Fully 3D printed Organic Electrochemical Transistors for biosensing applications

by

Darren Majak

A thesis submitted in partial fulfillment of the requirements for the degree of

Master of Science

Microsystems and Nanodevices

Department of Electrical and Computer Engineering
University of Alberta

Abstract

Biosensors are a large market that is quickly gaining traction and is a large industry that is projected to continue its rapid growth. One of the main challenges with biosensors are developing reliable, high sensitivity, repeatable sensors economically and rapidly. In this work, I have used 3D printing for developing organic transistors and logic gates for biosensing applications. These sensors are based on organic electrochemical transistors (OECTs) with Poly(3,4-ethylenedioxythiophene)-poly(styrenesulfonate) (PEDOT:PSS) as the channel material. Recreational use of cannabis was legalized in Canada in 2018, however, the detection of impairment has remained elusive for law enforcement. The psychoactive ingredient in cannabis, Δ^9-Tetrahydrocannabinol (THC), can be sensed in saliva and other body fluids thus indicating impairment. We have established that by using a platinum gate coupled with an OECT, concentrations of THC down to 0.05 nM can be sensed in DI water. This is the first step in creating THC sensors for saliva, which can detect impairment.

These OECT based sensors were also used as melatonin concentration sensors. Due to the nature of melatonin, the Redox reaction is not reversible. This means that the sensors are single-use sensors and can only be used once. These sensors show a distinct difference between the response for 1 μM and 10 nM. These are preliminary results show the capabilities of OECTs as Melatonin sensors.

Normally, one requires signal processing including multiplexing for the signal from these sensors and these are done off the sensor circuitry. Multiplexing is an important aspect of sensing as it allows for multiple entities to be sensed. Here, fully 3D printed multiplexers (MUX) based on organic electrochemical transistors (OECTs) with Poly(3,4-ethylenedioxythiophene)-poly(styrenesulfonate) (PEDOT:PSS) as the channel material. We have established that by arranging single OECTs, logic gates can be created that can then be arranged to make a MUX. A MUX can then be used to process signals from multiple sensors, thus allowing for a more complete biosensing platform to be created.

These logic gates show sensing capabilities as the results have predictable shifts depending on the concentration of cations used on the OECT channels. These sensing capabilities are explored using an inverter logic gate. These inverters show a distinction between various concentrations as well as a distinction between different cations. These sensors have a LOD of 1mM. Preliminary results for pH detection using NOT logic gates are also presented.

Preface

This thesis is the original work of Darren Majak, however, some fabrication of devices presented in Chapter 3, Chapter 4, Chapter 6 and the work presented in Appendix 1 were done in collaboration with Jiaxin Fan. All measurements, characterization, and analysis were completed by Darren Majak

Chapter 6 of this thesis has been published as Darren Majak, Jiaxin Fan and Dr. Manisha Gupta "*Fully 3D printed OECT based logic gate for detection of cation type and concentration*," Sensors and Actuators B: Chemical, vol. 286, issue 3, 111-118. [1]. Darren Majak fabricated the sensors, tested them and wrote the manuscript. Jiaxin Fan helped with sensor fabrication and manuscript editing. Dr. Manisha Gupta was the supervising author and was involved in manuscript editing and contributions. This chapter includes Appendix A, which is the publish supplementary data, and Appendix B which is unpublished data.

Acknowledgements

I would like to thank my supervisor, Dr. Manisha Gupta, for her support and guidance and for allowing me to grow, learn and achieve. I would like to thank my colleagues for their support and discussions, including Jiaxin Fan. I would like to thank the NanoFab at the University of Alberta for their training and expertise. My student intern Jiajie Li for all of his work, especially his work with LabVIEW programming. I would also like to thank the Electrical Engineering Department, the Faculty of Engineering and the University of Alberta. I would like to recognize the contributions of The Queen Elizabeth Academic Scholarship, and CMC Microsystems for their MNT Award which cover characterization costs. I would finally like to thank Patrick Remo for his support.

Table of Contents

List of Tables

List of Figures

1. Introduction

Biosensors are becoming more and more crucial to provide essential health metrics to medical professionals, law enforcement and everyday users. There is a growing trend towards more personalized health data with continuous monitoring, away from the traditional, one-time measurements that only provide a small snapshot into overall health. The traditional method is expensive, time-consuming, requires large laboratories with large, expensive equipment and specially trained staff.

There have been several different sensors introduced to circumvent the need for laboratory sensors that can sense various bio-entities. However, a number of these can be invasive; requiring either implantation into the patient or repeated extraction of bio-fluids like blood, which can be painful and can increase the risk of biocompatibility issues and infection. Non-invasive sensing is ideal but often requires sample preparation or bulky and complicated external circuitry to allow for signal processing. What the industry is lacking are non-invasive sensors that are both biocompatible and economical and can easily provide continuous monitoring with minimal external circuitry.

One of the main drawbacks of biosensors is the high production cost. Unlike traditional laboratory approaches, most biosensors are disposable or have limited usage due to sanitary requirements. It also requires expensive and complicated manufacturing processes, making them inaccessible solutions.

The work presented in this thesis is non-invasive biosensors that address a number of drawbacks and limitations of the current biosensors. This thesis presents a novel fabrication method for organic biosensors, specifically 3D printed Organic Electrochemical Transistors (OECTs). OECTs are wet sensors that, because of the use of organic semiconductors (OSC), are biocompatible. They also have low current levels and built-in amplification meaning that they require limited external circuitry. These biosensors are fabricated by two different 3D printed methods, gas injection 3D printing and aerosol jet 3D printing. 3D printing allows for fast, customizable and more economical manufacturing. There are several different biosensors presented in this thesis including, a Δ9-tetrahydrocannabinol sensor using a single OECT, a melatonin sensor using a single OECT, a cation concentration sensor using two OECTs arranged into an inverter logic gate, and finally various logic gates using several OECTs to demonstrate the building blocks for multiplexers, including NOT, NOR and NAND gates.

1.1. Biosensors, Background and Motivation

Biosensors is a crucial field to grow the capabilities of the medical industry. Not only can they provide healthcare workers with a larger arsenal of tools to quickly diagnose and treat patients but also provide continuous monitoring for users, providing a broader, more complete image of their health. Having a broader image of the user's health treatment can go from symptomatic treatments to a more holistic and effective approach that targets the root cause. Biosensors are becoming more accurate, smaller, more affordable, and detecting more and more biometrics. They also lend themselves well to the Internet of Things (IoT) and big data, leading to better, more personalized health care and preventative medicine. It is becoming a large industry and is predicted to grow from USD 17.85 Billion in 2017 to USD 40.37 billion by 2023 [2].

Biosensors are analytical devices that detect the presence or the concentration of bio-entities such as biomolecules or microorganisms. Different kinds of biosensors can detect a large range of different bio-entities in an analyte, ranging from cation concentration to hormone concentrations. The goal is to sense a large range of biomolecules with high accuracy, repeatability and the desired sensitivity required for detection. Typically, the detection and measurement of biomolecules and bio-entities is a time consuming and expensive process, requiring samples to be taken and then brought to a laboratory for testing, normally done via blood or urine tests. Biosensors provide an alternative to the large and expensive analytic equipment traditionally used[3], while still offering the ability to sense a large variety of bio-entities and biomolecules with high accuracy and precision. Other body fluids can be used including sweat, saliva and tears to detect analytes with the same accuracy as traditional methods, opening the door for wearable and non-invasive detection[4].

Biosensing has three elements: (1) **bio-detection**, which is an element to detect the bio-entity, (2) **bio-transducer** which converts the bio-signal to an electrical signal and (3) **signal processing** which makes the results readable [5]. These elements are illustrated in Figure 1.1. There are several different ways for **bio-detection (1)** to be done including enzymes, microbes, organelles, cells, or tissues, antibodies, receptors, nucleic acids, and aptamers [6,7]. Some bio-detectors add specificity; however, some transducers have intrinsic bio-detection properties. There are also several different types of **bio-transducers (2)** [8]available including, (i) optical, (ii) piezoelectrical, (iii) thermal and (iv) electrochemical [6,9].

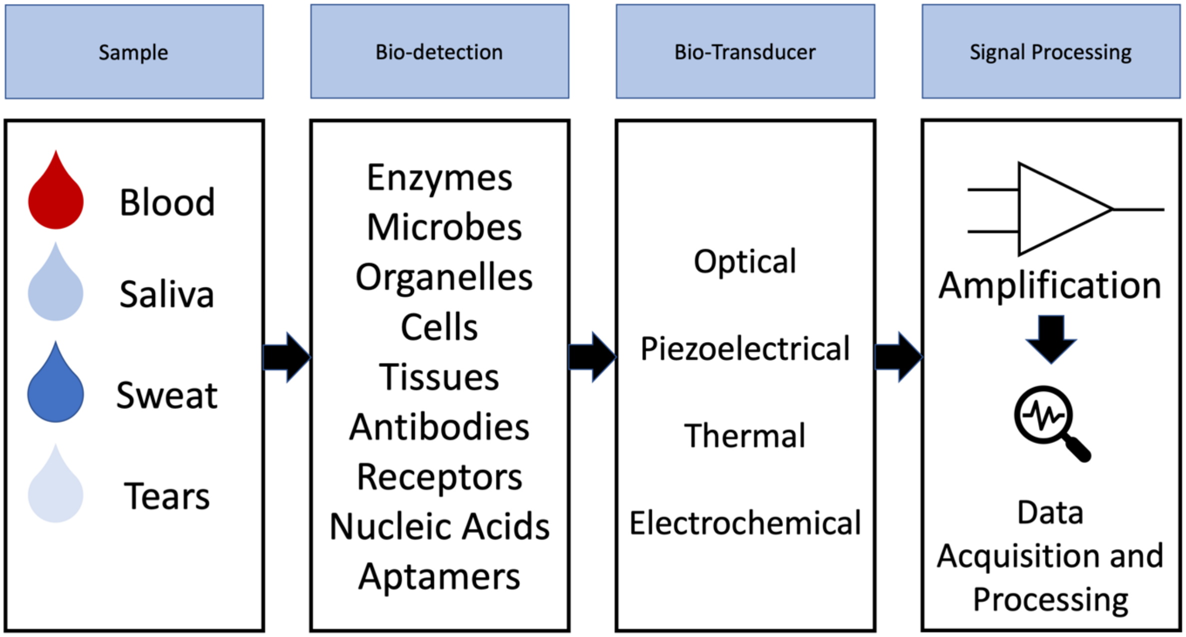

Figure 1.1 Figure demonstrating the different elements of a biosensor, including bio-detection, bio-transducers and signal processing.

Optical sensors (i) use light to measure bio-entities. Light is directed at the sensing area and then the reflected light is measured. There are various techniques to guide the light to the sensing surface and measure the reflected light, but the overall principle remains the same. Different sensors measure different optical signals including, reflectivity, fluorescence, absorption, chemiluminescence, and surface plasma resonance[6,10–12]. *Piezoelectric sensors* (ii) are simple sensors that take advantage of the piezoelectric effect; when bio-entities attach themselves, the piezo crystal is compressed, changing the frequency at which it oscillates. *Thermal based sensors* (iii) measure the temperature of a biological reaction and correlate that to the theoretical change. Other sensors rely on nanotechnology including quantum dots, which are normally coupled with optical sensors, carbon nanotubes which are often used in electrochemical sensing and graphene. Finally, *Electrochemical based sensors* (iv) detect changes in an analyte's electrochemical properties. These sensors can either take advantage of changes in voltage, current or conductivity of material based on the electrochemical interaction of the analyte with that material.

Biosensors have come a long way since the first biosensor reported in 1962 by Clark and Lyons [13] which detected blood oxygen levels. However, there remains a large gap in the field. Several biosensors are still bulky and expensive and difficult to miniaturize or require invasive procedures. Many biosensors require implantation of the sensor or blood sampling which can lead to painful wounds, scarring, discomfort and risk of infection. Blood sampling can be difficult in certain patients including, infants, elderly, hemophiliacs and hemophobics. Also, blood sampling often requires a large amount of preprocessing, to separate components before analyte can properly be sensed. This is why non-invasive and wearable biosensing is so sought after. In addition, wearable biosensors and bio-wearables are of great interest as they can provide continuous monitoring of health data that can lead to a more extensive and thorough picture of health. However, not all bio-transducers are ideal for non-invasive or wearable sensing methods. Three of the four bio-transducers discussed above often rely on expansive and bulky equipment, are difficult and time-consuming to manufacture, are difficult to miniaturize and are rigid and inflexible. Non-invasive and wearable biosensing requires the transducers to be small, flexible, durable, comfortable, biocompatible and inexpensive to manufacture. The best bio-transducer type for this application is *electrochemical based sensors* (iv). These sensors are simple, portable, cost-effective and can be miniaturized [14]. Also, electrochemical transducers are ideal for non-invasive sensing as they naturally lend themselves to liquid analytes. Liquid analytes are typically used for non-invasive sensing, including sweat, tears, saliva and interstitial fluid.[4,154]

There are challenges to non-invasive and bio-wearables, as they rely on sweat, tears, saliva and interstitial fluid, which generally have low concentrations and high volatility. Several sensors use tears as there are correlations with blood levels and tear levels of as the analyte as discussed in a review by Bandodkar et al. [15], however, tears are a difficult analyte to analyze as they are difficult to harvest, and can only be harvested in small amounts, which are volatile to evaporation. Also, the eye is highly sensitive to foreign material, making it challenging for in-vitro, continuous monitoring. Interstitial fluid is also difficult to harvest, and continuous monitoring can lead to immense discomfort as microneedles have to be inserted through the skin. This is why a large number of non-invasive and wearable biosensors use saliva or sweat based sensing as it offers the ability to sense a large number of analytes without the many preprocessing steps required as with blood. Saliva and sweat have several bio-entities and can be a great indicator of overall health [16]. Many bio-entities and their links to health have been outlined in a review by Bandodkar et al. [15]. Electrochemical bio-transducers are ideal for non-invasive sensing. Many approaches are used for electrochemical sensing including sensors using Carbon Nanotubes [17], graphene [18] and quantum dot-aptamers [19], carbon nanofibers[20] and nanowires [21]. However, one of the most versatile ones is electrochemical biosensors that are based on organic semiconductor (OSC). Organic semiconductors have many benefits, in a biosensing context. First, OSCs can be solution-processed, meaning that non-traditional forms of manufacturing can be used, thereby decreasing cost and time to manufacture. This is discussed further in the fabrication section (Section 2.3) of this chapter. In addition, OSC can be bio-compatible, making them ideal for biosensing. Finally, OSC can potentially combine all three parts of a biosensor (bio-detection, bio-transduction and signal processing) discussed above, into one device. This can be done with certain OSC because they are electrochemically active and naturally have bio-detection properties. These electrochemically active OSC can be used in transistors, which are a well-studied and understood transducer. Finally, the signal processing can be all done by combining organic transistors, meaning that all three parts of biosensors can be manufactured using a single OSC and one type of device. Organic semiconductors are discussed further later in this chapter (Section 2.1).

As mentioned above, one of the most straight forward ways to utilize OSC as electrochemical biosensors is to use them in transistors. There are several types of transistors using OSC, many of which are outlined in a review by Kergoat et al. [22], these include Organic electrochemical transistors (OECTs), Organic field-effect transistors (OFETs), Organic Ion-Sensitive Field Effect Transistors (ISFETs), and Electrolyte-gated organic field-effect transistors (EGOFETs). There are benefits and drawbacks to each of these organic transistors. OFETs often behave at high operating voltages making them not ideal for wearables as they can be damaging to humans. Though some have been demonstrated with low operating voltages [23–26] However, not without alterations. Organic ISFETs have issues with hysteresis, long term drift and thermal drift, making them ill-suited for long term or continuous sensing [27]. EGOFETs, resemble OECTs in structure, however, they behave differently. EGOFETs rely on a capacitance process for the switching of the transistor while the OECTs use a charge transfer from the electrolyte to the OSC[28]. EGOFETs though having lower voltages than OFETs have the disadvantage of only being a potentiometric sensor, while OECTs can be potentiometric or amperometric [29]. Also, OECTs have built-in amplification, can operate at low voltages and have high sensitivity. This means that they are ideally suited for non-invasive and wearable biosensing. OECTs are the technique used for biosensing in this thesis and the operating principle is described in Section 2.2.

1.1.1. Where are the gaps?

Though biosensors, including OECTs, have been demonstrated to sense, various bio-entities, there is still a lot of room for development. One of these areas is to reduce the complexity and the cost of manufacturing. Due to the nature biosensing, there are concerns about cross-contamination and sanitation, leading to the need for disposable sensors. Also, there can be a lot of wear and strain put on non-invasive and wearable sensors, leading to them breaking or weakening in performance. This is ideal to decrease the complexity of the sensors and the fabrication as well as the cost. That is why the work in this thesis uses state of the art 3D printing techniques to make the fabrication more cost-effective as well as allow for fast prototyping and customization. This is discussed in more detail later in this chapter (Section 2.3).

Several different approaches have been used to sense various bio-entities to varying degrees of sensitivity. However, a major hurdle in biosensing is to develop wearable and non-invasive biosensors that are simple, small, durable, biocompatible, cost-effective and highly sensitive. Due to these requirements, many bio-entities still need a reliable, non-invasive and wearable sensor. This includes certain types of hormones, including melatonin. Melatonin has been sensed using sensors based on graphene [30] [31], ZnO nanorods [32], molecularly imprinted polymer [333435], nano palladium [36], cyclic voltammetry [3738] and more. However, there is still a need for fast, reliable and portable sensing of melatonin concentrations in body fluids, especially a method that is simple and cost-effective. Therefore, melatonin sensors have been developed. These results are presented in Chapter 4.

Another sensing gap in biosensors is the detection of drug concentrations, indicating impairment. With the legalization of cannabis use in Canada in 2017, there are growing concerns for the detection of impairment, however, a cost-effective and reliable solution has yet to be found. The detection of impairment requires the sensing of THC levels. There are several approaches, including electrochemical detection[39–42], liquid chromatography-mass spectrometry[43–47], radioimmunoassay[48], gas chromatography-mass spectrometry[49–57], fluorescence immunoassay[58,59], mass spectrometry[60], and thin-layer chromatography. However, these solutions can be bulky, expensive and not ideally suited for roadside testing. Therefore, fully 3D printed, non-invasive, THC sensors were developed which are presented in Chapter 4.

A major goal in biosensing is to create biosensing platforms that can sense multiple entities and handle signal processing. The issue here is when using individual biosensors targeted at specific bio-entities, the sensing platform can become large and bulky, with the outputs and inputs having to be individually managed, requiring bulky circuitry. There have been signal processing circuits made for generic current output biosensors [61]. As well as larger sensing platforms with signal processing circuitry[62,63]. However, a multi-biosensor platform that can incorporate single processing and sensing in a single device ideal. Organic transistors can be arranged into logic circuits, meaning that the bio-detection, bio-transduction and the signal processing can all be done with the same device. There have been some organic logic gates demonstrated [64–70], however, these logic gates are not used for sensing and some use multiple OSC making them more complex. Therefore, logic circuits were 3D printed using one OSC, demonstrating the building blocks for fully 3D printed signal processing biosensors. These are discussed in Chapter 5. These logic gates have the added benefit of converting the current output of a single transistor to a voltage output, this allows for easier signal processing. In addition, logic gates can be used as reference sensors, for cation concentration and pH, which have been demonstrated in Chapter 6. Though there have been several Ion sensors [62,71,72] [73,74] and pH sensors[75–77] sensors developed, there is always a need for higher sensitivity and lower limits of detection. There is still a need for biosensors that can detect cation concentrations and pH and incorporate signal processing. Therefore, an ion and pH sensor that incorporates signal processing into a single device was developed around an inverter gate is been demonstrated in Chapter 6.

1.2. Solution

To fully address the gaps discussed, the solution presented uses a two-pronged approach: (1) the sensing mechanism and (2) the fabrication method. The sensing mechanism uses Organic Electrochemical Transistors (OECTs) which are perfectly suited for active, non-invasive, biosensors because they are electrochemically active devices that work in ‘wet’ environments. They are also biocompatible and have built-in amplification due to the high gain and high transconductance, which translates into high sensitivity at a low operating voltage. The fabrication method, 3D printing, is possible because OECTs use organic semiconductors (OSC) which are solution processable.

In terms of mass production, 3D printing is a highly customizable, faster, and more cost-effective alternative in commercializing these devices. Some biosensors in this thesis are meant to be wearable, multi-use devices like those presented in Chapter 5 and Chapter 6, while others are meant to be single-use, disposable sensors, to avoid cross-contamination and false positives like those presented in Chapter 4. 3D printing allows for the feasibility of disposable sensors as it lowers the cost of fabrication. OECTs and 3D printing are discussed in detail in Section 2.2 and Section 2.3 respectively.

1.3. Overview

The thesis is organized into seven chapters which are outlined below.

Chapter 1 introduces the thesis and provides a brief overview of the thesis.

Chapter 2 is the background chapter that explores the background information and a literature review of the biosensors, specifically electrochemical non-invasive biosensors. This chapter introduces organic semiconductors, and their working principle as well as the working principle for OECTs. The characterization and fabrication techniques including gas injection 3D printing and aerosol jet 3D printing are also discussed.

Chapter 3 discusses OECT characterization and optimization. The measurements for the work presented here were done by Darren Majak and the fabrication for the devices was done by Jiaxin Fan and Darren Majak.

Chapter 4 discusses the fabrication and testing of THC and melatonin single-use disposable sensors using a single 3D printed OECT. The sensors for this work were fabricated both by Jiaxin Fan and Darren Majak. The optical and scanning electron microscope images were taken by Jiaxin Fan. The measurements were done by Darren Majak.

Chapter 5 discusses logic gates, including NOT, NOR, NAND and MUX gates. These logic gates were fabricated by Darren Majak and tested by Darren Majak

Chapter 6 is a published paper written by Darren Majak, Jiaxin Fan and Dr. Manisha Gupta as "Fully 3D printed OECT based logic gate for detection of cation type and concentration," Sensors and Actuators B: Chemical, vol. 286, issue 3, 111-118. [1]. Darren Majak fabricated the sensors, tested them and wrote the manuscript. Jiaxin Fan helped with sensor fabrication and manuscript editing. Dr. Manisha Gupta was the supervising author and was involved in manuscript editing and contributions. This chapter includes Appendix A, which is the published supplementary data, and Appendix B which is an unpublished data showing preliminary results for NOT gates as pH sensors.

Chapter 7 is the summary and conclusion of the thesis where future work is presented.

Appendix 1 is a characterization of PEDOT:PSS printed with the Optomec aerosol jet 3D printer using the Ultrasonic Atomizer. This work was completed by Darren Majak and Jiaxin Fan.

2. Background

The purpose of this chapter is to provide background information to support the work presented in this thesis. The devices in this thesis are based on Organic Electrochemical Transistors (OECTs) that use organic semiconductors (OSC), specifically poly(3,4-ethylenedioxythiophene) polystyrene sulfonate (PEDOT:PSS) as their active component. The concepts of hybridization, conjugation as well as σ and π-bonding are discussed to explain the working principle of OSCs. The motivation and working principle of PEDOT:PSS and OECTs are presented in this chapter along with background information on the additive manufacturing process. Detailed descriptions of the working principle behind the two methods of fabrication, gas injection and aerosol jet 3D printing, are also presented. Finally, the various characterization techniques and their working principles are described; including four-point probe, profilometry, fixed angle ellipsometry and source meter IV measurement techniques.

2.1. Organic Semiconductors

Organic electronics have the potential to solve many sensing problems that have been difficult with conventional electronics in the past. Organic electronics included Organic Photovoltaics (OPVs), Organic Light-Emitting Diodes (OLEDs), and Organic Thin-Film Transistors (OTFTs), Organic Field-Effect transistors (OFETs) Organic Electrochemical Transistors (OECTs) which are the focus of this thesis. Organic electronics are based on conductive, conjugated, organic polymers are the basis of organic semiconductors (OSC), which were first reported in 1948[78]. By 1977, work was reported high conductivity for doped polymers that led to the Nobel prize in chemistry in 2000[79]. To discuss the electronic behaviour of organic semiconductors, it is integral to first discuss the concepts of hybridization, conjugation and π - π stacking.

2.1.1. Hybridization

Orbital Hybridization is when atomic orbitals combine to create new orbitals that have different shapes and energies. These combined orbitals are called hybrid orbitals. Hybridization can explain the shape of molecular geometry, like that of polymers and organic polymers. Hybridization can affect the molecular shape of compounds. There are different ways that s and p orbitals combine, including sp^3, sp^2 and sp hybridization. Organic materials are based on sp^2 hybridized carbon chains. However, atomic carbon has six electrons, with the configuration $1s^2\,2s^2\,2p^2$. This means the s orbitals are fully filled while the p orbitals are only partially filled. This leads to sp hybridization, between the filled s and the unfilled p orbitals. Hybridizations can reduce bond strength. The sp^2 hybridized orbitals are shared with other adjacent carbons, which form strong sigma (σ) bonds that are highly directional. The shared sp^2 orbitals are planar. The fourth valence electron, that does not occupy one of the three sp^2 orbitals occupies a $2p_z$ orbital that is perpendicular to the sp^2 plane. This structure leads to carbon chains that can have branched structures, which are very stable. The formation of hybrid orbitals is illustrated in Figure 2.1.

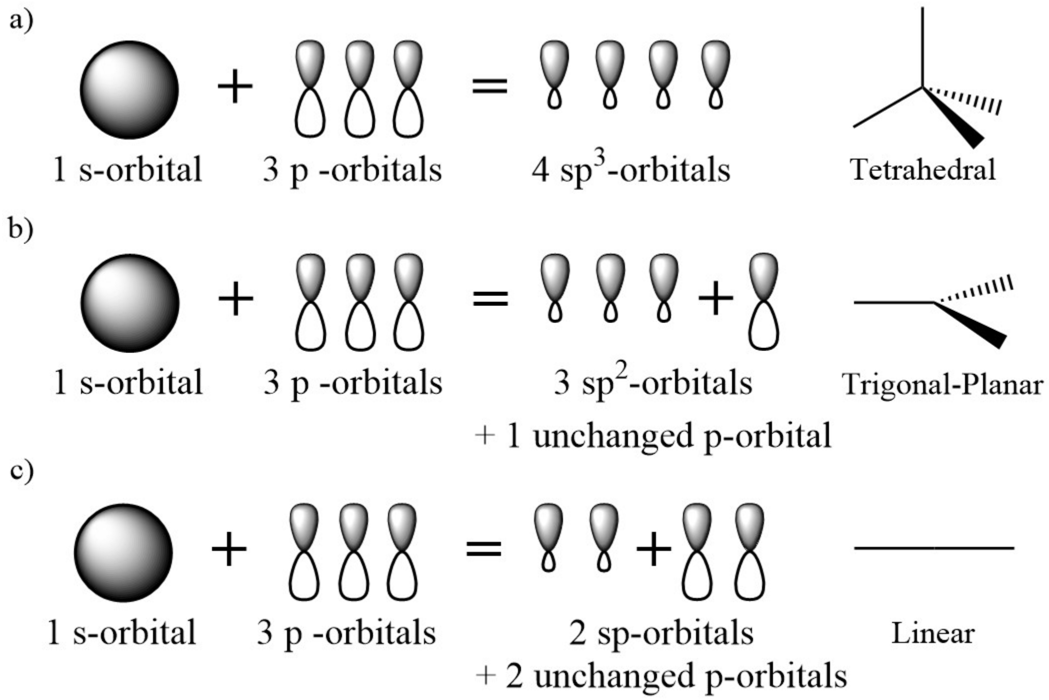

Figure 2.1 shows the different forms of hybridization bonds. a) Formation of an sp^3*, which has a tetrahedral configuration. b) Formation of sp*^{2} *orbitals, which has a trigonal-planar configuration. c) Formation of the sp orbitals, which has a linear configuration.*

The perpendicular $2p_z$ orbitals hybridize and form weak π and π* orbitals which are bonding and anti-bonding orbitals respectively. The π and π* orbitals make the molecule planar, which leads to the delocalization of the π and π* orbitals across several carbon atoms. This is conjugations, described in section 2.1.2.

2.1.2. Conjugation

Conjugation is a term first coined by Johannes Thiele in 1899 [80]. It can be described by Molecular Orbital theory in terms of electron delocalization over all atoms in a molecular orbital[81]. Specifically, conjugation is the delocalization of π electrons across several hybridized *p*-orbitals. This means that π electrons are shared between several atoms rather than a single bond or a single atom. Conjugation takes place in molecules with alternating single and double or triple bonds. Conjugations generally lower the energy of the molecule but increase its stability.

2.1.3. σ and π-Bonding

π-bonding is a concept in molecular orbital theory describing a type of covalent bond. It is when two π-orbitals from a single atom overlap laterally with two lobes from another. The nuclei plane has zero electron density, meaning that the electron concentration is above and below it.

A single bond contains a single σ bond, a double bond contains one σ and one π bond, and a triple bond contains one σ and two π bonds. σ bonds are made from the overlap of atomic orbitals. In the case of a carbon-hydrogen bond, the hydrogen is *s* hybridized while the carbon is sp^2 hybridized. The overlap of these hybridized orbitals leads to a σ bond. In the case of single bonds between carbon atoms, as seen in polymer chains, the two sp^2 hybridized orbitals overlap, leading to a σ bond. π bonds, come from un-hybridized *p* orbitals, where the orbitals overlap, a π bond is formed. π and σ bonds are covalent bonds, meaning that they are directional and prefer specific orientations. The bonds are formed by overlapping orbitals and therefore only specific orientations are possible. σ bonds are stronger bonds, as there is more overlap of the orbitals than π bonds. π bonds lead to π- π stacking and are integral to the formation of polymer chains and the packing of polymer films, which highly affect the conductivity of semiconducting organic polymers.

π- π stacking is the interaction of π bonds. π stacking occurs between conjugated groups. π stacking affects the packing of the organic polymer and leads to intermolecular charge transport. Also, by increasing the π stacking and lowering the crystallinity of an organic polymer, the mechanical properties of polymers can be heavily impacted, including an increase in flexibility, tensile strength and strain tolerance[82], all hallmark features of organic polymers which make them ideal for biosensor applications.

All these phenomena, hybridization, conjugation and π - π stacking, are what allow for organic semiconductors to have the properties that are ideal for biosensing including flexibility, tensile strength, strain tolerance, and conductivity.

2.1.4. Conduction Mechanism (Hopping)

HOMO and LUMO levels stand for Highest Occupied Molecular Orbitals and Lowest Unoccupied Molecular Orbital respectively. HOMO and LUMO levels arise from the π and the π* orbitals. The π orbital is spin allowed π states, while the π* states are above an energy gap and tend to be unoccupied. Increasing conjugation will narrow the bandgap by increasing the number of hybrid states.

The conduction mechanism in organic polymers is known as hopping. There are two primary forms of conduction, band transport which is primarily in crystalline solids and is intra-molecular. Hopping, however, takes place in molecular solids like organic semiconductors and is inter-molecular. The underlying mechanism for band transport is the formation of the conduction and valence band and is due to the Pauli Exclusion Principle which states that no two electrons can have the same four electronic quantum numbers in a molecule. Therefore when atoms combine into molecules, the atomic orbitals overlap[83] but cannot occupy the same energy level. This means that for N number of atoms in a molecule, then there will be N molecular orbitals that have N different energy levels to allow for electrons to satisfy the Pauli Exclusion Principle. In a solid there are a large number of atoms, this means that the energy levels are very closely spaced, and the discrete energy levels are considered continuous. This is what forms the bands. The conduction band is lower in energy and tends to be occupied, while the valence band is unoccupied. The transition between the bands can either create electrical current (excitation) or create light (relaxation). Atomic crystal can have atoms replaced in a process known as doping to either provide excess electrons (n-type doping) or excess holes (p-type doping) for conduction. When a bias is applied the carriers can freely flow in the bands as the states are continuous. This is the basis for traditional, inorganic semiconductor-based electronics.

In hopping transport, however, conduction occurs in the HOMO and LUMO orbitals which are analogous to the conduction and valence bands respectively in band theory. The HOMO and LUMO levels come from the π and the π* orbitals. As discussed earlier, when two unhybridized *p* atomic orbitals overlap, they create two molecular orbitals. The atomic orbitals can either combine in-phase or out-of-phase. The in-phase combination of the atomic *p* orbitals is lower in energy and leads to the bonding π molecular orbital. The out-of-phase combination of the atomic *p* orbitals leads to the higher energy π* molecular orbital. The π orbital is spin allowed π states, while the π* states are above an energy gap and tend to be unoccupied. When N number of atoms are in a molecule and N *p* atomic orbitals overlap, the in-phase and out-of-phase combinations increase. It is not simple in or out-of-phase however, the orbitals can be all in-phase, and have (N-1) bonding interactions, 0 anti-bonding interactions and 0 nodal planes to (N-1) antibonding interactions, 0 bonding interactions and (N-1) nodal planes. As the number of antibonding bonding interactions increase, the number of bonding interactions decreases. In other words, as the number of anti-bonding interactions increases the energy also increases. This is illustrated in Figure 2.2. This leads to N number of states. These states will either be in the HOMO or LUMO band. The HOMO band contains all states from (N-1) to N/2 bonding states (0 to N/2-1 anti-bonding states) while the LUMO band contains all states from N/2 to (N-1) anti-bonding states (N/2-1 to 0 bonding states).

Increasing the number of hybrid states increases conjugation. This can also be called lengthening the π system or increasing the degree of polymerization. This leads to the energy gap between the HOMO and LUMO decreasing. This illustrated in Figure 2.2.

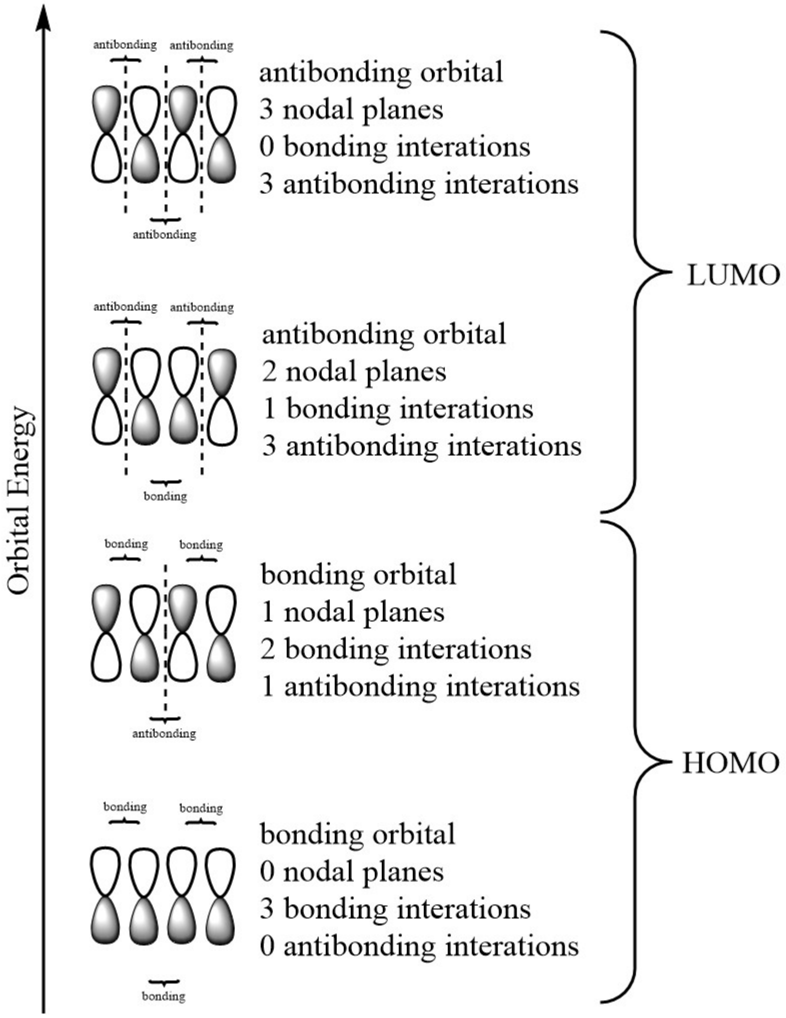

Figure 2.2 Shows how orbitals combine in and out of phase to produce HOMO and LUMO levels.

The conductions mechanism in HOMO and LUMO bands are different as the states are discrete instead of continuous as with band conduction. This means the carriers cannot easily flow when a bias is applied. Instead, the carrier must hop or tunnel from one state to another in the molecular orbital. In addition, the charge carriers in each mechanism are also different. With band conduction, electrons and holes are the charge carries, but in hopping transport the charge carriers are quasi-particles including solitons, polarons and bipolarons. These quasiparticles arise from local distortion of polymer chains.

Polymers can either have a degenerate ground state or a non-degenerate ground state. A ground state is the lowest energy state if there is more than one ground state, it is called degenerate. For these systems, because of the degenerate ground states, changes in single and double bonds will not change the overall energy because there are different configurations for the same energy. Therefore, for polymers with degenerate ground states, the charge carriers are solitons. Solitons are used to describe a self-sustaining wave packet that travels at a constant velocity and maintains its shape. Unpaired π-electrons and bond distortions form a soliton. The soliton is the charge carrier for degenerate conjugated polymers[84–87].

Polymers that are non-degenerate, changes in double and single bonds will change the energy of the system. When electrons are added or subtracted from the system, radicals form which cause local deformations, these form polarons and bipolarons, which are two coupled polarons. Polarons and bipolarons act as the charge carriers in non-degenerate conjugated polymers.

In degenerate and non-degenerate conjugated polymers, the charge carriers move along the polymer chain. Hopping and tunnelling of the charge carriers are the main charge transport mechanisms. This charge transport occurs between adjacent chains by hopping between π-orbitals. [84–87].

Conduction can be affected by various factors, including crystallinity, uniformity as well as temperature. Increased uniformity and crystallinity lead to better conduction with both band and hopping transport mechanisms. The temperature has the opposite effect on each transport mechanism. With band transport, as the temperature increases the kinetic energy of carriers increases, which increases the number of collisions and scattering, thereby decreasing mobility. In hopping transport, however, the mobility increases with temperature as it helps the transport of charge carriers.

2.1.5. Benefits of Organic Semiconductors

Hybridization, conjugation and π - π stacking are integral to the working of OSC and lead to the ability of OSC to conduct charge. In addition to the electrical properties of OSC, other properties allow them to be used and processed in new and novel ways. These include flexibility, stretchability, transparency, biocompatibility and ultimately solution processability. Due to these properties, especially low-temperature solution processability, addresses the drawbacks associated with inorganic semiconductors. Traditional electronics based on silicon are rigid and inflexible and have high material and manufacturing costs. This is discussed further in the manufacturing Section 2.3. Though traditional electronics are used in sensing, they are mostly incompatible to be used in biosensing. On the contrary, the properties of OSC are perfect candidates for biosensors. OSCs have been used in biosensors of various kinds including OFETs, OTFTs and OECTs, which are the main focus of this thesis.

2.1.6. Types of Organic Semiconductors

Several different types of organic semiconductors are used in organic electronics. These OSC can be divided into n-type and p-type organic semiconductors. N-type semiconductors are rare, and difficult to manufacture there are several outlined in a review by Borges-Gonzálezet al. [88]. Poly([N,N′-bis(2- octyldodecyl)-naphthalene-1,4,5,8-bis(dicarboximide)-2,6-diyl]-alt-5,5′-(2,2′-bithiophene)) *P(NDI2OD-T2)* [89] has been used in n-type accumulation mode OECT have been demonstrated[90]. Poly(benzimidazobenzophenanthroline (*BBL*) has been used in OFETs [91] and

OECTs[64]. P*entacene* has been demonstrated in OTFTs [92]. Poly(3-hexylthiophene) (*P3HT*) has been used in OFETs[93]. Poly(2,5-bis(3-alkylthiophen-2-yl)thieno[3,2-b]thiophenes (*PBTTT*) has been demonstrated in OFETs[94]. Poly(2-(3,3′-bis(2-(2-(2- methoxyethoxy)ethoxy)ethoxy)-[2,2’-bithiophen]-5-yl)thieno- [3,2-b]thiophene) (*p(g2T-TT)*) has been used to make OECTs[95]. N-type polymers are an important component in bioelectronics and biosensors but have not been used for this work.

P-type organic semiconductors are more abundant and widely used and can be split into depletion and accumulation OSC. Several p-type OSC has been discussed by Borges-González et al. [88] some of them include: 5,5’-bis-(7-dodecyl-9H-fluoren-2-yl)-2,2’-bithiophene (*DDFTTF*) used in OFETs[96]. Alkoxyphenylene-thiophene oligomers have been used in OTFTs[97]. Poly[[2,5-bis(2-octyldodecyl)-2,3,5,6- tetrahydro-3,6- dioxopyrrolo[3,4-c]pyrrole-1,4-diyl]-alt-[[2,2′-(2,5-thiophene)- bis-thieno(3,2-b)thiophene]-5,5′-diyl]] (*DPP-DTT*) has been used in OFET sensing [98]. Poly(tetrathienoacene-diketopyrrolopyrrole) (*PTDPPTFT4)* has been used in OECTs[99]. Polypyrrole was the first OECT demonstrated by white et al. [100], Polyaniline (*PAni*) has been widely used in pH detection[101–104]. Finally, poly(3,4-ethylenedioxythiophene) polystyrene sulfonate (*PEDOT: PSS*), which is the focus of this thesis, and discussed more in-depth below.

2.1.7. PEDOT:PSS

A widely used and versatile organic semiconductor is poly(3,4-ethylenedioxythiophene) polystyrene sulfonate (PEDOT:PSS)[105,106] which is a p-type organic polymer that is electrochemically active, meaning that it works with electrolytes. PEDOT:PSS is ideal due to its high conductivity, solution processability and low redox potential [107,108]. PEDOT: PSS is two polymer chains that have a columbic attraction to each other; poly(3,4-ethylenedioxythiophene

(PEDOT) is a conjugated polymer and has a positive charge, sodium polystyrene sulfonate (PSS) is deprotonated sulfonyl group and has a negative charge. This is illustrated in Figure 2.3 and Figure 2.4. The PSS dopes the PEDOT. When a positive ion (cation) is introduced into the polymer, it attracts the slightly negative PSS, breaking the columbic attraction to the PEDOT. This de-dopes the PEDOT, lowering the conductivity. When PEDOT:PSS is used as a channel, the current level lowers when a positive charge (cation) is injected into the PEDOT:PSS it attracts the PSS from the PEDOT backbone, which de-dopes the channel, lowering the conductivity and turning the transistor off. The PEDOT:PSS and cation reaction is a reversible reaction as shown in Equation 2.1.

$$PEDOT^{+} : PSS^{-} + M^{+} + e^{-} \leftrightarrows PEDOT^{0} + M^{+} : PSS^{-} \tag{2.1}$$

Where M^{+} is a cation and e^{-} is an electron.

The quasi-particle used in the conduction mechanism is disputed and by some sources, it is reported to be a bipolaron[109–113], while others claim it to be a polaron[114,115].

PEDOT:PSS has been used in organic photovoltaics (OPVs), Organic Field-Effect Transistors (OFETS), Organic Electrochemical Transistors (OECTs). PEDOT:PSS is used in commercial electronics and therefore, there is a large variety of high-quality material available without the need for manufacturing of the OSC.

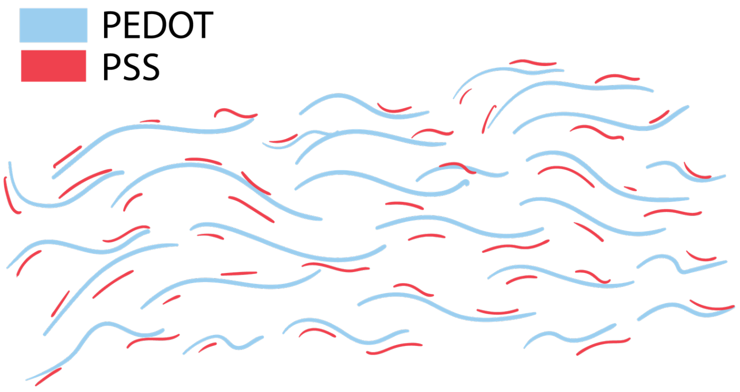

Figure 2.3 Graphic showing PEDOT:PSS structure. The PSS is attracted to the PEDOT through coulombic attractions

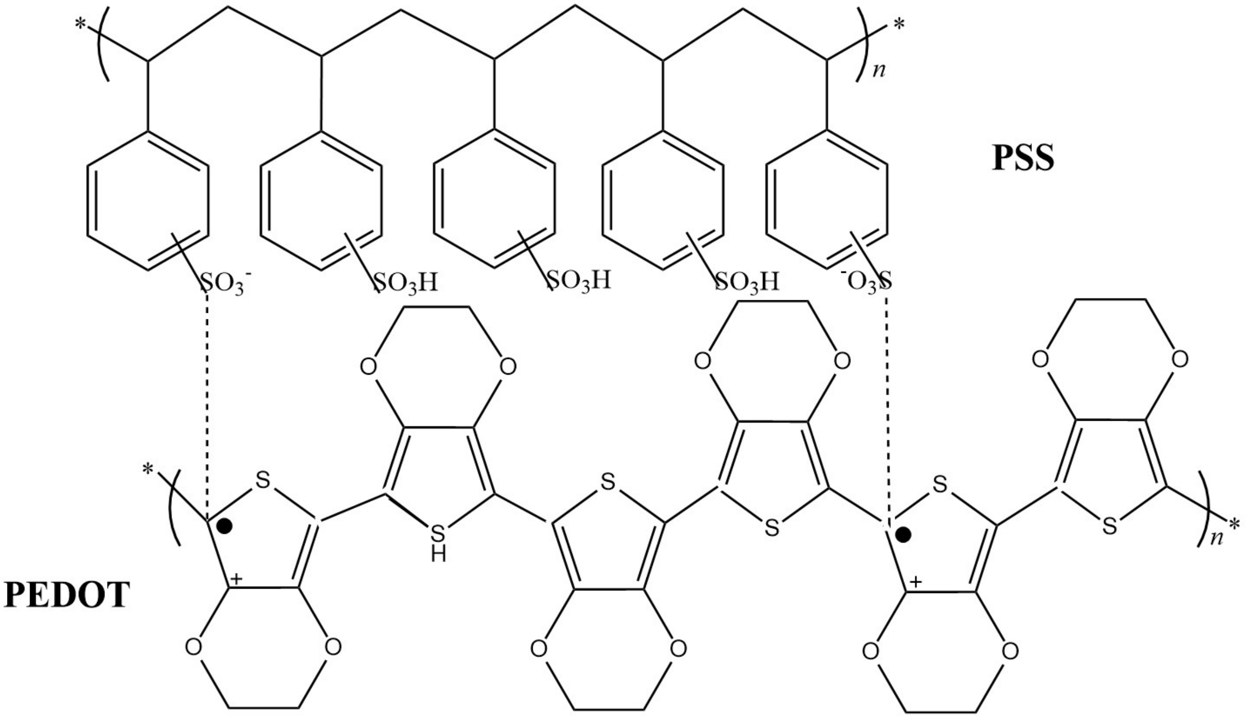

Figure 2.4 Chemical structure of PEDOT:PSS. The slightly negative PSS has a columbic attraction to the PEDOT, which is partially positive.

2.2. Organic Electrochemical Transistors (OECTs)

The sensors discussed in this thesis are based on Organic Electrochemical Transistors (OECTs). OECTs are electrochemically active meaning that they work with an electrolyte. OECTs are similar to traditional transistors, they have a source, a drain and a gate. However, instead of doped silicon for the channel, they use an organic polymer as the channel material. The gate is also removed from the channel material and an electrolyte is placed between the channel and the gate contact, like the dielectric in a MOSFET, however, in this case, the electrolyte has ions which act as charge carriers that enter the channel material. In our case, the channel material is a p-type organic semiconductor called poly(3,4-ethylenedioxythiophene) polystyrene sulfonate (PEDOT:PSS). The electrolyte sits on top of the PEDOT:PSS channel, when a gate voltage is applied, it drives cations into the channel, the cations de-dope the PEDOT:PSS because the cation attracts the PSS, pulling it away from the PEDOT. This lowers the conductivity of the channel and lowers the current between the source and the drain and turns off the OECT.

Due to this behaviour OECTs have been used as biosensors for various liquid medium entities[116–118]. They have been used to sense ion concentration [74,119], pH [75], glucose levels [120,121], hormone levels [122], DNA [123–125] and lactate [126]. PEDOT:PSS, is also a flexible material, meaning that other, flexible materials can be added in the fabrication of the complete sensors and devices, to make a more complete flexible circuit. In bio-sensing, flexibility is important as it allows for conformal adhesion to biological tissue topographies, thereby improving sensor accuracy [127,128]. In this case, we coupled the flexible PEDOT:PSS, with flexible silver electrodes, and PDMS masks, all of which were 3D printed with an aerosol jet 3D printer onto a flexible PET substrate.

2.2.1. OECT Working Principle

Depending on the material and the doping the transistor can either be p-type or n-type, which refers to the doping, and then either depletion or accumulation mode, which describes the behaviour of the transistor. A depletion-mode transistor is normally on, meaning the channel is conducting and there is a drain current flowing when there is no current or voltage applied to the gate. An accumulation mode device is normally off, meaning that the channel is not conducting and there is no drain current when there is no voltage or current applied to the gate.

OECTs were proposed by white et al in 1984[100] and first used polypyrrole as the active material. OECTs are transistors that behave in a similar way to traditional silicon transistors and have three contacts, the source, drain and gate but an electrolyte acts as a part of the gate contact. The model of the OECT is shown in Figure 2.5. As with a traditional transistor, a current or voltage signal applied to two terminals will change the current through the other two terminals. This is because the material that makes up the transistor channel changes its conductivity depending on the voltage or current applied. However, the difference is with the channel material which is made from organic semiconductor, specifically conductive, conjugated, organic polymers [129,130]. Just like traditional transistors, OECTs can be either p or n-type and act in depletion mode (normally on) or accumulation mode (normally off).

In our case the channel material is made from poly(3,4-ethylenedioxythiophene) polystyrene sulfonate (PEDOT:PSS) which is a p-type organic polymer, meaning that it is a p-type, depletion-mode transistor. These OECTs behave like a MOSFET, where a negative voltage is applied to the source ($V_S<0$) and the drain is grounded ($V_D=0$), this causes a drain current to flow through the channel (I_D). This current flow is then modulated by the gate voltage. When a positive gate voltage is applied, cations, from the electrolyte are driven into the porous channel material (PEDOT:PSS).

As seen in Equation 2.1, these cations pull the PSS away from the PEDOT, which causes the hole density to lower to maintain charge neutrality. In other words, the semiconductor is de-doped. The de-doping lowers the conductivity of semiconductors and ultimately lowers the drain current (I_D). When the gate voltage is sufficient, the drain current lowers to a point where the OECT turns off[105]. In steady-state OECT has a similar working principle to MOSFETs and therefore follows the same current equation, where the drain current is dependent on the gate voltage. However, unlike a MOSFET, the drain current is dependent on the channel thickness (d). This is because the drain current is directly correlated to the ability of cations to penetrate into the channel material[131]. This makes the drain current equation (2.2) as follows:

$$I_D = \mu d C^* \frac{w}{l}\left(V_T - V_G + \frac{V_D}{2}\right) V_D \qquad 2.2$$

Where μ is the hole mobility of the channel, w is the channel width, l is the channel length, d is the channel depth, C* is the capacitance per unit volume, V_T is the threshold voltage, V_G is the gate voltage and V_D is the drain voltage. In saturation, $V_D = V_G - V_T$ meaning that the above equation (2.3) becomes

$$I_{D,sat} = \mu d C^* \frac{w}{l}(V_T - V_G)^2 \qquad 2.3$$

From these equations (2.2 and 2.3), it is clear the current is dependent on the channel dimension *w*, *l* and *d*, which is the width, length and depth of the channel. Therefore, to tune the OECTs, these parameters can be adjusted. These adjustments can be easily made when the manufacturing method is 3D printing.

The OECT and its working principle according to Bernard's et al.[105] can be described according to an electronic circuit an ionic circuit model. The electronic circuit follows ohms law, and can be described by the following equation (2.4):

$$J(x) = q\mu p(x)\frac{dV(x)}{dx} \qquad 2.4$$

Where J is the current flux, q is the elementary charge, µ is the hole mobility, p is the hole density, and dV/dx is the electric field. The OECT works by doping and de-doping of the channel, meaning that the addition and subtraction of carriers respectively. According to Bernards et al. follows the equation (2.5):

$$p = p_0\left(1 - \frac{Q}{qp_0v}\right) \qquad 2.5$$

Where p is the hole density, p_0 is the initial hole density when the applied gate voltage is 0, Q is the total cation charge that is injected into the channel when a gate voltage is applied.

The ionic circuit, according to the Bernards' model, can be described as a resistor (R_s) and a capacitor (C_d) in series. Where the ionic current through them is described by Equation 2.6.

$$Q(t) = Q_{ss}[1 - exp(-t/\tau_i)] \qquad 2.6$$

Where $Q_{ss} = C_d\Delta V$ and is the total charge passing through the circuit, C_d is the modelled capacitance in the circuit, $\tau_i = C_dR_s$and is the ionic transit time, R_s is the modelled resistance in the circuit, ΔV is the applied gate voltage.

When using OECTs are sensors, an important parameter is transconductance, which is the ratio of the change in drain current to the change in gate voltage, using the above equations, the transconductance can be written as Equation (2.7).

$$g_m = \frac{\delta I_D}{\delta V_D} = \mu dC^* \frac{w}{l}(V_T - V_G) \qquad 2.7$$

From this, we can see that the transconductance is directly dependent on the channel thickness (d). This has been experimentally verified by Rivnay et al.[131].

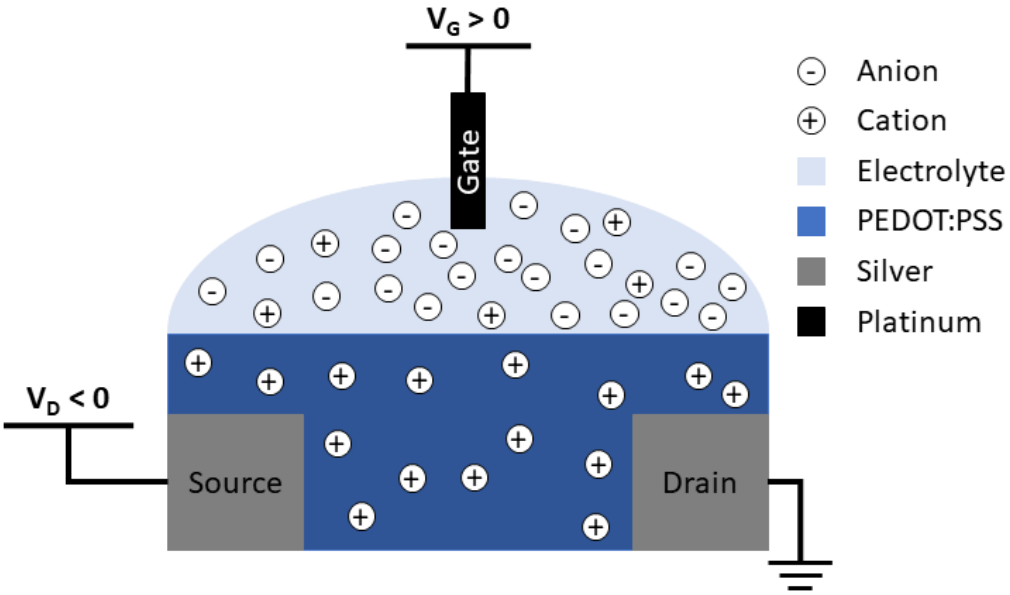

Figure 2.5 (a) OECT working principle, source, drain and gate metals may change depending on the intended application in this thesis silver and platinum are used. The cations are driven into the PEDOT:PSS channel, thereby de-doping the channel, lower the conductivity and decreasing the drain current.

2.3. Fabrication Techniques

2.3.1. Benefits of 3D Printing

Biosensors often need to be disposable for two main reasons. First, when bio-entities are being sensed, sanitation and sterilization need to be considered, meaning that disposability is often necessary to avoid cross-contamination and infection. Second, organic materials are generally less stable than inorganic materials that can quickly breakdown with use or when exposed to light or air, meaning the devices can only be used a finite number of times. For these reasons, the cost of these sensors must be drastically reduced to make them a more feasible option. This cost can be reduced with equipment, maintenance, labour and material costs, thereby lowering the overall cost of the biosensors.

Reducing the costs of biosensors requires a change in the fabrication technique used. In manufacturing, there are both additive and subtractive techniques. A subtractive manufacturing technique requires at least three general steps, material deposition, patterning and then etching. These processes require extra steps, each with their own equipment requirements and expertise, adding to the equipment and labour costs. In addition, the excess material that must be removed in the etching step, in most cases cannot be reused and is wasted, further adding to the material costs. Most OECTs are fabricating using microfabrication techniques [118,132–135], most of which are subtractive techniques. These techniques include photolithography, electron beam deposition, sputtering, chemical etching, thermal evaporation, RIE, spin-coating, etc. These processes require special equipment, facilities and staff to maintain them, meaning that there is an immense cost added to the devices. In the case of photolithography, which is widely used, for the desired pattern to be deposited, first a photomask must be designed and manufactured, meaning that the design and dimensions of the devices cannot be easily changed without great effort, time and cost. All these drawbacks can be avoided by using an additive manufacturing technique, like 3D printing.

An additive manufacturing technique only places material where it is desired, then the material is cured or sintered. Additive processes require fewer steps and are generally less complex, leading to lower equipment and labour costs. A big benefit of using organic semiconductors is that they are solution-processable, which means that more additive processes can be employed in fabrication. Additive processes allow for less labour, time, and material intensive processes unlike, subtractive manufacturing because they require less equipment, less material and no do not require specialized facilities like clean rooms. Also, some techniques, like 3D printing, allow for a quick and easy device design change, allowing for fast prototyping and customization. It can be as simple as changing a CAD drawing, as opposed to redesigning and manufacturing a photomask as with photolithography.

There are several different additive techniques available. These include screen printing, inkjet printing, gravure printing, and 3D printing. Screen printing is widely used for organic electronics, including OECTs[136–138]. Screen printing is a process that uses a mesh to transfer the ink onto the substrate through gaps in a stencil that only allows ink to be deposited in specific areas. Inkjet printing has also been used to fabricate OECTs [139,140]. This method simply deposits droplets of ink onto the substrate to print the desired pattern. Gravure printing is commonly used in roll to roll processing. The substrate is fed in between two cylinders that are rolled in opposite directions. One of these cylinders has the desired pattern engraved on it. While the cylinders are rolled, the substrate is fed through, the engraved cylinder is rolled in ink, the excess ink is bladed off and the pattern is deposited onto the substrate.

3D printing is the additive fabrication technique that was used for this work. There are several different kinds of 3D printing including, material extrusion, binder jetting, material jetting vat polymerization, and powder bed fusion. Material extrusion printing includes Fused Deposition Modeling (FDM), or Fused Filament Fabrication (FFF). This is a type of printing that melts and deposits the material in a selected pattern. Vat polymerization is a printing technique that uses micromirrors to shine light in the desired pattern. This light activates the crosslinker in a light-curable polymer resin, hardening it. The build head is raised, and another pattern is shone to build the 3D structure. This technique was briefly used in this work to make electrolyte wells. This is discussed further in the NOT gate concentration sensor section (Chapter 6). Powder bed fusion is a tie of printing that can be done with polymers, or metals and includes different techniques including, selective heat sintering (SHS), direct metal laser sintering (DNLS), selective laser melting (SLM), selective laser sintering (SLS) or electron beam melting (EBM). All these techniques use a powder ink that is sinter layer by layer. Binder Jetting is a printing technique that uses a binding agent that is deposited in a desired pattern onto a powder bed. The powder is bond together where the binding agent is deposited. Material Jetting is a printing technique that is used in this work. It is a process that deposits material in the desired pattern by moving either the printing head or the printing bed. The material is then cured either through UV curing, laser sintering, oven or hot plate curing. There are different kinds of material jetting including gas injection printing and aerosol jet printing, which are used in this work. These techniques are discussed in more depth below.

2.3.2. Gas Injection Printing (nScrypt Printing)

Some of the devices described in this thesis were printed using an nScrypt 3Dn-Tabletop 3D printing and micro-dispensing system. This system uses nitrogen gas to push the plunger of a syringe and force ink through a nozzle. There is a small actuator between the syringe and the nozzle that can be adjusted. The amount of material that is dispensed onto the substrate can be controlled by a combination of the actuator opening, the printing speed, the gas pressure and the nozzle size. An illustration of the working mechanism is in Figure 2.6. Depending on the viscosity and the particle size of the material being printed, these parameters must be adjusted to achieve the optimal parameters. The nozzles only come in set sizes, and therefore, changing the size is generally only adjusted to suit the particle size and the viscosity of the material. The printing speed is used to adjust the line thickness and width, while the actuator and pressure are used to adjust the amount of material being dispensed. In addition, the height of the nozzle to the substrate can be adjusted, this is important that the material can be precisely placed onto the substrate. If the nozzle is too high, the material will curl up back onto the printing nozzle, and or simply drip onto the substrate in an uncontrolled manner. If the nozzle is too close to the substrate, the nozzle can contact the surface and damage both the substrate and the nozzle. If it is not contacting the substrate but still too close, the material will have a V-shaped cross-section as the nozzle will push the material out of the way. The nScrypt printer is equipped with a build stage that can move the substrate in the x and y direction to control the pattern that the material is deposited in. A CAD drawing of the desired pattern is made, and then using proprietary software, the CAD drawing is converted into the path the printer will take. Depending on the line width that is being dispensed at the given parameters (speed, actuator height, pressure, nozzle size) the software must be adjusted so that the lines overlap to create a continuous film. The overlap between lines mustn't be too great as this will increase the thickness of the film, too small, and the film will have gaps. The nScrypt printer will then follow the path, closing the actuator, thereby stopping the flow of material when there is the end of a line. This allows for disconnected patterns to be created, as needed for electrodes. After the material is finished dispensing it is then baked, either on the bed of the printer, which has a built-in heater, on a hot plate or in an oven. After the material has been baked, it is possible to build on the design, adding other layers of different materials. The designs used in this thesis are described in subsequent chapters.

The nScrypt printer is equipped with a heated printing bed, which has a large temperature range, meaning that lower temperatures can help to remove solvent from the ink, preventing the printed line from spreading. Also, the printer bed can be raised to higher temperatures, allowing for projects to be cured in place, this helps to limit alignment errors when subsequent layers are printed. The nScrypt printer is also equipped with a laser for levelling, this helps to ensure that the printing bed is level so that the ink is dispensed from a consistent height from the substrate and the nozzle does not run into or scratch the surface.

The nScrypt printer can print a large range viscosity from 1 cp to 1,000,000 cps, however, the printer works best with higher viscosity inks. Low viscosity inks have a tenancy to spread and not make a nice uniform film when printing. The benefit of using this mode of fabrication is that an entire device can be printed with this single printer. Starting with a substrate, the metal electrodes are printed, then cured, the PEDOT:PSS channel is then printed and cured and lastly a masking material to prevent shorting of the source and drain is printed and cured. This method leads to consistent devices that can be quickly adjusted to test different configurations and device dimensions.

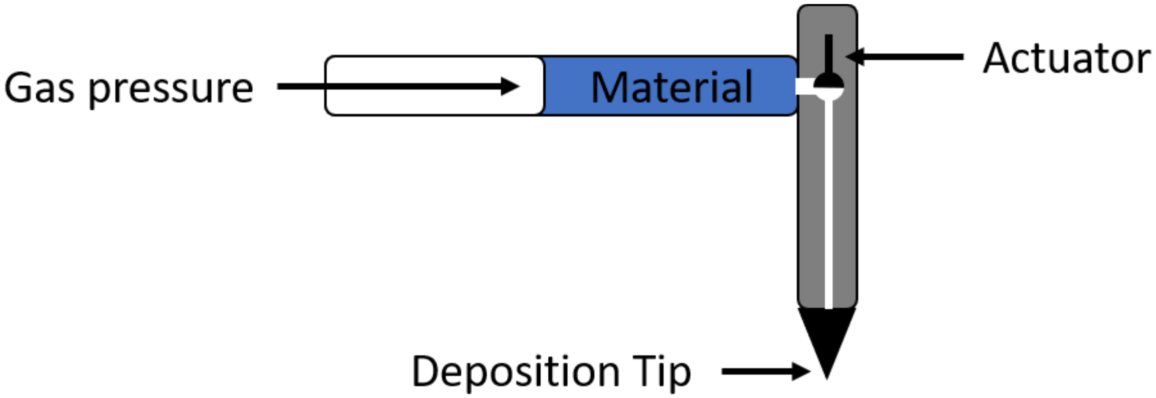

Figure 2.6 Image illustrating the working principle of a gas injection printer.

2.3.3. Aerosol Jet Printing (Optomec Printing)

A large majority of the devices in this thesis were printed using an Optomec Aerosol Jet® 5x System. This printer uses atomizers that agitate the ink dispersion to create an aerosol. A flow of nitrogen gas is flown across this aerosol, carrying it through a tube to the tip, where the stream of the aerosol is focused with another flow of nitrogen gas that acts as a sheath to focus the flow of material so that a fine line can be deposited. The stage moves in the x and y directions so that a pattern can be printed. The design is made in AutoCAD and then converted with a proprietary software into the path for the printer to take. The software requires to input the line spacing; this will ensure that a continuous film can be printed. A line spacing that is too large, will leave gaps in the film, while a line spacing that is too small will cause the film to become thicker. In addition, the software will curve the corners of the design, this is to prevent the motors from coming to a full stop and changing direction suddenly, leading to a build-up of material at every corner. By rounding the corners, the motors, will slow in one direction and speed up in the other simultaneously, leading to a smoother print and a more uniform film.

The Optomec printer has two options for atomizing the ink. The first is an ultrasonic atomizer (Figure 2.7), this atomizer uses sonic energy to sonicate the Nano-particle dispersion. A thin glass vial sits in a water bath, the bottom of the glass vial is thinned so that the energy from the water bath can more easily be transferred to the ink. The sonication creates an aerosol that is picked up by the nitrogen gas flow. This gas flow is carried in a tube to the deposition tip where it is focused into a stream by another flow of nitrogen gas called the sheath flow. The ultrasonic atomizer can be used to deposit materials that range in viscosity from 0.7 to 10cP.

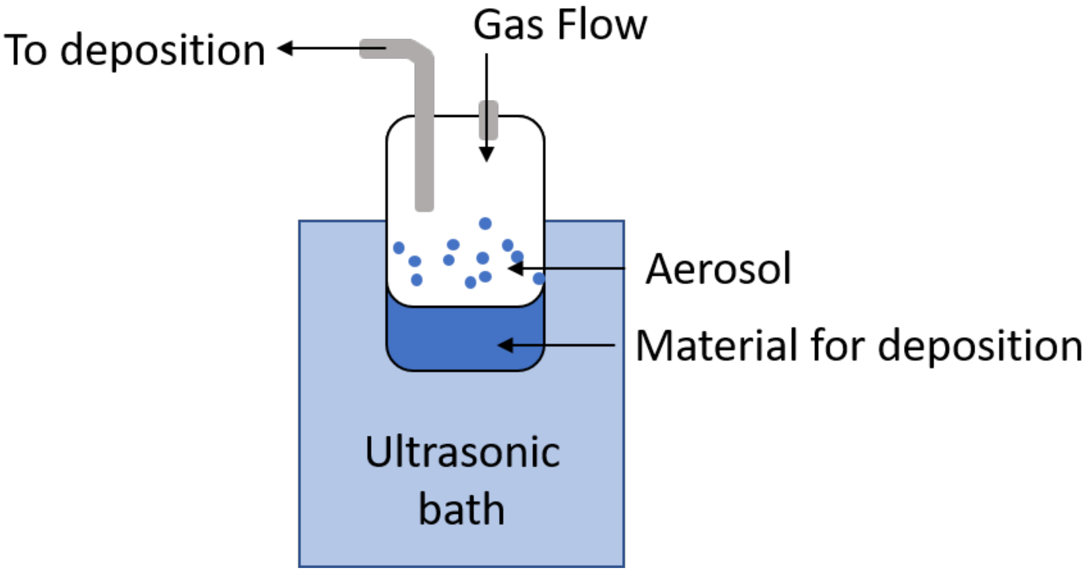

Figure 2.7 Ultrasonic Atomizer schematic used in the Optomec printer.

The other atomizer is pneumatic (Figure 2.8). This atomizer uses airflow to suck up the material into a tube, which is then sprayed against the side of the container thereby creating droplets that are then picked up by a flow of nitrogen gas, which runs through a virtual impactor. The virtual impactor condensed the aerosol and removes excess gas before the aerosol is carried to the tip, where a sheath flow of nitrogen is used to narrow the stream of material which is then deposited. This atomizer can be used to deposit material ranging in viscosity from 1-1000cP.

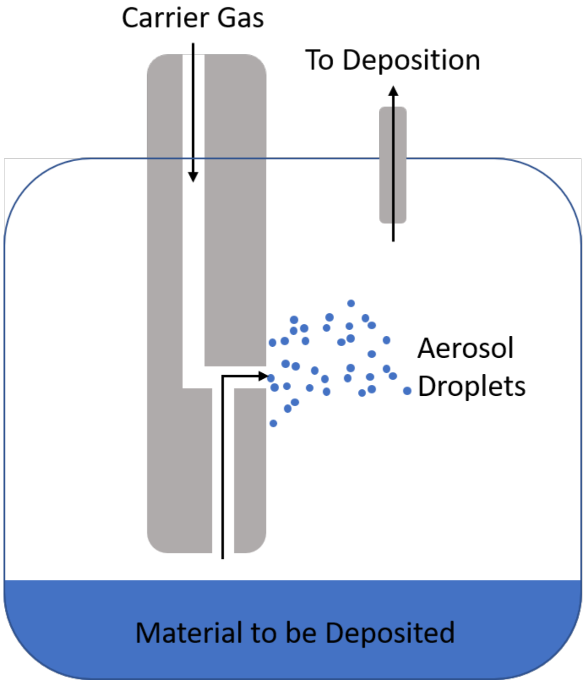

Figure 2.8 Pneumatic Atomizer used in the Optomec printer.

There are different types of tubing available Teflon, Polyethylene (PE) and PFA to carry the material from the atomizer to the deposition tip. Depending on the material being deposited, a different tubing can be selected, the polarity helps to choose the appropriate tube material. For water-based materials, PE tubing was used. The compatibility and the polarity of the material help to inform the choice of the tubing.

The Optomec printer can reach up to 10-micron resolution in the XY plane. This allows for high precision and small features to be printed. This printer is also equipped with a heated bed, which allows for better deposition of some materials. The heated bed can help to remove the solvent from the ink once it has been deposited, thereby limiting the spreading of the ink and maintain the fidelity of the printed line. Another feature of this printer is the heated pneumatic ink reservoir, with a magnetic stirrer. Being able to heat the ink reservoir allows ink to remain more viscous, allowing for easier deposition, while the magnetic stirrer keeps the ink consistent. There is also a

UV lamp (405 nm) that can be used for on the fly curing. This allows for the deposition of UV curable inks, such as UV curable PDMS. The UV lamp means that materials can be printed and then cured immediately, because of this, more precise patterns can be printed, as well as 3D structures built. The Optomec is also equipped with a laser (830 nm), the laser can be programmed to follow the same pattern as the printed ink, which sinters the ink with high precision. The laser can be beneficial for certain inks as it can allow for more uniform and conductive films, as compared to oven curing.

Another feature of the Optomec printer is a built-in alignment software routine. This feature uses an alignment camera to find alignment marks that are printed with the first layer, calculate the rotation and shrinkage and then adjust the subsequent layers so that they are properly aligned. This is necessary when the project is removed to be oven or hot plate cured and allows for more precision and control over device dimensions.

One of the major features of the Optomec printer is that the printing stage can be changed from a 3 axis to a 5-axis printing stage. The 3-axis printing stage has a vacuum platen that can hold the substrate in place and there is movement in the x, y and z planes. The 5-axis stage has movement in the x, y and z planes as well as two rotational axis A and B that are perpendicular to each other. The 5-axis stage allows for direct printing on 3D objects.

The Optomec printer has many features that make manufacturing quick and efficient. This system has high precision and can print a resolution down to 10 μm in the XY plane and less than 100 nm thickness. This printer can print inks ranging in viscosity from 1 cp to 1000 cps and works well with low viscosity inks. Also, this printer has an operating height of 3 to 5 mm from the substrate, as opposed to the nScrypt printer which has to be almost touching. This higher working distance allows for more flexibility with printing.

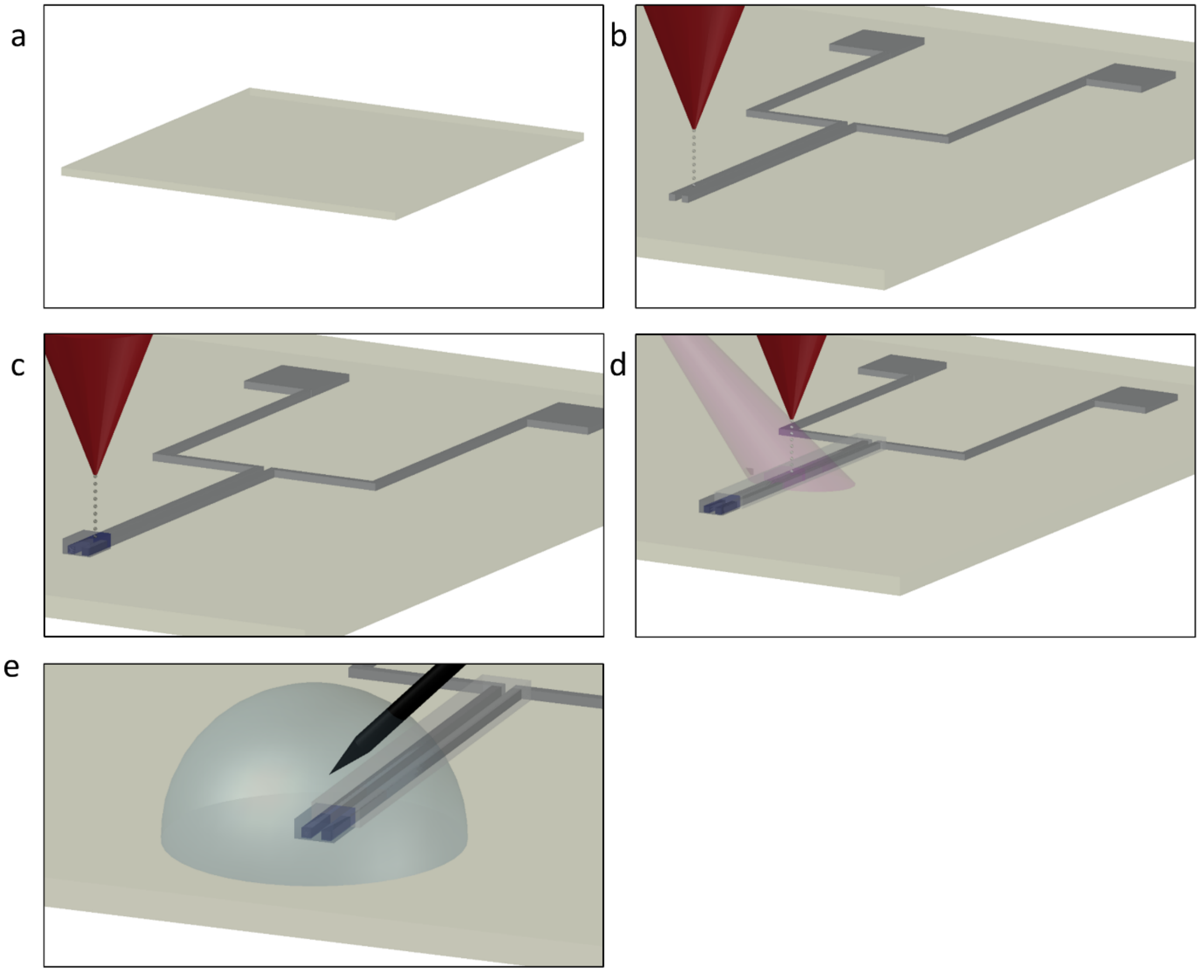

Figure 2.9 The process flow for device manufacturing. (a) Start with a substrate, typically Polymide, PET or Parylene. (b) Deposition of electrodes using nanoparticle inks, typically with silver. The electrodes are then cured by oven curing. (c) Deposition of the channel material. Typically, PEDOT:PSS which is then oven cured. (d) Deposition of the masking material, PDMS. This is cured on-the-fly with a UV light exposure and oven cured afterwards. (e) This is the complete device with an electrolyte bead on the channel. The device is tested using an external gate probe.

2.4. Characterization Techniques

2.4.1. 4-Point Probe

The four-point probe, also called Four-terminal measurements, is a method to directly measure the sheet resistance. For this work, a Lucas Pro4 4000 with a Keithley 2601A source meter was used. The four-point probe is a simple device that uses four equally spaced probes, on the Lucas Pro they are 0.04 inches (1.016 mm) apart. The probes are arranged in a line. Current is passed through the outer two probes, which induces a voltage that is measured with the inner two probes. The voltage can be measured, without drawing current, thereby eliminating the contact resistance in the measurement, leading to a more accurate measurement. This is illustrated in Figure 2.10.

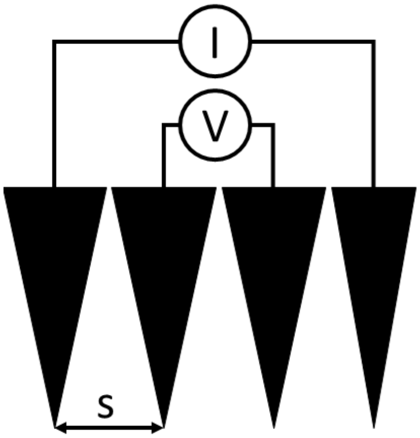

Figure 2.10 Schematic showing the connections on a four-point probe system. The current is applied between the two outer probes while the voltage is measured using the two inner probes.

If the sample is bulk and of semi-infinite volume, in other words, when the sample thickness (t) is much greater than the space between the probes (s) (t>>s). In this case, resistivity is expressed as Equation 2.8.

$$\rho_0 = 2\pi s\left(\frac{V}{I}\right) \qquad 2.8$$

Where s is the spacing between the probes, V is the voltage and I is the current and the subscript 0 indicates, that this the resistivity for a bulk sample. The actual resistivity $\rho = \rho_0$ when it is a bulk sample. However, for finite samples, $\rho \neq \rho_0$ and correction factors must be used to give a more accurate resistivity measurement. There are several correction factors that need to be used depending on the circumstance of the measurements [141]. Primarily, if the distance of the probes to the edge of the sample is greater than 5 times the spacing between the probes (5s), then there is no need for a correction factor[142]. However, if the thickness of the sample is less than 5 times the distance between the probes ($t \leq 5s$ or in the Lucas Pro4 4000 case $t \leq 5.08\, mm$), then the equation (2.9) for resistivity becomes as follows

$$\rho = f_1 f_2 \rho_0 = 2 f_1 f_2 \rho = \frac{\pi t}{ln2}\left(\frac{V}{I}\right) f_1 f_2 \qquad 2.9$$

Where f_1 is the finite thickness correction factor and f_2 is the finite width correction factor. The correction factor is a function of $\frac{t}{s}$. For samples that are semi-infinite in volume (t>>s) $f_1 \approx 2\ln(2)\frac{s}{t}$ which leads to Equation 2.10.

$$\rho \approx 2\pi s\left(\frac{V}{I}\right) f_2 \qquad 2.10$$

To calculate the sheet resistance, which has units of $\Omega/square$, the resistivity can simply be divided by the thickness, giving Equation 2.11.

$$R_s = \frac{\rho}{t} \qquad 2.11$$

Where the R_s is the sheet resistance. From this, the resistance, with units of Ω, can be calculated using Equation 2.12.

$$R = \frac{l}{w} R_s \qquad 2.12$$

Where l is the length, w is the width of the sample.

When measuring with a four-point probe, it is important to measure away from the edge as to avoid, edge effect, which will change the measurement results due to the edge geometry. To avoid edge effect, the distance of the probes to the edge of the sample must be greater than 5 times the spacing between the probes (5s). At this point, there is no need for a correction factor[142]. For small samples, when this cannot be avoided however, a correction factor must be used depending on the geometry of the sample. The two most common geometries are a circle and a rectangle.

The approximate geometry, size and shape of the substrate is entered the software, which takes care of the correction factor.

2.4.2. Profilometry

Profilometry is used to determine step height changes and is perfectly suited to measure thicknesses of films or traces on a substrate. In this case, the profilometry was done using an Alpha-Step IQ in the nanoFAB at the University of Alberta. Profilometry works by dragging a stylize across the surface of the substrate. The stylus is connected to a transducer so that changes in the surface profile will lead to changes in the electrical signal being sent to the computer. The limitations of this device are the stylus size and shape. A large stylus cannot measure extremely rough surface profiles with deep cracks. The alpha step IQ has a stylus with a 5 µm radius. This is illustrated in Figure 2.11.

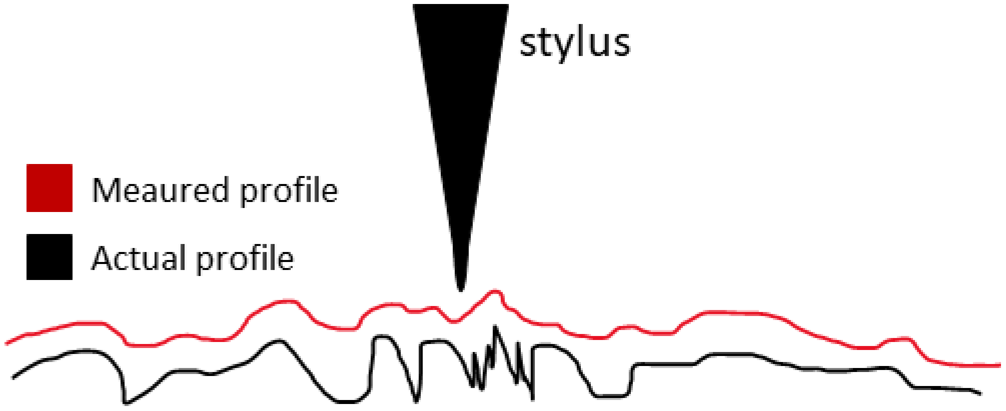

Figure 2.11 The black line shows the actual profile while the red line shows the measured profile.

2.4.3. Fixed Angle Ellipsometry

Fixed angle ellipsometry was used to determine thin layer thicknesses. In this case, a Filmetrics F10-UV was used in the nanoFAB at the University of Alberta. This system transmits light, normal to the material surface, then measures the reflectance coming back to the detector. At every medium change (change in the material) light will be reflected, transmitted or absorbed. The reflections are the measurements collected by the ellipsometry system. The amount of light that is reflected off a surface is determined by the n and k values of that material, which are the real and imaginary components or the refractive index n*, such that $n^* = n + ik$. The relationship is described by Equation 2.13.

$$R = \frac{(n-1)^2 + k^2}{(n+1)^2 + k^2} \qquad 2.13$$

When light passes through a material or a stack of materials, there will be a reflection at every surface, in other words, at every medium change. This means that there will be multiple waves of light that are reflected that will interact. Each of these waves will either be in phase and constructively combine or will be out of phase and deconstructively combine. This is shown in Figure 2.12.

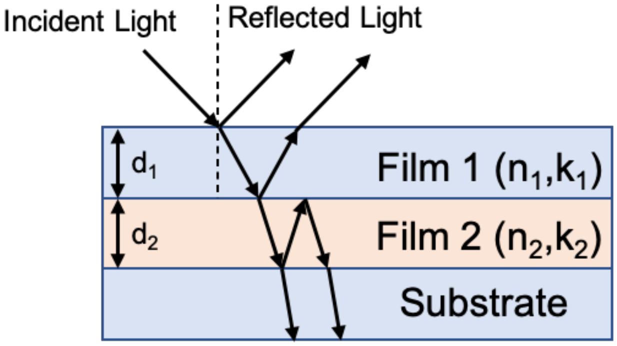

Figure 2.12 An image showing the material stack up and light reflection and transmission.

2.4.4. Source Meter

A Keithley Source meter was used to measure the IV Characteristics of devices. A source meter can simultaneously apply and measure both current and voltage. In this case, two different source meters were used, a Keithley 4200-Semiconductor Characterization System (SCS Parameter Analyzer) with a probe station as well as a Keithley 2612b which is controlled using a custom LabVIEW program. Source meters can use either four-point or two-point measurements. Two-wire measurements simply connect the Device Under Test (DUT) so the Force HI and LO connections. However, Four Wire connections connect one side of the DUT to the sense and Force HI and the other side of the DUT to the Force and Sense LO. Four-wire sensing is best used when measuring and/or sourcing in low impedance circuits. The four-wire connections are shown in Figure 2.13 and the Two-wire connection is shown in Figure 2.14.

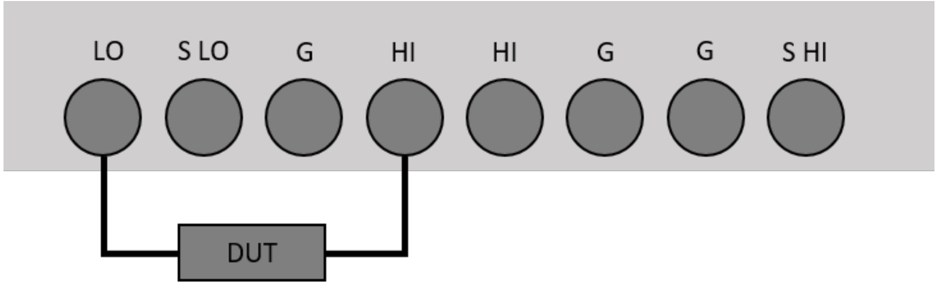

Figure 2.13 Connections for two-wire measurements.

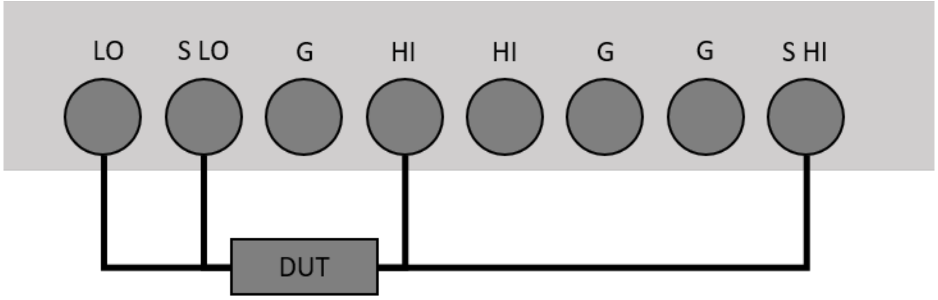

Figure 2.14 Connections for four-wire measurements.

2.4.5. LabVIEW

LabVIEW is a programming software from National Instruments. It is a visual programming language, meaning that blocks are dragged and dropped into place instead of writing the code. LabVIEW was used to program a Keithley 2612b source meter to work for various electrical tests. Signal generators were coupled with the source meter for different measurements.

3. OECT Characterization

To use OECTs as sensors and in logic gates, it is important to first characterize them in order to gain insight into their electrical properties including their sensitivity, their threshold voltage and their current levels. One of the main methods for OECT characterization is done by using a source meter (Keithley 2612B), coupled with micro-positioner probes. The gate of the device is connected to one Source Measurement Unit (SMU) of the source meter and the source is connected to another SMU. The drain is connected to ground. The biasing of the device is shown in Figure 3.1. Once the OECT is connected different tests can be undertaken. The main test done on the devices is an IV sweep, where the drain voltage is swept, and the current is measured at a set gate voltage. Several IV sweeps are done at various gate voltages and compiled into a graph called a family of curves. In other words, the gate voltage is applied, the drain voltage is swept, then the gate voltage is stepped up and the drain voltage is swept again. This is repeated for several gate voltages. These curves are crucial to determine when the OECTs are turning off and on and to determine the threshold voltage of the device.

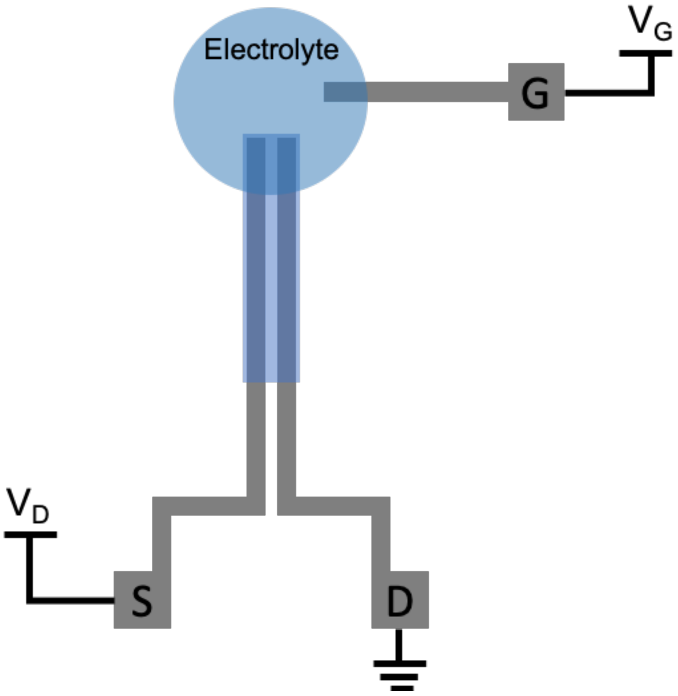

Figure 3.1 Biasing of an OECT device. The source, the gate and the drain are marked by S, D and G respectively. The electrolyte is presented as a blue circle and is labelled as such. The source has a voltage applied, while the drain is grounded. The gate voltage has another separate voltage applied.

A family of curves is shown in Figure 3.2 and Figure 3.3. In addition, several other parameters can be extracted from the family of curves. This includes the transconductance (g_m) and the transfer curve. These curves are generated by selected a specific drain voltage and extracting the corresponding drain currents at each gate voltage. These curves indicate the sensitivity of the device and can indicate the operating voltages at which the device has peak sensitivity and therefore peak performance. As discussed in the background chapter, the transconductance curve is the ratio between the change in the drain current to the change in the gate voltage ($g_m = \delta I_D / \delta V_G$), this is then plotted against the gate voltage. The peak transconductance indicates the peak sensitivity of the device. The transfer curve is a plot of the drain voltage plotted versus the gate voltage. The transfer curve shows the corresponding drain current to the gate voltage. The transfer curve shows the operating current of the device and allows for different devices to be compared as the operating currents can vary from device to device.

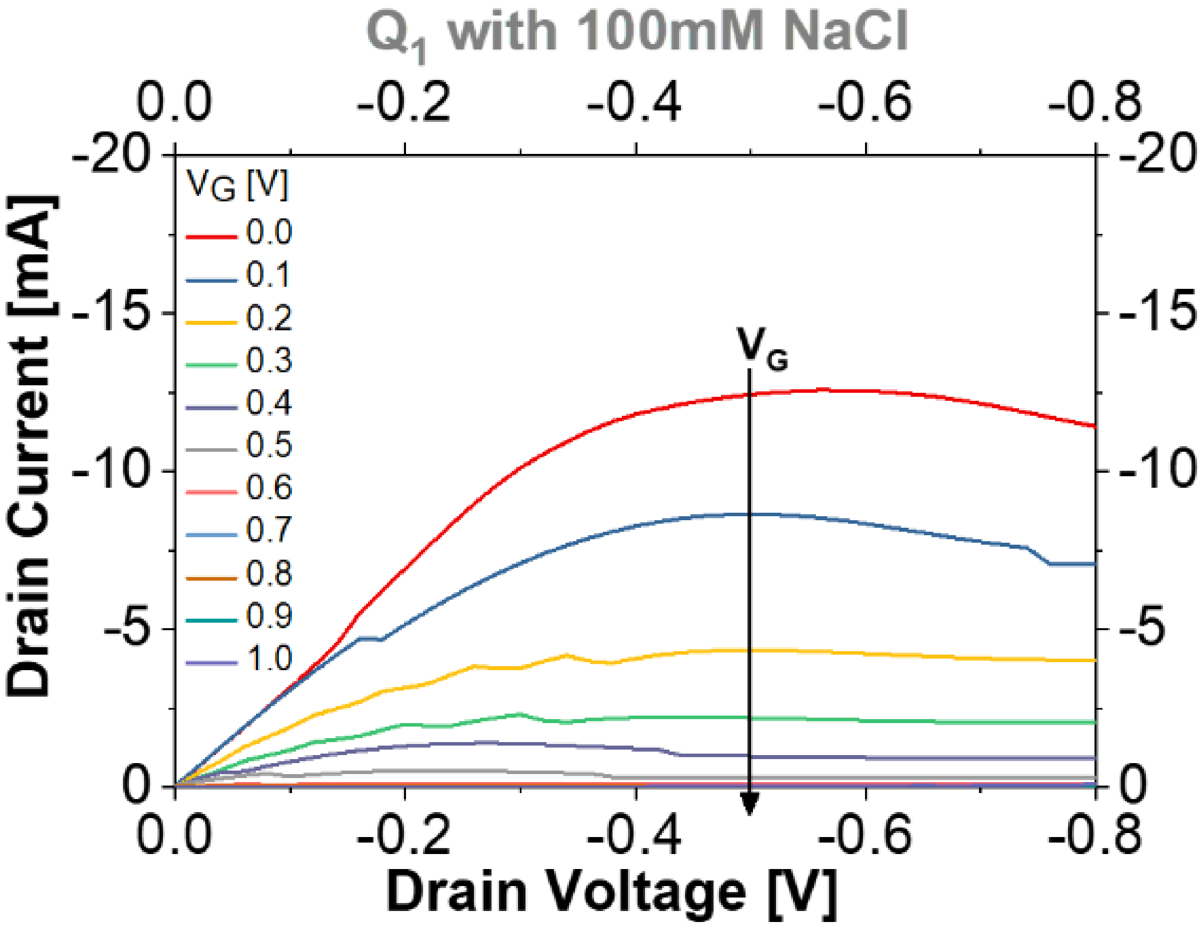

Figure 3.2 This is the family of curves for an nScrypt printed OECT tested with a silver gate and 100 mM NaCl. The transfer and transconductance curves are extracted from these curves. This image was first published in the supplementary document in a paper by Majak et al.[1]

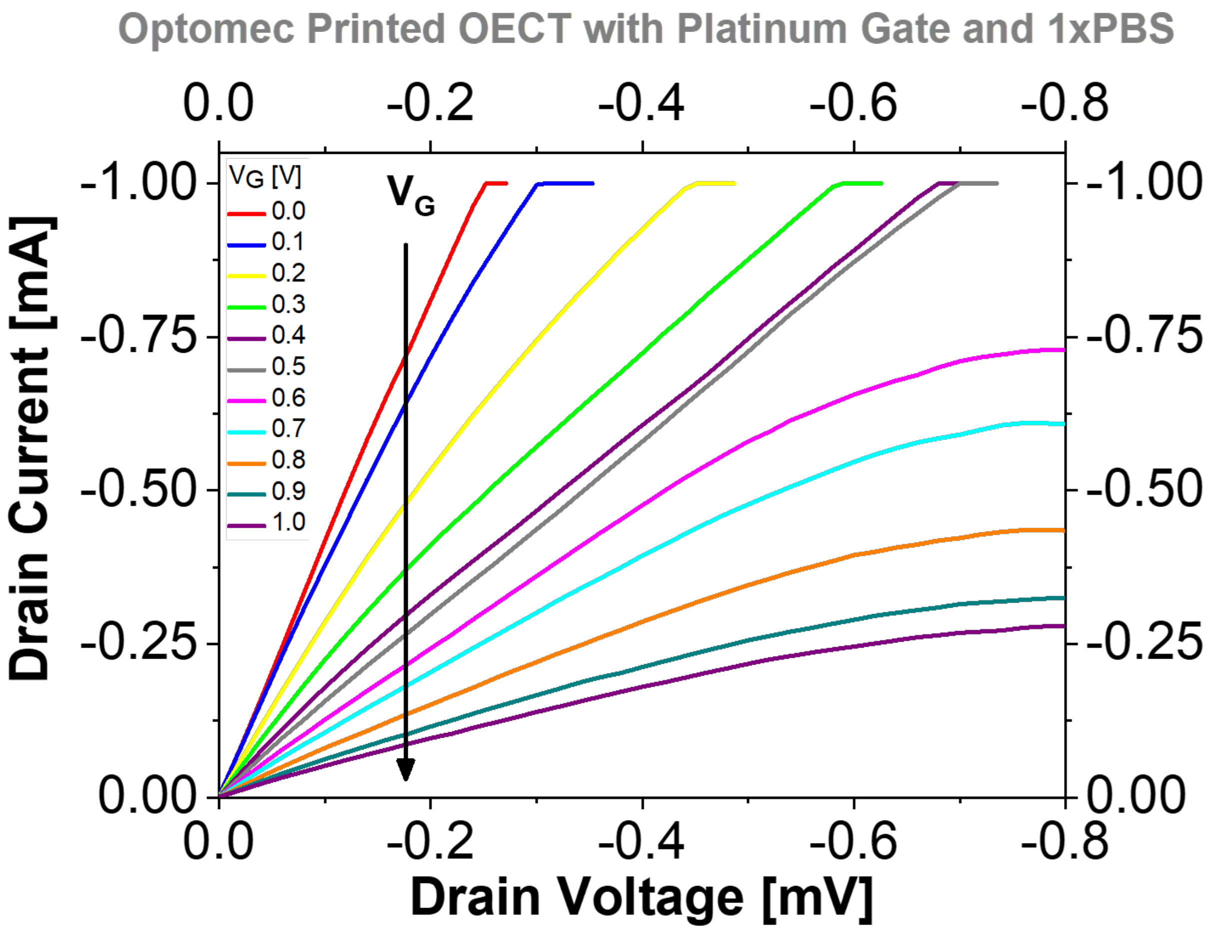

Figure 3.3 The family of curves for an Optomec printed OECT. This device used a platinum gate and 1xPBS electrolyte. The transfer and transconductance curves are extracted from this data.

As discussed in the background chapter (Section 2.2.1), the OECTs drain current follows Equation 3.1.

$$I_D = \mu d C^* \frac{w}{l}\left(V_T - V_G + \frac{V_D}{2}\right) V_D \qquad 3.1$$

From this, it is clear the drain current is dependent on the w/l ratio. This ratio is the width to length ratio of the channel of the OECT. The w/l ratio also directly affects the transconductance as illustrated in Equation 3.2 for transconductance.

$$g_m = \frac{\delta I_D}{\delta V_D} = \mu d C^* \frac{w}{l}(V_T - V_G) \qquad 3.2$$

Therefore, from the transconductance curve, the optimized w/l ratio can be determined. In addition, from these two equations, it is clear that the drain current and the transconductance are dependent on the channel thickness (d). The w/l ratio can easily be adjusted in 3D printing by simply adjusting the CAD files that are used to print the channel material. The channel thickness can be adjusted by changing the printing parameters. These parameters vary depending on the printer being used. The optimization of the thickness and the w/l ratio were mostly carried out by another group member, Jiaxin Fan and the optimized parameters were used to build the sensors described in this thesis.

As discussed previously, there are two main fabrication methods used in making the sensors discussed in this thesis. Gas injection 3D printing using an nScrypt 3Dn-Tabletop 3D Printing and Micro-Dispensing System and aerosol jet 3D printing using an Optomec Aerosol Jet® 5x System. These two printing methods use different materials and have different dimension capabilities and therefore the devices that the devices produce have different characteristics.

One of the main differences between the Optomec and the nScrypt printers are the inks that are used for the PEDOT:PSS. Due to the ability of the Optomec to print high viscosity materials, the PEDOT:PSS ink used has very low viscosity, which allows for extremely thin channels to be printed. However, the viscosity of the ink used in the nScrypt is high and it is difficult to print thin channels. Also, there can be discrepancies between different devices printed with the same method due to slight changes in the ink consistency, buildup in the deposition tubing and adhesion to the substrate. This is another reason to characterize the OECTs is to ensure that devices with similar devices are used when measurements are to be compared.

The family of curves for the nScrypt printed OECTs are shown in Figure 3.2. The transfer/transconductance curves that were extracted from the family of curves for the nScrypt printed OECT are shown in Figure 3.4. These devices used a silver gate and 100 mM NaCl as the electrolyte. Both Figure 3.2 and Figure 3.4 are reprinted from a paper published in Elsevier's Sensors and Actuators B: Chemical[1] and reprinted here with permission. The family of curves for the Optomec printed OECTs is shown in Figure 3.3 and the transfer/transconductance that was extracted from it are shown in Figure 3.5. The Optomec printed OECTs were tested using a platinum gate and 1xPBS. Due to the platinum gate, the family of curves shows that the device does not fully turn off. This is due to the redox potential of platinum being higher (1.188 V[143]) than the applied gate voltage of 1 V. This is explained further in Chapter 4.

Table 3.1 Comparison of nScrypt and Optomec printed devices.

Printer	**nScrypt**	**Optomec**
Family of Curves	Figure 3.2	Figure 3.3
Transfer and Transconductance Curve	Figure 3.4	Figure 3.5
PEDOT:PSS Ink Conductivity	0.0139 S/cm[1]	~270.27 S/cm
Channel Thickness	9.056 ± 0.559 μm[1]	~600 nm
w/l ratio	2.286[1]	~5
Gate Electrode	Silver	Platinum
Peak Transconductance	43.32 mS	2.54 mS

As seen in Table 3.1 there are many differences between the nScrypt and Optomec printed devices, including the transconductance and current levels between the two printing methods. The Optomec has a lower transconductance and a lower drain current. This is due to the different dimensions and the materials used in the construction, including the conductance of the silver electrodes and the mobility of the PEDOT:PSS channel. The ink used with the nScrypt printed has a much lower conductivity than that of the Optomec. Also, the two printing methods produce a channel of very different thicknesses leading to a very different transconductance. The nScrypt channels have a thickness of much thicker channel but a smaller w/l ratio than the Optomec printed devices. In addition, the characterization of different devices using the same printing method can be important as there can be slight variations due to many factors including changes in ink consistency, solvent evaporation, material buildup in the deposition tube, adhesion issue with the substrate, etc.

The transconductance of the nScrypt printed devices peaks at 43.32 mS which is very high, while the Optomec printed devices peak at 2.54 mS. This compares to some of the highest OECT transconductance values reported in the literature. Including microfabricated ones with a transconductance of 4.0 mS[134] or Inkjet-printed OECTs with a transconductance of 1.67 mS[144].

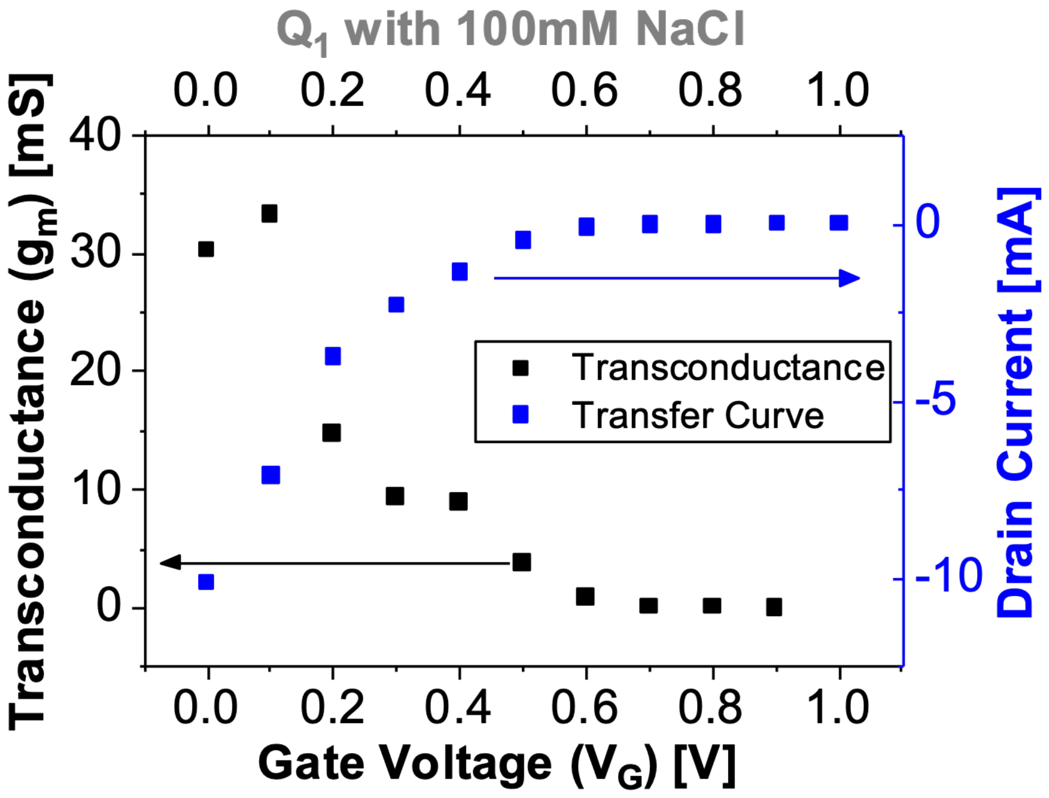

Figure 3.4 Transconductance and transfer curves for an nScrypt printed OECT characterized with 100 mM NaCl. This OECT used a silver gate. This image was originally published in Elsevier's Sensors and Actuators B: Chemical[1] *and is reused here with permission.*

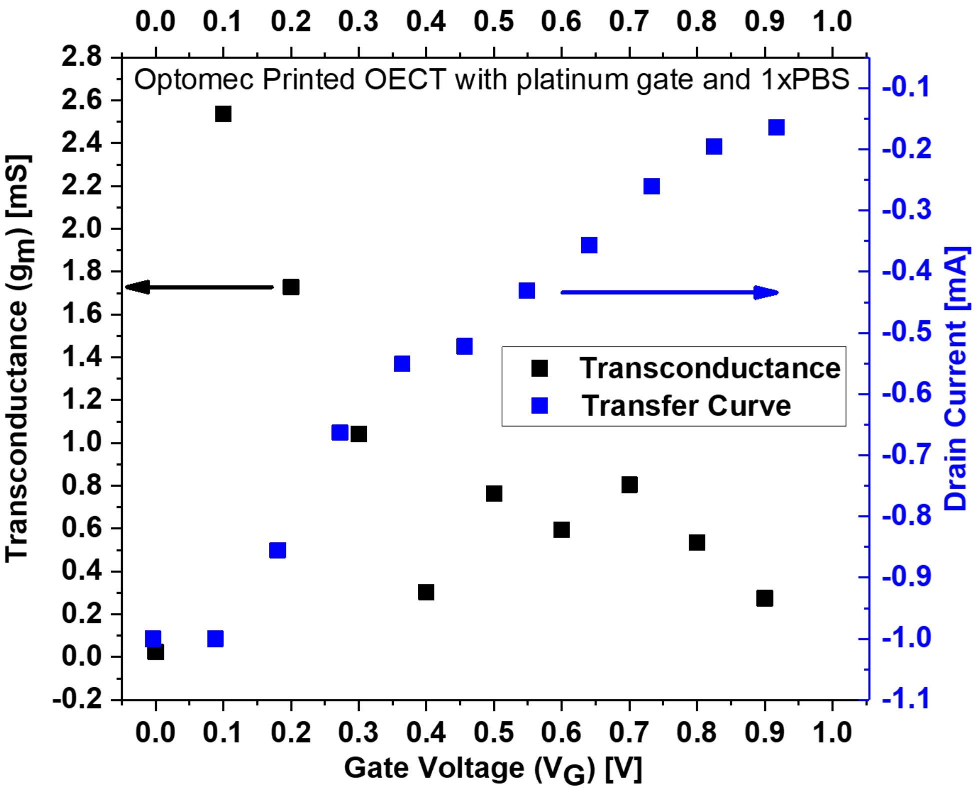

Figure 3.5 Transconductance and transfer curves for an Optomec printed OECT using 1XPBS as the electrolyte and a platinum gate.

The characterization of OECTs is integral to understand device performance. This characterization can be done through three different curves, the family of curves, the transconductance curve and the transfer curve. This gives insight into the threshold voltage, the on/off current, the sensitivity, and the current levels of the device. These characterization techniques can be used to optimize the OECT channel dimensions as the drain current and the transconductance are directly proportional to the w/l ratio and the channel thickness (d). OECT characterization is also used to select the V_G and V_D for the appropriate operating point of the OECTs, such that the device is in the linear region and has high transconductance. OECT characterization is simple but effective.

4. Fully 3D Printed OECT Based Δ9-Tetrahydrocannabinol (THC) and Melatonin Sensors

4.1. Introduction

Δ^9-Tetrahydrocannabinol (THC) is the psychoactive ingredient in cannabis products, many of which have either been decriminalized or completely legalized in various jurisdictions throughout the world. Canada became the first country in the G7 to legalize cannabis in 2017, while it is decriminalized in Portugal, the Netherlands, and various states in the USA. With the legalization of cannabis consumption, it is an increasing concern to regulate its use and keep the public safe. Because THC is psychoactive, it is important that cannabis users do not consume THC and operate motor vehicles, heavy machinery, or perform tasks that could be harmful or dangerous if not performed carefully. However, despite legalization, THC impairment remains difficult to test. THC levels in urine, blood and hair are difficult to relate to impairment. THC in blood is difficult, especially for roadside testing, as blood tests often require the suspect to be transported to a secondary location where the blood sample can be taken. The issue arises here as THC enters the blood quickly after consumption but then quickly leaves to enter lipophilic compartments in the body[145]. THC remains in blood three to ten minutes[146,147]. In urine the THC levels peak within two hours, however mostly metabolites are used to sense THC consumption, these can last up to several days in urine[148]. Therefore, a more accurate indicator is THC levels in saliva[149]. There have been a few sensors, demonstrating THC saliva testing including electrochemical detection[39–42], radioimmunoassay[48], fluorescence immunoassay[58,59], liquid chromatography-mass spectrometry[43–47], gas chromatography-mass spectrometry[49–57], thin-layer chromatography and mass spectrometry[60]. However, these devices are not reliable for THC saliva testing for roadside testing, as would be used by law enforcement.

Our solution to this issue is to use Organic electrochemical Transistors (OECTs) to sense the THC concentration. As described in the background chapter (Section 2.2), these OECTS use the organic semiconductor PEDOT:PSS, which electrochemically active meaning that the OECTs work with an electrolyte. The working principle of OECTs and PEDOT:PSS are described in length in the background chapter (Section 2.2). The use of OECTs for THC detection are meant to be single-use, disposable sensors to avoid cross-contamination and false positives.

These same OECTs were also used to sense melatonin hormone levels. Melatonin is known as the sleep hormone as it is responsible for the regulation of sleep. Melatonin levels can also be linked to various diseases including, type 2 diabetes[150], prostate cancer[151] and breast cancer[152]. The study of melatonin levels is of great interest to the military, and others. Melatonin has been detected using graphene-based sensors[31], nitrogen-doped graphene-based sensors [30] molecularly imprinted polymer sensors [33–35], ZnO nanorods modified carbon paste electrode[32], nano palladium-based sensors[36], cyclic voltammetry using glassy carbon electrodes [37], fast-scan cyclic voltammetry [38] and more. Fast, reliable and portable sensing of melatonin concentrations in body fluids would be beneficial. OECTs are perfectly suited for ‘wet’ sensing, and therefore perfectly suited for melatonin sensing. These OECTs, for the detection of melatonin, are meant to be single-use, disposable sensors to avoid cross-contamination and false positives.

4.2. Materials and Methods

4.2.1. Fabrication and Materials

These devices were designed in four layers. The first layer was a polymer substrate that was Kapton RK-08277-84, purchased from Cole Parmer, which had no adhesion promoted and was 25.4 µm. The second layer was a deposition of silver electrodes, using the ultrasonic atomizer on the Optomec 5x printer. The silver was a nanoparticle dispersion, Clariant PRELECT® TPS 50, the silver was cured at 140ºC overnight. The silver electrodes are 100 µm wide and about 2.45 µm thick and the resistivity is $5x10^{-6}$ Ω-cm.

The third layer is a PEDOT:PSS channel was printed using the ultrasonic atomizer. The PEDOT:PSS ink was made using, Heraeus Clevios TM PH 1000 at 79 v/v%. Ethylene glycol was added by 20 v/v% as a conductivity promoter[153,154]. Then, to change the surface tension and to minimize the contact resistance dodecylbenzenesulfonic acid solution (DBSA) (70 wt. % in isopropanol) was added by 0.1 v/v %[155]. (3-Glycidyloxypropyl)trimethoxysilane (GOPS) (≥98%) was added by 0.9 v/v% to act as a cross-linker. The ingredients were mixed in a nitrogen environment. The PEDOT:PSS ink, which was then printed as the channel with a W/L ≈ 5 and a thickness of ~600 nm and a resistivity of ~0.0037 Ω-cm. The PEDOT:PSS ink was cured at 130º C for 15 minutes.

The final layer was a mask that was printed over the electrodes, to ensure that shorting does not occur when electrolyte was added. The mask was printed using a PDMS mixture 1:1 v/v% PDMS (KER-4690-A): crosslinker (KER-4690-B) mixture from Shin-Etsu Chemical Co., Ltd. which was then diluted with hexane 3:1 v/v% to improve the viscosity for printing with the pneumatic atomizer. The ink was heated to 30ºC and constantly stirred throughout printing. While depositing the ink was exposed to UVA light (13.4 W/cm^2). A final bake was done to anneal the layer at

130ºC for 30 minutes. The layer is approximately 1-2 µm. The stack-up of the device is shown in Figure 4.1 (a), an optical microscope image of the OECT is shown in Figure 4.1 (b) and a Scanning Electron Microscope (SEM) image shown in Figure 4.1 (c). The fabrication of these devices is also illustrated in Figure 2.10.

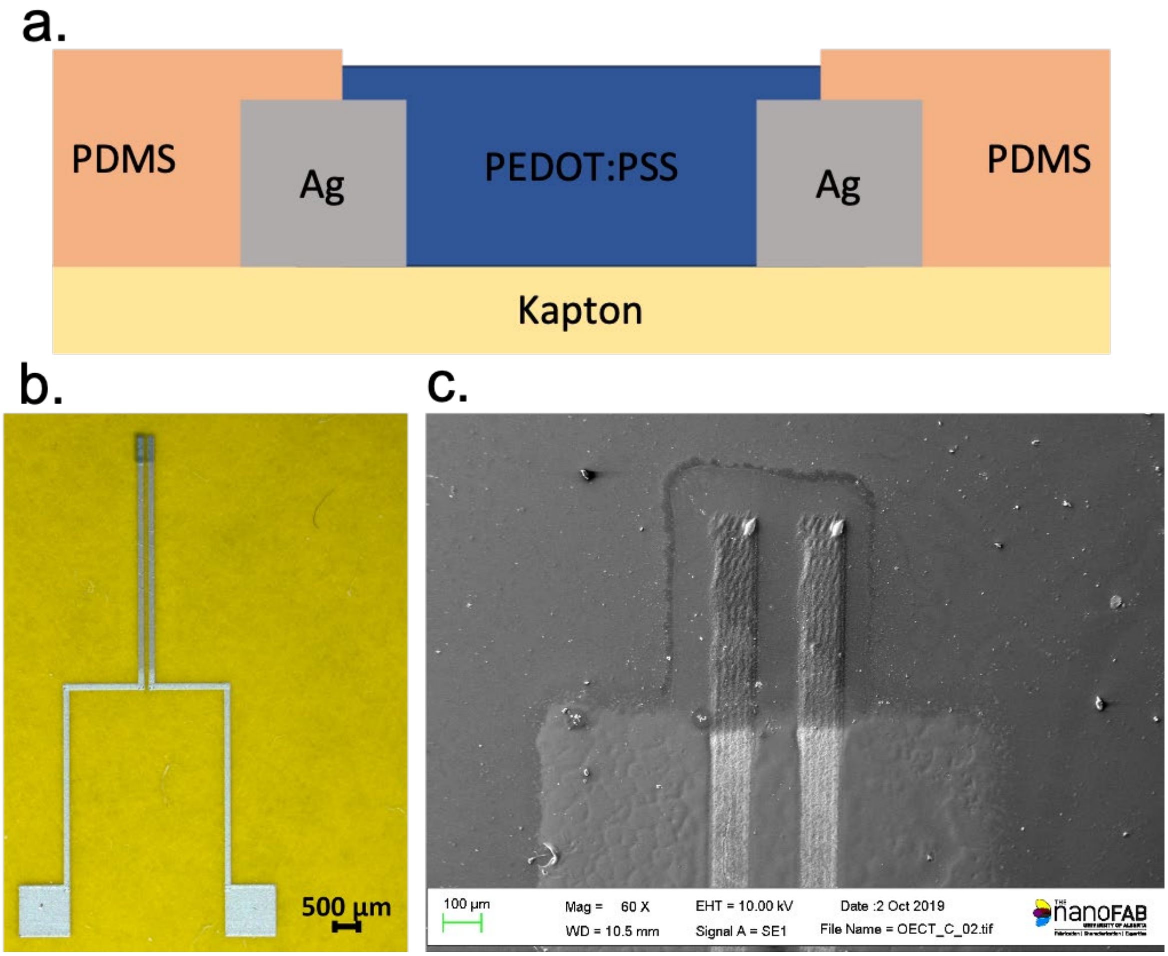

Figure 4.1 (a) This is the cross-section of the OECT construction. The OECTs are constructed in four-layer. The Kapton substrate, then the silver electrodes, then the PEDOT:PSS channel and finally the PDMS mask. (b) Optical Microscope image of the OECTs used for sensing with a 500 µm scale bar. (c) A Scanning Electron Microscope image of the OECT showing the OECT's channel with a 100 µm scale bar.

4.2.2. Measurements and Characterization

The electrical measurements were done using a customized LabVIEW program with a Keithley 2612b source meter. Several tests were performed on the devices. First, a family of curves was collected for different concentrations of THC. A family of curves is a measurement of drain current (I_D) versus drain voltage (V_D) for separate gate voltages (V_G). This is shown in Figure 3.3. The gate voltage is set and then the drain voltage was swept from -0.2 V to 0.8 V back to -0.2 V in steps of 0.02 V. The gate voltage was stepped from 0 V to 1 V in steps of 0.1 V. These measurements indicate that the OECTs do no fully turn off, this is due to the redox potential of platinum is greater than the applied gate voltage (1.188 V[143]). This means that platinum, will not transfer electrons until the gate voltage is greater than 1.188 V is applied. It is important to compare similar devices with similar current levels. When a device is tested with DI water, a higher resting current. When the OECT is tested with THC, the current level drops, when tested with melatonin the current level increases.

4.3. THC Detection Theory

THC can be detected using an OECT due to its redox curve. Considering that the anodic peak occurs at 0.025 V when using a platinum working electrode[156], while other studies indicate an anodic peak at 0.0 V when using a glassy carbon electrode[157]. This means that the THC oxidizes, meaning that an electron is released, in this case, the most likely occurrences is that a hydrogen is lost from the hydroxyl group, meaning that an electron is released into the electrolyte. This electron is removed by the platinum gate. The structure of the THC and the reaction are shown in Figure 4.2. This means that the electron double layer that is present at the gate-channel interface is reduced. When the electron double layer is reduced, the gate-electrolyte capacitance is decreased, which in turn increases the effective gate voltage that is applied to the channel, thereby lowering the drain current magnitude. The shift in the effective gate voltage can be shown when considering the Nernst Equation[158], as shown in Equation 4.1.

$$E_{Nernst} = E^{0'} + \frac{k_B T}{ne} \ln\left(\frac{[Ox]}{[Red]}\right) \qquad 4.1$$

Where E_{Nernst} is the Nernst potential, k_B is the Boltzmann constant$\left(1.38 \times 10^{-23}\,\frac{m^2 kg}{s^2 K}\right)$, T is the temperature in kelvin, n is the number of electrons transferred, and e is the fundamental charge $(1.60217662 \times 10^{-19} C)$. Also, $[Ox]$ is the concentration of the oxidized part and $[Red]$ is the concentration of the reduced part. $E^{0'}$ is the formal potential where $E^{0'} = \frac{V_G}{1+\gamma}$, where V_G is the gate voltage, and $\gamma = C_{CE}/C_{GE}$ where C_{CE} is the capacitance at the channel electrolyte interface and C_{GE} is the capacitance at the gate electrolyte interface. In addition, $V_G^{eff} = (1+\gamma)E_{Nernst}$ where V_G^{eff} is the effective gate voltage. This means that Equation 4.1 can be re-written as Equation 4.2.

$$V_G^{eff} = V_G + (1+\gamma)\frac{k_{Bz}T}{e}\ln([THC(Ox)]) \qquad 4.2$$

From Equation 4.2 it is obvious that as the concentration of THC increases, the concentration of the oxidized THC will increase, this increases the effective gate voltage, which in turn decreases the drain current magnitude in the OECT, as it is a depletion mode device.

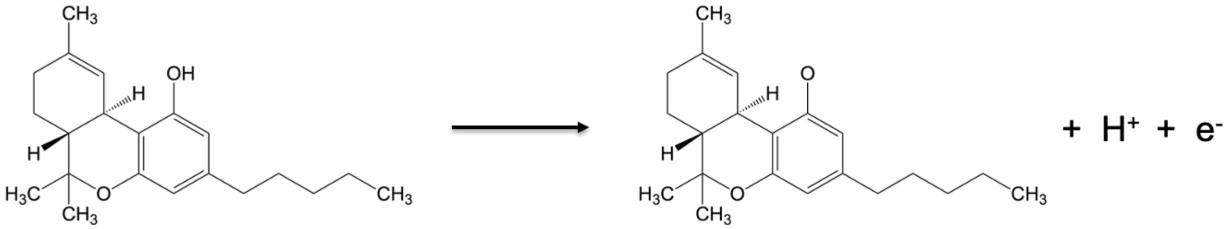

Figure 4.2 THC reaction showing the oxidation of THC. Oxidation, releases and electron that is removed by the platinum gate of the OECT, this increases the effective gate voltage, thereby decreasing the drain current magnitude of the device, meaning the device is turning off with an increase in concentration.

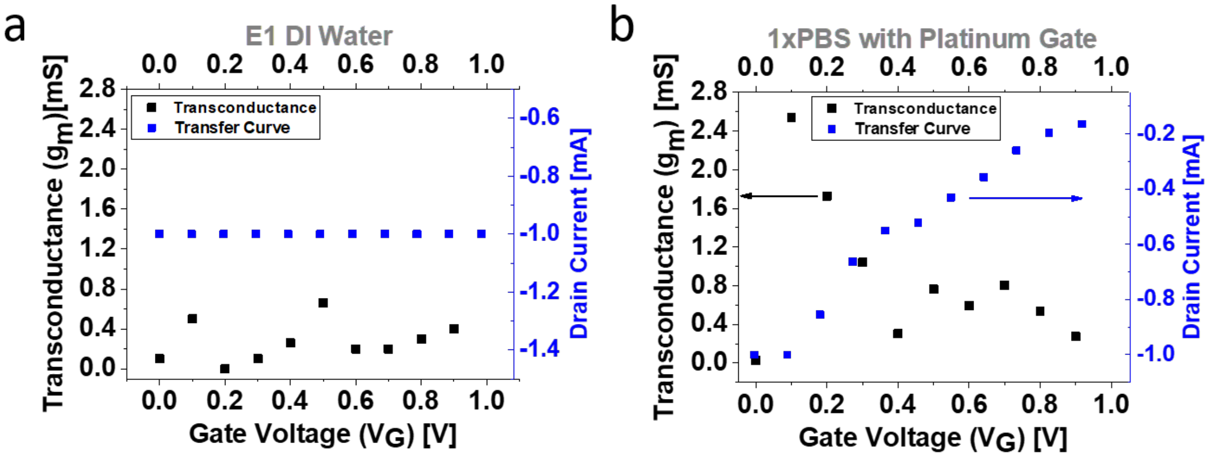

Figure 4.3 Transconductance and transfer curves for (a) DI water tested on E1 (b) For a device tested with 1xPBS and a platinum gate.

Figure 4.3 shows the transconductance and the transfer curve for a device tested with DI water (Figure 4.3(a)), and a device tested with 1x Phosphate-buffered saline (1xPBS) (Figure 4.3 (b). The transconductance curve is the ratio between the drain current and the drain voltage ($g_m = \Delta I_D/\Delta V_D$). The transconductance directly indicates the peak sensitivity of the device. From the black curve in Figure 4.3 (b), the peak occurs at a gate voltage of 0.1 V. The transfer curve, shown in blue, indicates the drain current level of the device. Figure 4.3 (b) indicates that as the gate voltage increases, the drain current is decreasing, which is the expected behaviour of an OECT. The transfer curve also shows the low current levels of these devices, operating in 1 mA range.

4.4. THC Results and Discussion

A family of curves is the best way to gain insight into the operating of an OECT. In Figure 4.3 (a)-(b), separate OECT devices were tested by grounding the source and sweeping the input of the Drain Voltage (V_D) from -0.2 V to 0.8 V in steps of 0.02 V, then in reverse from 0.8 V to -0.2 V, after V_D is swept, the Gate Voltage (V_G) is stepped up by 0.1 V. V_D is swept again at the new V_G.

This is repeated for a V_G of 0 V to 1 V in steps of 0.1 V. The generated curve can be used to determine the best operating range for the sensors. To use these OECTs as THC sensors they must be biased at a constant V_G and V_D. From the family of curves, it is important to select a voltage point where there is enough distinction between different concentrations, with enough current, but still in the linear region of operation, before the saturation region. In this case, an appropriate V_D is selected between -0.1V and -0.2 V. The V_G can be selected such that the device is not fully off, and that there is a maximum distinction for different concentrations of THC. Also, the V_G should be below the redox potential of platinum (1.188 V). When the device is biased as such. First the current must settle, before adding the THC solution. This is to ensure that the device is settled and will have a proper response. The settling time was tested by holding the drain current at -0.1 V and the gate current at 1 V. DI water was added to an unused OECT and 0.5 nM THC to another unused OECT. The results are shown in Figure 4.4. The settling time for DI water is 681 s at an averaged current level of -5571.6 µA, while the settling time for 0.5 nM is 1213 s at an averaged current level of -5639.6 µA. These settling times can vary from device to device and normally decrease over multiple runs as seen in Figure 4.5.

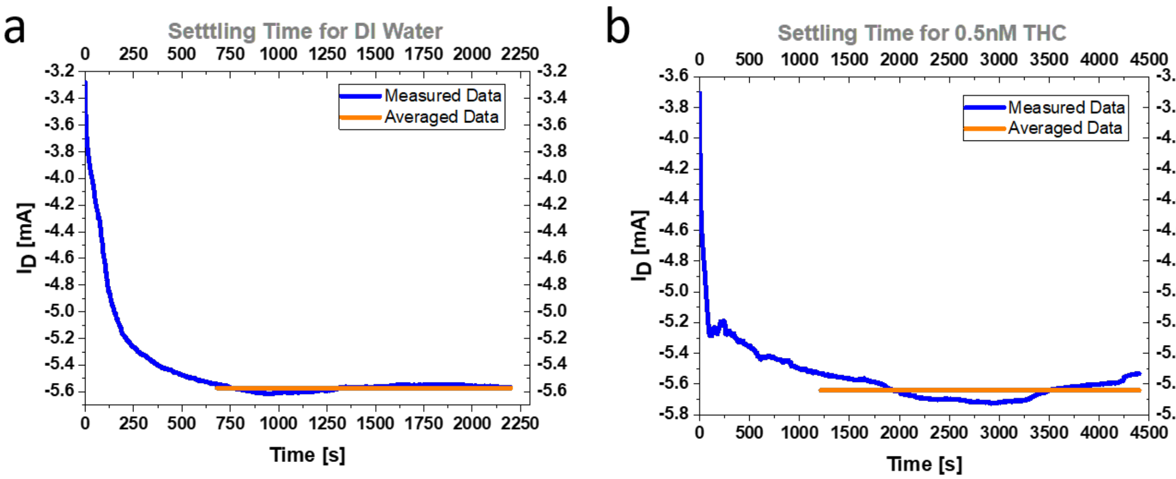

Figure 4.4 THC settling time when the drain voltage is set at -0.1 V and the gate voltage was set to 1 V (a) is the settling time for DI water on a clean OECT. (b) Is the settling time for 0.5 nM THC on a clean OECT.

The devices were tested using the THC solution bought from Sigma. The solution is 1.0 mg/mL in melatonin. Considering the molar mass is 314.46 g/mol, the concentration is 3.18x10^{-3} mol/L. This solution was further diluted to 100 µM using methanol. The solution was further diluted using DI water to 5 µM, 2.5 µM, 1 µM, 500 nM, 100 nM, 50 nM, 10 nM, 5 nM, 2.5 nM, 1 nM, 0.5 nM, and 0.1 nM.

The first four points from 0.1 nM to 5000 nM where selected to show the operation of the sensing over a broad range. 6 µL of DI water was placed on the channel of the OECT, an external platinum electrode was placed in the analyte, with care not to contact the channel, the source or the drain. A bias was applied to the drain and the gate, while the current for both was measured. After the current settled (~200 s), 6 µL of 0.1 nM THC was added thereby making the THC concentration on the channel 0.05 nM. This caused a shift in the drain current. After the drain current settled (~200 s), an additional 6 µL of THC, in a greater concentration of 10 nM was added. This was repeated for 500 nM and 5000 nM. After each addition, there was a shift in the drain current. The drain current magnitude decreases with the increasing concentration of THC. This trend is evident as the blue series in Figure 4.5.

When the OECT is initially biased, with a DI water, it takes some time (~200 – 300 s) to settle. After settling, when a concentration of THC is added to the channel, there is an initial spike in drain current. After some time, the drain current settles. The current level settling is important to consider when using OECTs as sensors. The results have to be repeatable and the current level for various concentrations has to be stable and distinguishable. To have a single current level for a THC concentration, the settling time was excluded, and the current level was averaged. This was determined by calculating the slope for every point using the three nearest points from the I_D versus time graph. The current was averaged for every concentration level, from the point where the slope is consistently below 2 μA/s until the addition of the next concentration level. This gave a stable current level that is directly derived from the instantaneous current levels. This is displayed as the green series in Figure 4.5.

These preliminary results show that the device can detect concentrations down to at least 0.05 nM and up to 5000 nM. This means that the limit of detection (LOD) is well within the range of THC found in saliva, making these sensors ideal for the application of THC sensing in saliva.

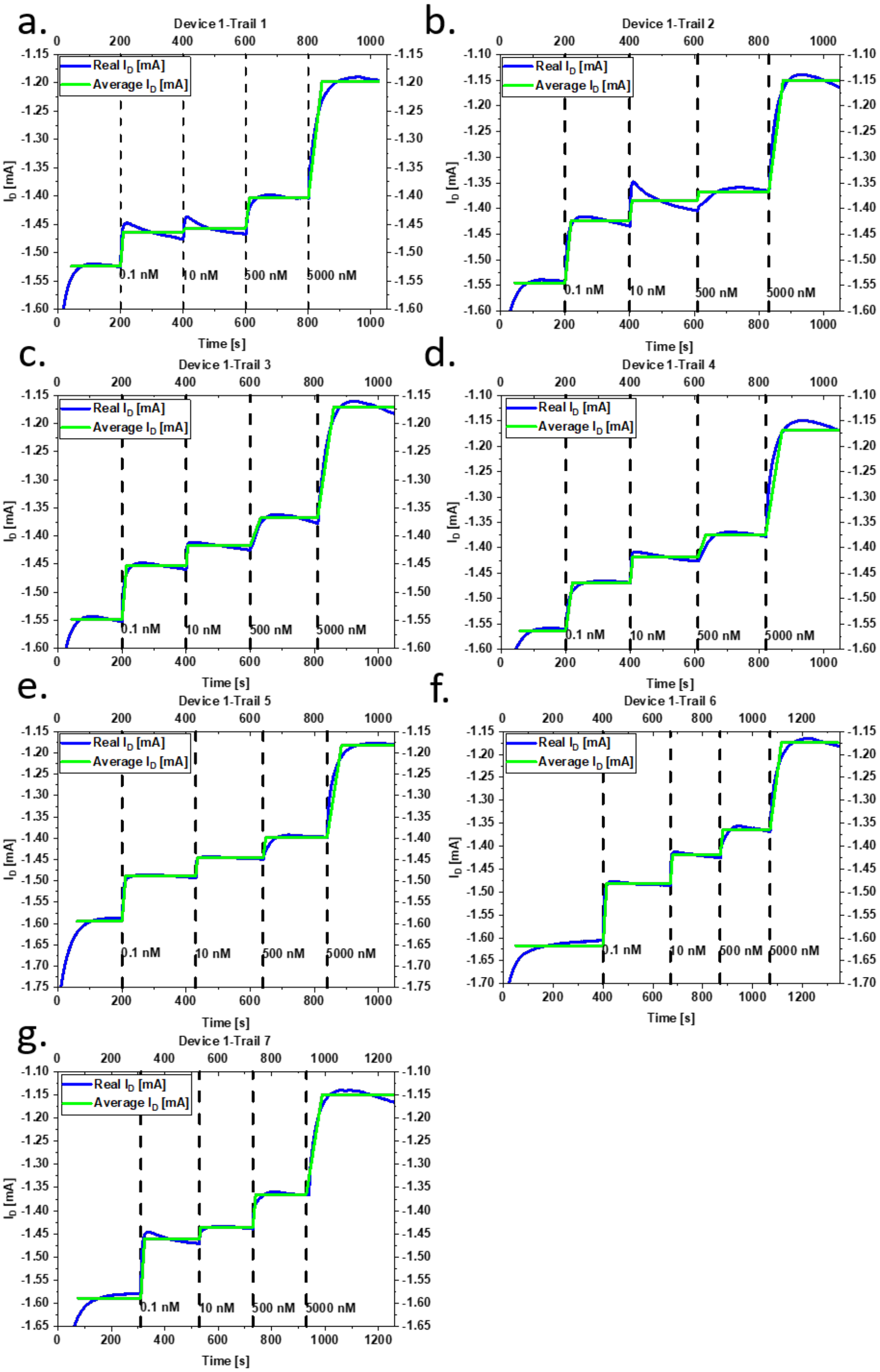

Figure 4.5 A constant voltage graph with changing THC concentration. The drain voltage is set at -0.1 V and the gate voltage was set to 1 V. (a) shows the first trial the subsequent trials are shown in figures (b) through (g). The real-time drain current is indicated in blue while the averaged drain current, which excludes the settling time is shown in green.

To compare trials and compare different devices, it is necessary to normalize the current. The current was normalized with the DI current level. The averaged current levels are divided by the DI current level according to Equation 4.3.

$$I_{\mathrm{Normalized}} = \frac{I_{\mathrm{THC}}}{I_{\mathrm{DI}}} \qquad 4.3$$

This allows for comparison. The normalized current can be averaged across all trials and devices. These results are shown in Figure 4.6. Two different devices were tested with the same THC concentrations of 0.1, 10, 1000 and 5000 nM. The current levels for each device were normalized by dividing it by the DI water current level, according to Equation 4.3. The two different devices have a very low error, with the blue series having and error below 0.87% and below 2.65% for the black series. In addition, the slope of both devices is very similar showing the repeatability of these sensors For the black series each section has a slope of -0.0134 /dec for 0.1 to 500 nM and -0.1276 /dec for 500 to 5000 nM, while the blue series has a slope of -0.0153 /dec for 0.1 to 500 nM and -0.1300 /dec for 500 to 5000 nM.

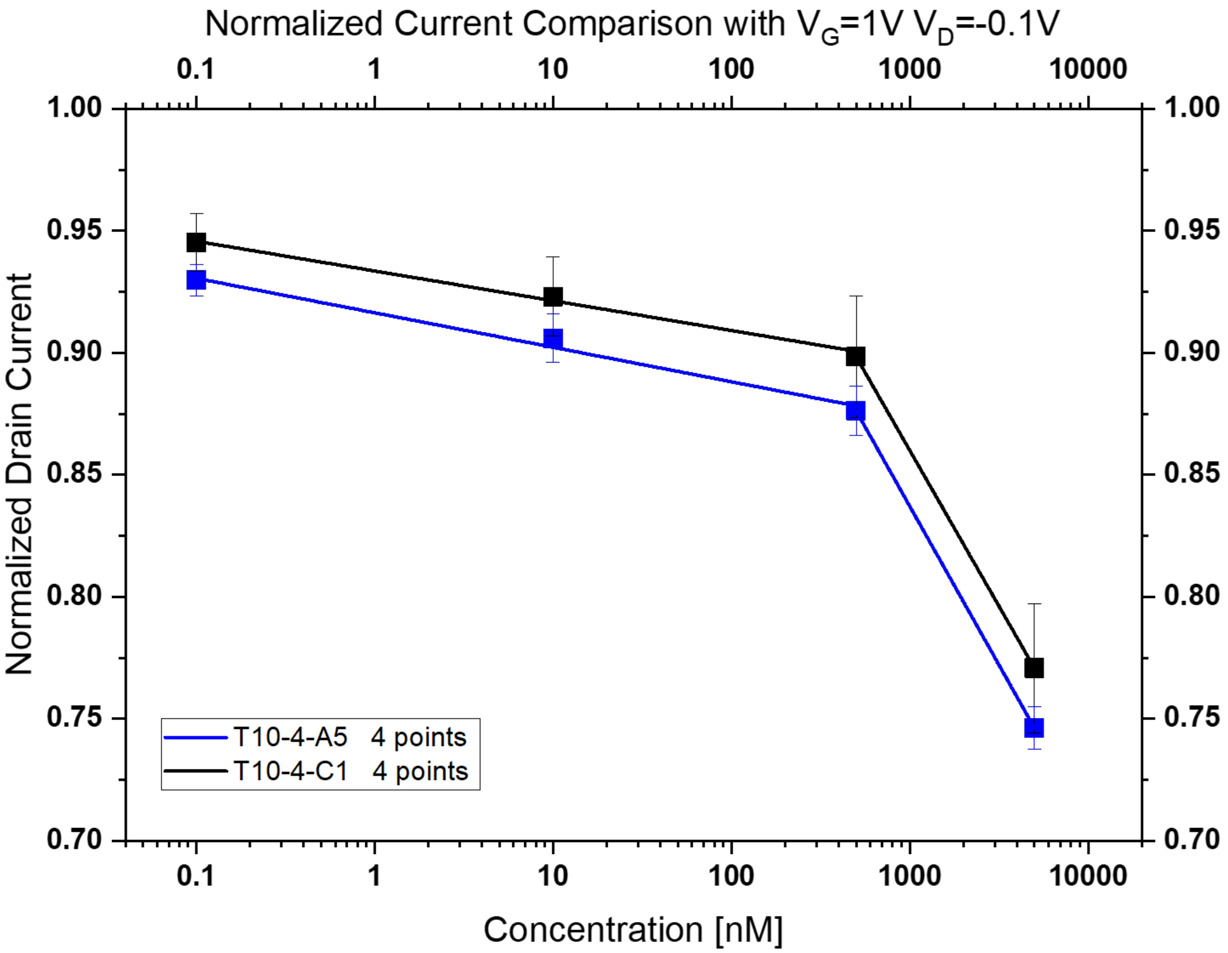

Figure 4.6 Normalized THC current levels for two different devices. These devices have a low error with the blue series having and error below 0.87% and below 2.65% for the black series. The slope for the black series is -0.0134 /dec for 0.1 to 500 nM and -0.1276 /dec for 500 to 5000 nM, while the blue series has a slope of -0.0153 /dec for 0.1 to 500 nM and -0.1300 /dec for 500 to 5000 nM.

To reinforce, the sensor's abilities, the number of points between the lowest and the highest concentrations were increased from four to twelve to increase the fidelity. However, due to the method in which the sensors are tested only four points were tested at a time. This is because the amounts of liquid that are on the channel quickly become too great and the solution becomes mostly DI water instead of the desired THC concentration. By breaking up the twelve points into five sets the entire range can be tested with higher fidelity. Each set started with DI water. The last step of the set was repeated as the first step of the next set. The range was broken up as follows. DI water, 0.1 nM, 0.5 nM, 1 nM and 2.5 nM. Then DI Water, 2.5 nM, 5 nM, 10 nM and 50 nM. Then DI water, 50 nM. 100 nM, 500 nM and 1000 nM. Finally, DI water, 1000 nM, 2500 nM and 5000 nM.

Though there is an overlapping point between sets, there is a difference in the normalized current level. This is due to the difference in the DI water volume. There is 2.5 times as much DI water present in the last point of the previous set and the first point of the next set. Therefore, there was a shift in the normalized current level. To take this into account the overlapping normalized current level for the overlapping point was set at the same point. All the normalized current levels from that set are shifted by the same amount. This resulted in Figure 4.7. These results have an error of less than 1.41%. The slope is similar to those presented in Figure 4.6, with -0.04188 /dec from 0.1 to 500 nM and -0.1730 /dec for 500 to 5000 nM. This increase in slope can easily be explained by the fact the same number of points were tested in a smaller concentration range.

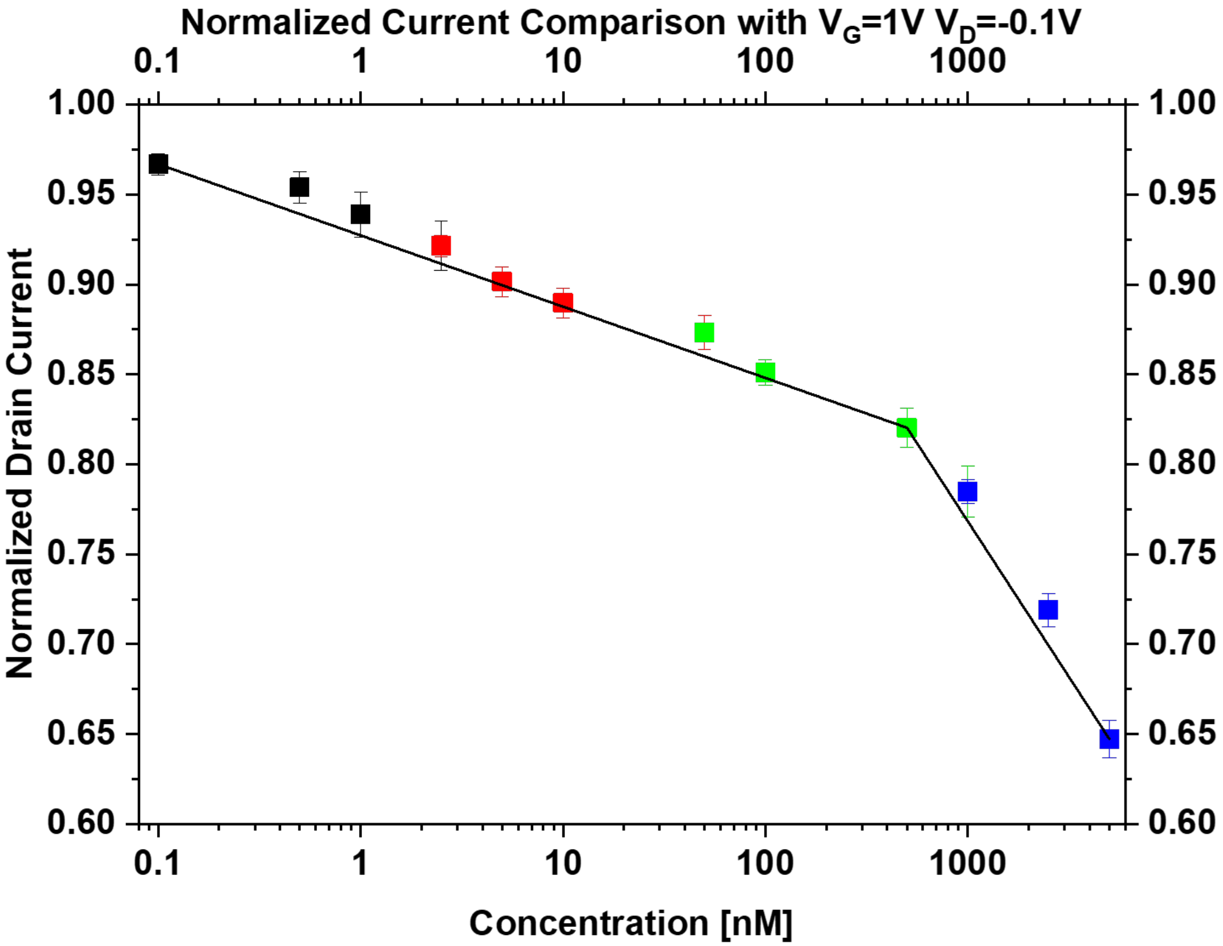

Figure 4.7 The normalized THC current level. Four series are presented, represented by different colours. Each of these series started with a DI water level before THC was added, this DI water current level was used to normalize the results. The overlapping THC concentration point between series was set to the same point, and the entire series was shifted by the same amount. This device has an error of less than 1.41%, the slope is for -0.04188 /dec from 0.1 to 500 nM and -0.1730 /dec for 500 to 5000 nM.

4.5. Melatonin Detection Theory

Melatonin detection also uses redox potential in the same way as THC however, in this case, because the redox reaction of melatonin is non-reversible and has an anodic peak at 0.6-0.7 V[159] this means that the melatonin oxidizes in this range. There is no cathodic peak, meaning that this reaction is not reversible, and the melatonin is used up when it is sensed. It is important to use an appropriate gate electrode. The redox potential of silver/silver chloride (Ag/AgCl) is 0.22233 V [160] the redox potential of gold (Au) is 1.83 V [161] and for platinum (Pt) it is 1.188 V [143]. Therefore, because gold is more cost-prohibitive than platinum and the redox potential of Ag/AgCl is below that of melatonin, platinum is ideal as a gate electrode. The redox potential of the melatonin is reached between 0.6-0.7V meaning that the platinum gate electrode must be biased above 0.7V and below the redox potential of platinum (1.188 V). The melatonin will oxidize when the gate is biased at this level, many reactions occur, however, one possible reaction is that the double-bonded oxygen will become a single bond, as an electron is lost[162].

The melatonin structure is illustrated in Figure 4.8. The electron is extracted by the gate electrode, however, by having a single bonded oxygen, the oxygen becomes slightly negative which extracts any native cations from the channel, thereby increasing the current magnitude (more negative). In other words, there are two competing phenomena. Equation 4.2 holds, and can be written as Equation 4.4 below, meaning that as the concentration of Melatonin increases, the concentration of the oxidized Melatonin will increase, this, in turn, increases the effective gate voltage, which should, in turn, decreases the drain current magnitude in the OECT, as it is a depletion mode device. However, as more melatonin is oxidized, more shielding occurs because of the now single-bonded oxygen because slightly negative, shielding the channel from the gate voltage, and doping the channel by removing cations from the channel. In the end, the shielding effect has a greater impact on the drain current than the removal of the electrons by the gate. In other words, as the concentration of melatonin increases the drain current increases in magnitude (becomes more negative). However, because melatonin does not have a reversible redox reaction, the sensors can only be used once. However, if the two devices have the same current levels without a melatonin solution, then this pattern is the same. This leads to Equation 4.4.

$$V_G^{eff} = V_G + (1+\gamma)\frac{k_{Bz}T}{e}\ln([Melatonin(Ox)]) \quad 4.4$$

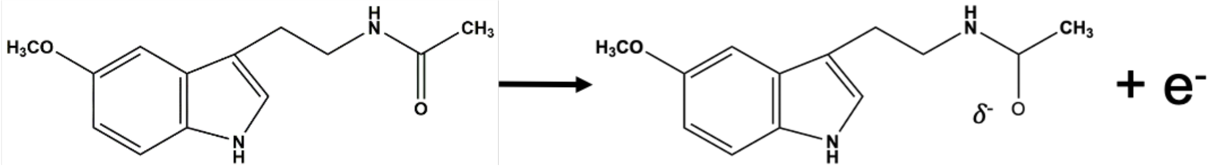

Figure 4.8 Structure of Melatonin. The double bond of the oxygen is broken, causing the loss of an electron and therefore the oxidation of the melatonin between 0.6-0.7 V. This is not reversible.

From the family of curves, a drain voltage and a gate voltage can be selected. Selecting the proper drain voltage should be selected such that there is enough distinction between different concentrations low enough such that the current is limited to a reasonable level. The gate voltage can be selected to be at a maximum that is below the redox potential of the platinum gate (1.188 V). Therefore, the gate voltage was set at 1 V and the drain voltage was set between -0.1 V to -0.2 V. When the device is constantly biased, the device needs to settle, meaning that the current becomes a relatively flat constant. When Melatonin is added, the drain current increases in magnitude.

4.6. Melatonin Results and Discussion

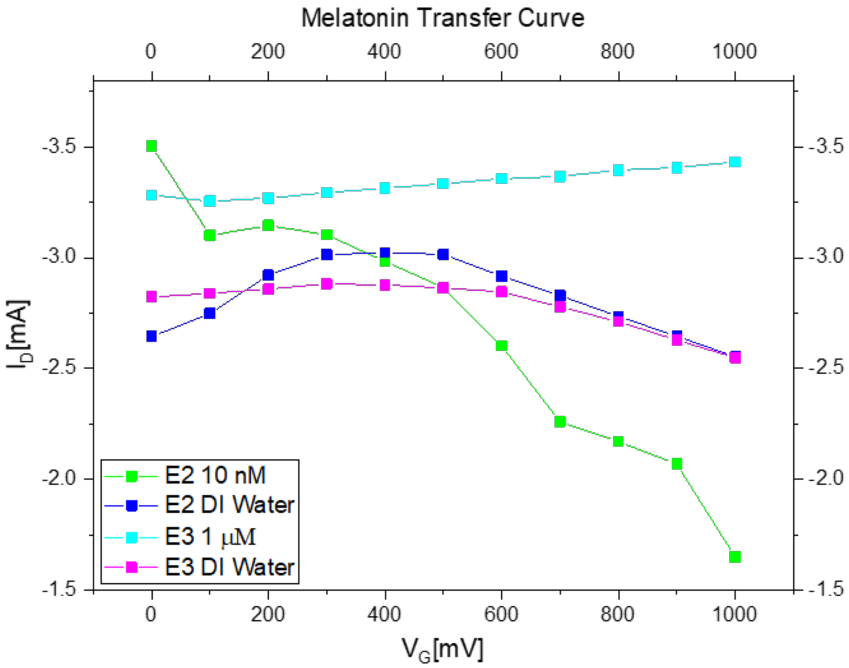

Figure 4.9 Graph of melatonin tests, showing the drain current, versus the gate voltage. These devices were tested with DI water, as shown in the blue and magenta curves. They were also tested with 10 nM of melatonin, shown in green. The device was also tested with 1 µM of melatonin shown in teal.

When these devices are first tested with DI water, a base current level can be measured. After that, the Melatonin solution can be placed on the channel of the device and tested. This results in a drain current level for that particular melatonin concentration. It is important to compare the results at a gate voltage that is greater than the redox potential. Considering the results for a gate voltage greater than 700 mV, as shown in Figure 4.9, there is a large magnitude drain current for 1 µM Melatonin with respect to the DI current level and a smaller magnitude drain current for 10 nM Melatonin with respect to the DI current level. Meaning that the 1 µM drain current is higher than that of the 10 nM drain current. These results are consistent with the expected results because, at lower concentrations (10 nM) the effective gate voltage increases, thereby lowering the drain current, from the DI value. However, as the concentration of melatonin increases (1 µM), shielding becomes more dominant, blocking the gate voltage thereby leading to an increase in the drain current.

These devices can only be used to test the concentration of Melatonin a single time because the Melatonin reaction is irreversible. This can be seen in Figure 4.10, where the drain current level changes with subsequent measurements, thereby degrading the signal.

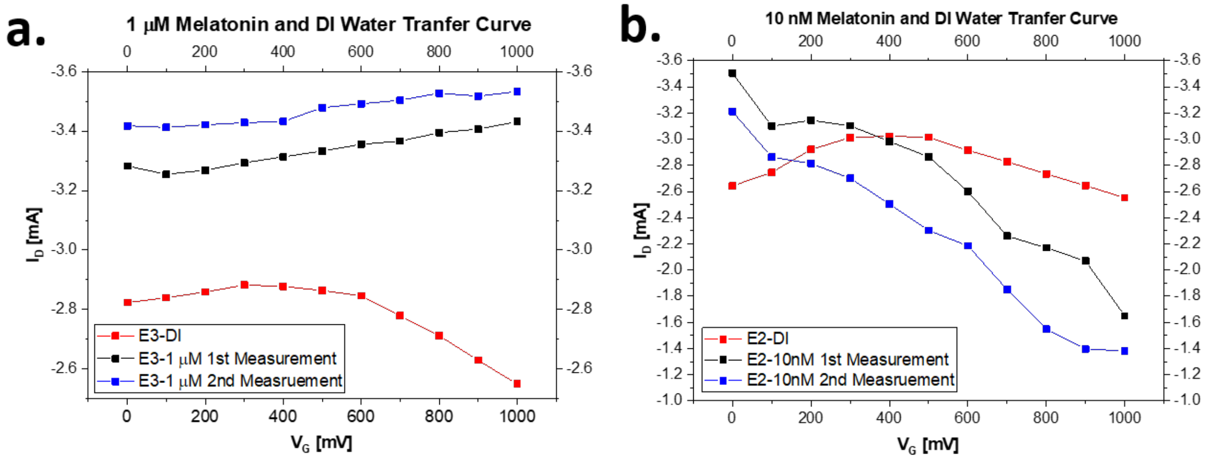

Figure 4.10 Transfer curves for melatonin sensors showing multiple tests on the same devices. (a) Shows transfer curves comparing DI water (red) and 10 nM melatonin. There is a decrease in the current level between the first run (black) and the second run (blue) of the device. Therefore, these sensors should be used a single time because the redox reaction of melatonin is irreversible. (b) Shows transfer curves comparing DI water (red) and 1 µM melatonin. There is also a decrease in the current level between the first run (black) and the second run (blue) of the device, further illustrating the single-use nature of these sensors.

4.7. Conclusion

Cannabis was legalized in Canada in 2018, and with it, the enforcement of impaired driving offences has been difficult. The psychoactive component of cannabis, THC, is responsible for impairment. However, the THC levels in blood and urine do not indicate impairment as they remain at elevated levels, much longer than impairment lasts. Concentrations of THC in saliva are more closely associated with impairment for roadside testing. A large number of approaches to detect THC in saliva require mass spectroscopy or chromatography, which require bulky and expensive equipment. Other techniques include immunoassays, which require labelling which can be expensive and requires difficult processes. Other electrochemical detection methods can require large external equipment or more complex measurements such as CV curves or impedimetric measurements. By using OECTs to detect THC in saliva these drawbacks are avoided. This approach allows for quick, economical and customizable manufacturing using the 3D printing method. Also, the use of OECTs means that the devices are small, biocompatible, and do not require large external equipment as the output signal of the OECT is a current signal making them convenient and easy to implement and use. This makes OECT detection of THC perfectly suited for saliva-based roadside testing, that could be used by law enforcement.

That is why ‘wet’ THC sensors were created. These OECT based sensors can detect THC concentrations down to 0.05 nM, which is well below the range found in saliva, which is 3.18 nM-1039.88 nM with a median of 89.36 nM [163]. These sensors work with THC diluted in DI water, for these sensors to work in saliva they must be functionalized to exclusively detect THC, in an environment full of different entities. Though these sensors are not functionalized. Their operation with DI water-diluted THC is the first step in developing full THC saliva sensors. The next step in making these sensors is to functionalize the gate or the channel to add specificity.

Melatonin is a crucial sleep hormone, making it a useful bio parameter to be measured and characterized. By using 3D printed OECTs, melatonin can be effectively measured and then the sensor disposed of. These melatonin results are preliminary and more extensive testing needs to be done to determine the limits of these OECTs to sense melatonin. However, based on these preliminary tests it is clear that these devices can be used for detection of small concentrations of melatonin as low as 10 nM and as high as 1 μM. This will be benefitted by functionalization of the device for more targeted detection.

5. Fully 3D printed OECT Based Logic Gates for Multiplexing

5.1. Introduction

As discussed in the background chapter, the logic gates described in this chapter were made using aerosol jet 3D printed OECTs with a PEDOT:PSS channel. Instead of using a single OECT to sense, these devices combine multiple OECTs to build basic logic gates including NOT, NAND and NOR gates. The working principle of OECTs and PEDOT:PSS are described in detail in the background chapter. In short, the OECT acts like a 'wet' transistor with a source, gate and drain contact. This means that they turn on and off under specific conditions and therefore can be used to create logic gates in the same way as traditional transistors. As discussed in the background chapter, the OECTs used in this thesis use PEDOT:PSS as the channel material and are therefore p-type depletion mode (normally on) transistors. The OECTs use PEDOT:PSS channel coupled with, silver electrodes, and PDMS masks, all of which were 3D printed with an aerosol jet 3D printer onto a flexible PET substrate.

Biosensors have three elements, a bio-receptor, bio-transducer and signal processing, as discussed in the background chapter. By using logic gates, all three elements of a biosensor can be combined without the use of external circuitry. PEDOT:PSS is electrochemically active, meaning that it has native bio-detection properties, OECTs act as the bio-transducer, and finally, by arranging the OECTs into logic gates, signal processing can take place. These logic gates can be combined to make multiplexing circuits that allow for multiple inputs and a single output. This means that multiple different bio-entities can be sensed simultaneously. These inputs could be functionalized to add specificity.

Most work with OECTs has been done with sensors and very few have used OECTs to show logic gates[64–66]. This work focuses on using OECTs to make logic gates and ultimately using those logic gates to make multiplexers (MUX). This work presents NOT, NAND and NOR gates and then combines them to make a two-channel MUX. Having a MUX from OECTs means that each of the inputs of the MUX can be different biosensors, and then have the output signal be processed with the MUX. These MUX are 3D printable, meaning that the cost of fabrication is lowered, with a lower commercialization fabrication price, as well as flexible, making them perfectly suited for bio-wearables. The basic logic gates presented in this chapter can be used to build more complex logic circuits, allowing for more complex signal processing to be done.

5.2. Fabrication and Materials

All the logic gates were completely 3D printed using an Optomec Aerosol Jet® 5x System as outlined in the background chapter. The logic gates are made with simple four layers. The first layer is a polyethylene terephthalate (PET) substrate. Specifically, MELINEX® 454 provided by DuPont Teijin Films (36 µm) and is pretreated with an adhesion promoter. The electrodes were printed with the Optomec ultrasonic atomizer using silver ink, specifically Clariant PRELECT® TPS 50 composed of silver nanoparticles. The electrodes were 100 µm wide a ~2.45 µm thick, as two layers were printed larger landing pad of 400 X 400 µm were printed. The ink was baked at 140ºC overnight to sinter the ink.

The second layer was the channel material, which was PEDOT:PSS. First ink had to be prepared. The main component of the ink, PEDOT:PSS, specifically Heraeus Clevios^{TM} PH 1000 at 79 v/v% was added. Next ethylene glycol (≥99%) from Sigma was added by 20v/v% as a conductivity promoter[153,154]. Then, dodecylbenzenesulfonic acid solution (70 wt. % in isopropanol) (DBSA) from Sigma was added by 0.1v/v % to change the surface tension and minimize contact resistance[155]. (3-Glycidyloxypropyl) trimethoxysilane (GOPS) (≥98%) from Sigma was added by 0.9v/v% to act as a crosslinker. These were mixed in a nitrogen environment to create the PEDOT:PSS ink, which was then printed as the channel. Two layers were printed making it ~600 nm thick. The channels measured 250 µm X 1250 µm, giving a W/L ratio of 5. The ink was baked at 130°C for 15 minutes to crosslink the polymer.

Finally, the mask was printed using a 1:1 v/v% PDMS: crosslinker solution using KER-4690-A: KER-4690-B from Shin-Etsu Chemical Co., Ltd. This PDMS: crosslinker mixture was then diluted with 3:1 Hexane and then printed using the pneumatic atomizer on the Optomec printer. The PDMS ink was kept at 30°C and constantly stirred during printing. The ink was exposed to 405 nm UV light during printing to initialize the crosslinking of the PDMS and then baked at 130°C for 30 minutes to complete the crosslinking. The PDMS ultimately was ~3.5-4 µm thick. The fabrication steps of these devices are illustrated in Figure 2.9.

5.3. Measurements and Characterization

All the electrical characterizations were done using a customized measurement station using a Keithley 2612B, a Tektronix MDO3102 oscilloscope and a BK Precision 9130B wave generator, which was controlled by a costume LabVIEW program.

Each device was tested using the electrolyte solution of NaCl, prepared by dissolving salt in de-ionized (DI) water. For each gate, one (Source Measurement Unit) SMU of the Keithley 2612B was used to measure the output of the device, while the other SMU was used to sweep the input of the device, generally from -0.5 V to 1.2 V in steps of 0.05 V. The ground of the logic gate was connected to the SMU ground, which is common. The -V_{DD}, for the devices, was provided by a BK Precision 9130B or a Tektronix MDO3102 oscilloscope. This supplied a constant bias for the device, in this case -1V. The BK Precision 9130B in the case of the NOR and NAND gates, also provided the constant supply for $V_{in, A}$, either LO (1 V) or HI (0 V). The connections for the NOT, NAND and NOR gate can be seen in the Schematics in Figure 5.1(a), Figure 5.3(a) and Figure 5.5(a), respectively. To measure the performance of the devices, a NaCl electrolyte of varying concentrations was placed on the channel and the gate electrode of each OECT and the output was measured. The input voltage (V_{in}) was then plotted versus the output voltage (V_{out}).

When the electrolyte was changed, the channel was rinsed with DI water, then dried with compressed air before placing the new electrolyte solution.

5.4. Device Design, Operation and Results

5.4.1. Device Design and Operation

An inverter (NOT), a NAND and a NOR gate were designed using only p-type depletion mode (normally on) OECTs. These OECTs use PEDOT:PSS for the channel material, meaning that they operate with electrolytes, specifically the cations in the electrolyte. In this case, NaCl was used as the electrolyte. Ideally, complementary transistors[64] would be used to create logic gates, meaning both n and p-type, however, n-type semiconductors are rare, and electrochemical n-type organic semiconductors are even rarer as discussed in the background chapter. Therefore, simply one kind of OECT was used to fabricate all the logic gates, which has the added benefit of simplifying the fabrication process.

By using depletion-mode transistors this means that the gate-source voltage must be greater than zero ($V_{GS}>0$) for cations to be driven into the channel, de-doping the channel, lowering its conductivity and turning off the OECT. This means that an input level logic of HI has been assigned to $-V_{DD}$ and LO to ground.

5.4.2. NOT Gate

5.4.2.1. Not Gate Materials and Methods

The NOT gate is the simplest of the three gates and was demonstrated by our group in an earlier publication [1] and discussed in the following chapter. Though these logic gates use a different fabrication method, they use the same concept and design. The design is shown in Figure 5.1(a), uses two OECTs. The top OECT (Q1) has the gate shorted to the bias of $-V_{DD}$, this ensures that Q1 is always on, meaning that $-V_{DD}$ is always is set the output. The second OECT (Q2) has the input at the gate, meaning that when the input is set to HI (0 V) Q2 is conducting and the output is pulled to ground (GND). However, when the input is set to LO (1 V), Q2 turns off, thereby leaving the output to be $-V_{DD}$. This means that when the input is LO, the output is HI and vice-versa. The operation table is shown in Figure 5.1(b).

NOT gates are the simplest logic gate that simply has an output that is the inverse of the input, as shown in Figure 5.1(b). A NOT gate is a simple use of two OECTs, where the source of one is connected to the drain of the other. The first has the gate and the source shorted together and biased at a $-V_{DD}$. The drain of the second is grounded. The input is the gate of the second, grounded transistor, and the output is taken from the connection of the drain and source of the two transistors. This is illustrated in Figure 5.1(a).

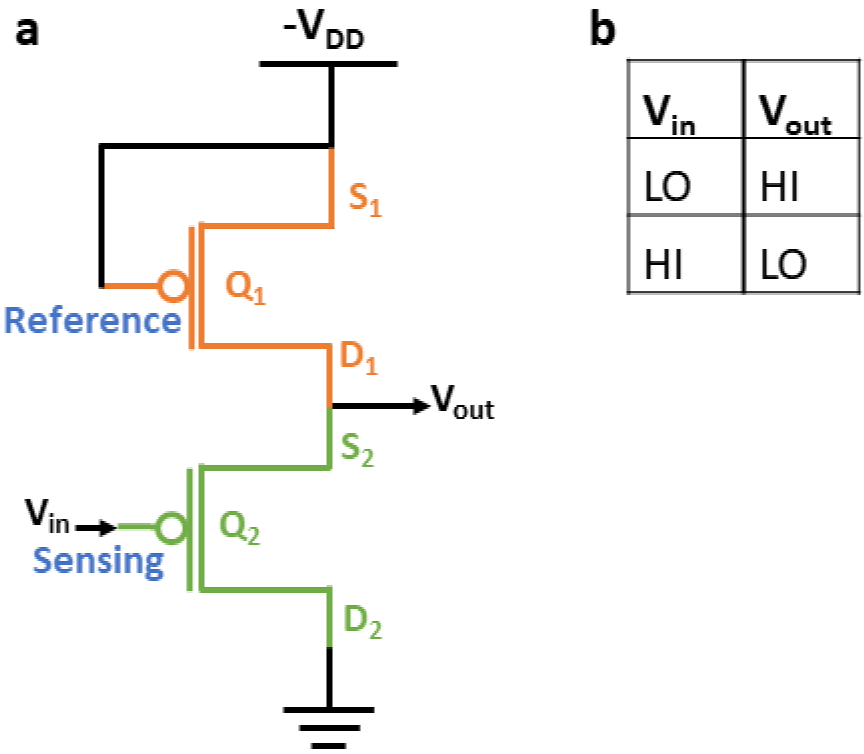

V_{in}	V_{out}
LO	HI
HI	LO

Figure 5.1 (a) Schematic of a NOT gate. The top OECT is indicated in orange and the second OECT is indicated in green. The top transistor (Q1) is left as the reference electrolyte and the bottom transistor (Q2) is the sensing transistor. (b) Logic table for a NOT gate.

The top transistor (Q1) is kept at a reference concentration and the second transistor (Q2) is set as the sensing transistor. NOT gates switch and input logic HI to an output logic LO, and an input logic LO to an output logic HI. The required input voltage required to shift the output from LO to HI shifts with concentration. The higher the concentration the lower the required input voltage to switch the output from LO to HI. This is because Q1 is always ON as the gate is tied to the source. This means that the channel of Q1 conducts $-V_{DD}$ to V_{out}. When no V_{in} is applied, then Q2 is also on and V_{out} is pulled to ground, when V_{in} is applied cations are driven into the channel to de-dope the channel of Q2, turning off Q2, which means that V_{out} is no longer shorted to ground (logic LO) and since Q1 is always ON, $-V_{DD}$ is sent to V_{out}, which is logic HI. NOT gates are can invert the signal but can also be used as sensors, are their response to the concentration of electrolyte changes the response of the gate. The higher the concentration of the electrolyte, the less voltage from V_{in} that is required to turn Q2 OFF.

These sensors not only act as a way to detect concentration levels but also the difference in different types of cations. Due to the ionic mobility in water, the required switching voltage also shifts. The lower the ionic mobility, the lower the switching voltage required to change the output from LO to HI. This is discussed in depth in the next chapter.

5.4.2.2. NOT Gate Results and Discussion

The NOT gate is tested by switching the input from HI to LO and then measuring the output. The input is swept from around -0.2 V to 1 V in steps of 0.02 V. As shown in Figure 5.2 when the input is HI (right on the x-axis), the output is LO (bottom of the y-axis), then when the input is LO (left on the x-axis) the output is HI (top of the y-axis). This confirms the expected results in Figure 5.1(b). The NOT results show that there is a shift in the required input voltage to switch the output from LO to HI with a shift in the concentration. As the concentration of the electrolyte increases, the required input voltage to switch the output decreases. This is because there are more cations present in the electrolyte that de-dope the channel, lowering the conductivity and turning the OECT off. Not only is there a distinction between the concentration of electrolytes (Figure 5.2(a)-(c)), there is also a distinction between different cations. These results further reinforce the results discussed in Chapter 6.

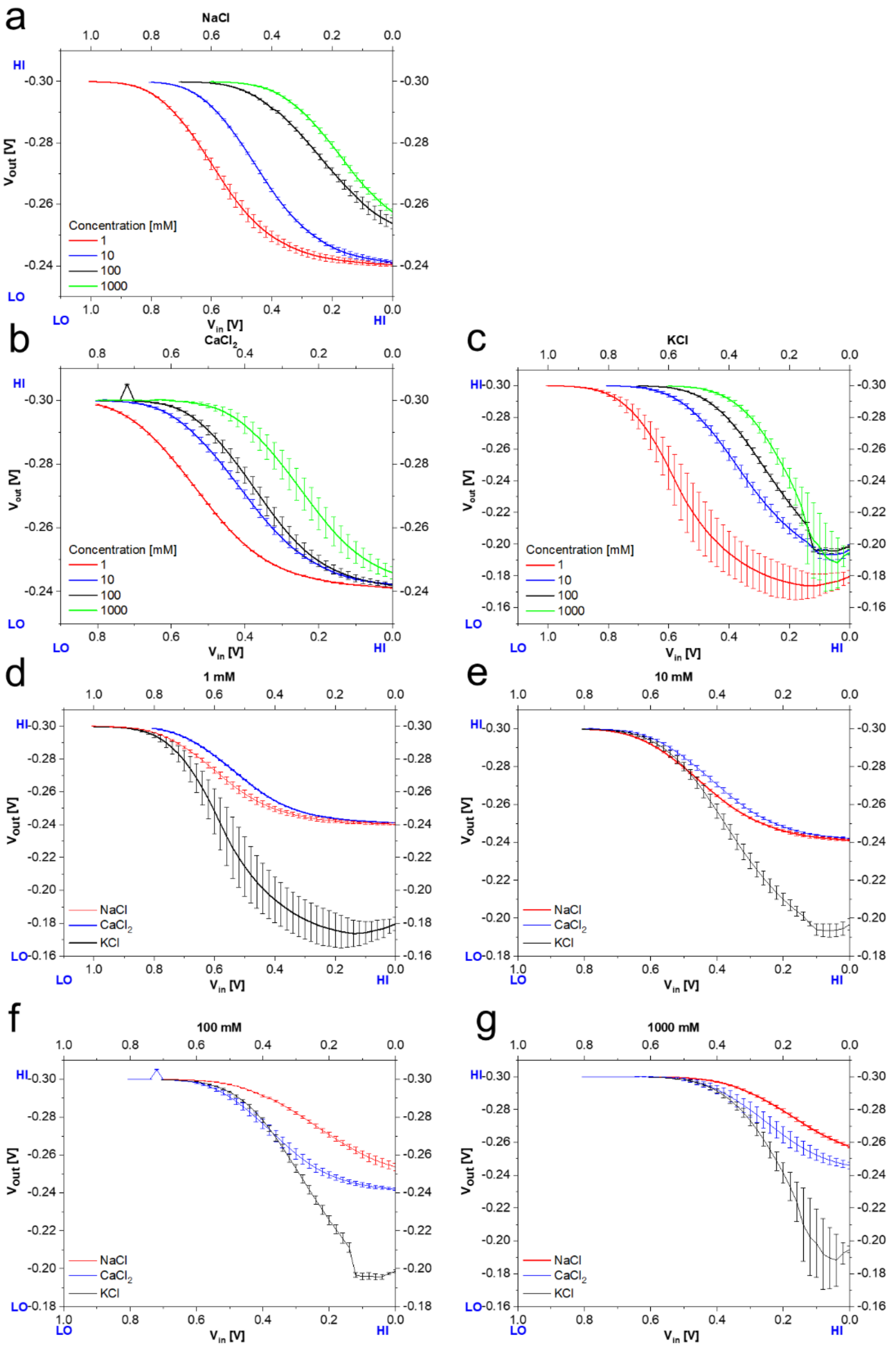

Figure 5.2 NOT gate results printed with the Optomec printer. (a) Displays the NOT gate tested with NaCl at 1, 10, 100 and 1000 mM. (b) Displays the NOT gate tested with $CaCl_2$ at 1, 10, 100 and 1000 mM. (c) Displays the NOT gate tested with KCl at 1, 10, 100 and 1000 mM. The results are compared with the results for NaCl, $CaCl_2$ and KCl at (d) 1 mM, (e) 10 mM, (f) 100 mM, (g) 1000 mM.

5.4.3. NAND Gate

5.4.3.1. NAND Materials and Methods

The NAND gate (Figure 5.3(a)) operates similarly to the NOT gate but uses three OECTs and has two inputs. In this case, the first OECT (Q1) has its gate tied to $-V_{DD}$, meaning that Q1 is always on, and conducting $-V_{DD}$ to the output. The other two OECTs (Q2 and Q3 respectively) have two separate inputs set to their respective gates. This means that when V_{in} is set to HI (0V) the OECT is on and conducting when the input is set to LO (1V) the OECT is off and not conducting. This means for the output to be brought to GND, both Q2 and Q3 have to be conducted, meaning $V_{in, A}$ and $V_{in, B}$ have to be set to HI for them both to conduct and pull the output to GND (LO). Otherwise, the output will be $-V_{DD}$ (HI). The NAND gate operation should be such that the output is LO when both inputs are HI, and a HI output for all other inputs. This behaviour is summarized in the table in Figure 5.3(b).

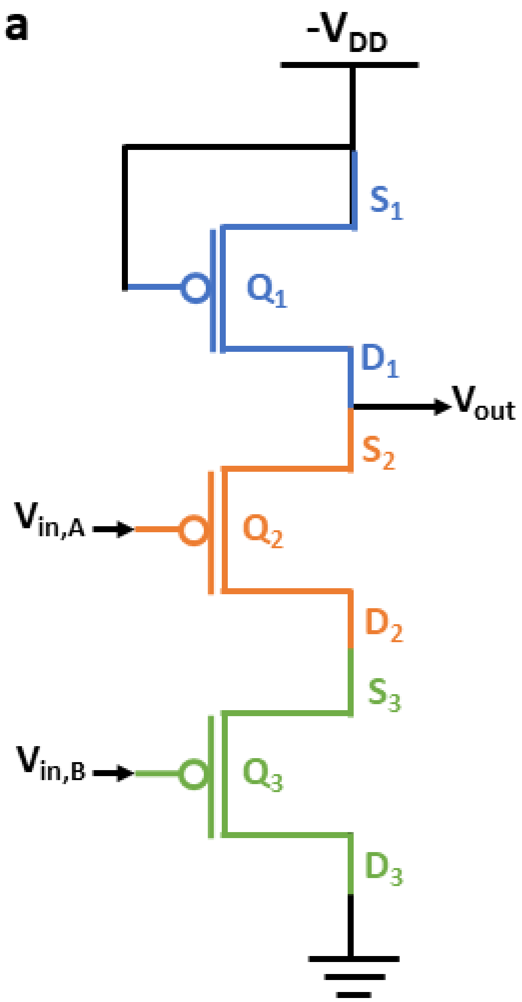

b

$V_{in,A}$	$V_{in,B}$	V_{out}
LO	LO	HI
LO	HI	HI
HI	LO	HI
HI	HI	LO

Figure 5.3 (a) NAND gate schematic. Q1, shown in blue, is always conducting -V_{DD} *to* V_{out}*. Therefore, for* V_{out} *to be LO, it must be grounded, by having both Q2 and Q3, shown in orange and green respectively, to be ON. This requires, both* $V_{in,\,A}$ *and* $V_{in,\,B}$ *to be logic HI, otherwise, Vout will be -*V_{DD} *which is logic HI. (b) NAND logic table.*

5.4.3.2. NAND Results and Discussion

To properly test the NAND gate, the first input must be held HI while the second input is swept from HI to LO. The first input is then held LO and the second input is swept from HI to LO, the output is measured during both of these measurements are then compiled to show the overall response of the gate. The theoretical response of a NAND gate is shown in Figure 5.3(b). When both inputs ($V_{in,\,A}$ and $V_{in,\,B}$) are set to HI (1 V), the output (V_{out}) should be LO. All other combinations of $V_{in,\,A}$ and $V_{in,\,B}$ should give a HI output. The actual results are shown in Figure 5.4.

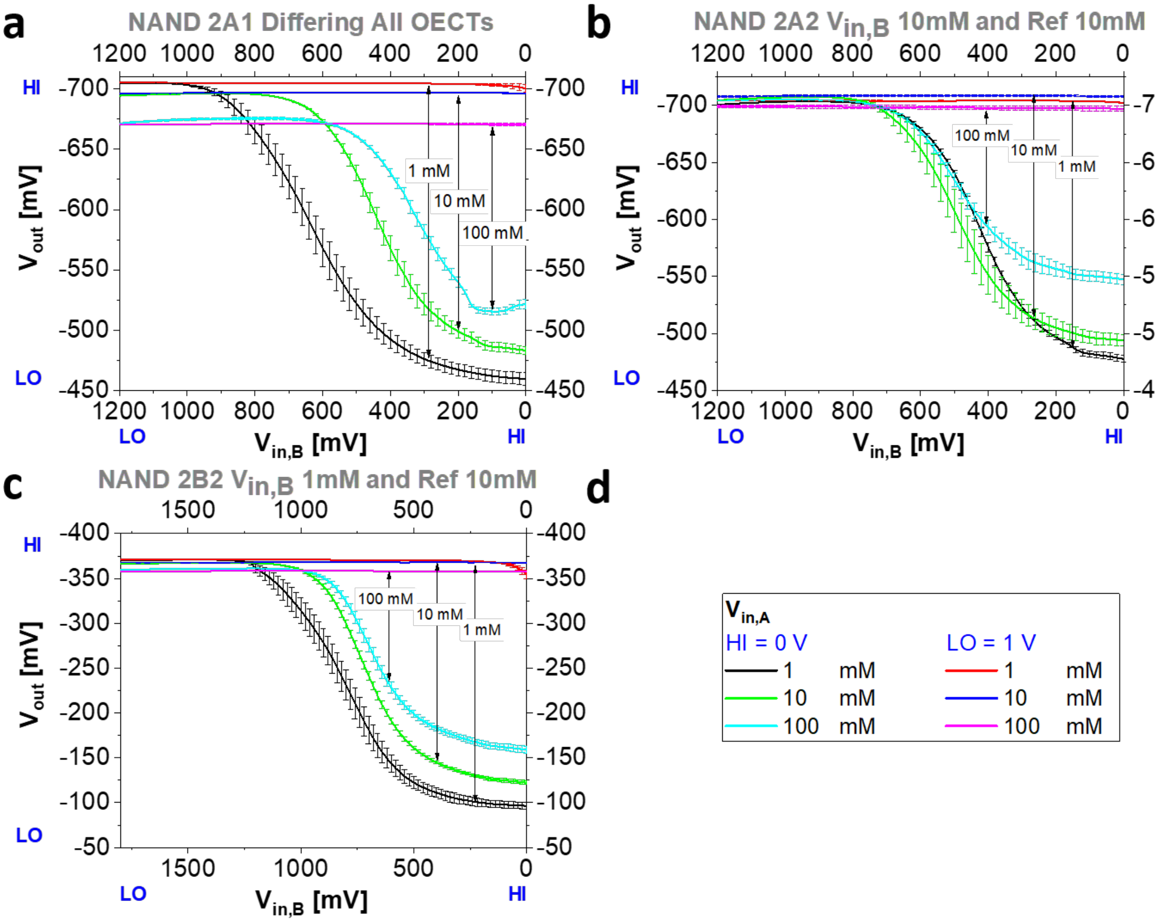

Figure 5.4 Response of a NAND gate showing testing with different electrolyte concentrations. (a) The results 1, 10 and 100 mM when all OECT electrolyte concentrations match. (b) The results for 0.1, 1, 10, 100 mM on the $V_{in,\,A}$ OECT, while $V_{in,\,B}$ and the reference OECTs are held at 10mM. (c) The results for o.1, 1, 10 and 100 mM on the $V_{in,\,A}$ OECT, while $V_{in,\,B}$ is held at 1 mM and the references OECT is held at 10 mM. The error bars are calculated using the standard error method. (d) The legend for (a), (b) and (c).

From the results (Figure 5.4 (a)-(c)), there is a clear distinction between the different concentrations of NaCl. If we consider the navy, black, green and cyan lines, which is when $V_{in,\,A}$ is set to HI, and look on the X-axis when $V_{in,\,B}$ is also HI, we can see that V_{out} is LO. All other combinations of the inputs lead to a HI V_{out}. Therefore, the expected results for a NAND gate are achieved.

In addition, there is a distinct difference in response when different concentrations of electrolytes are used on the channels. This result is consistent with the NOT gate results seen in the next chapter. This indicates that these logic gates could potentially be used as sensors because there is a shift in the switching voltage with a shift in concentration. As the concentration of the electrolyte increases, the required input to switch the output decreases. This is because there are more cations available to turn off the channel material, meaning less gate voltage is needed.

The results are shown in Figure 5.4 shows three different conditions and indicate little change in the results. Figure 5.4 (a) is the result for when all of the OECT electrolytes are varied. Figure 5.4 (b) is the result when only one input is varied ($V_{in,\,A}$), while the other input ($V_{in,\,B}$) and the reference OECT are held at 10 mM NaCl. Figure 5.4 (c) is the result when only one input is varied ($V_{in,\,A}$), while the other input ($V_{in,\,B}$) is held at 1 mM and the reference OECT is held at 10 mM NaCl. The major difference between these scenarios is that the V_{out} = HI level is more unstable and shift when all of the OECT levels are changed instead of one input, as seen in Figure 5.4 (a). The V_{out} = HI level is more stable when one input and the reference are held at a set concentration as with Figure 5.4 (b) and (c).

5.4.4. NOR Gate

5.4.4.1. NOR Gate Materials and Methods

NOR gates have two inputs and one output and follow the logic in Figure 5.5(b). The NOR gate, as illustrated in Figure 5.5, is a more complex architecture and uses four OECTs, two reference transistors, Q1 and Q2, which behave the same way as Q1 in both the NOT and NAND gates.

Meaning the Q1 and Q2 have their gate shorted to $–V_{DD}$, causing them to always be on, conducting $–V_{DD}$ to the output. Q3 and Q4 must have their output set to HI (0V) for them to turn on and pull the output to GND, thereby setting the output to LO. If the output is LO (1V), then they are not conducting. In other words, both $V_{in,\ A}$ and $V_{in,\ B}$ have to be set to LO for the output to be $–V_{DD}$ (HI), otherwise, either Q3 or Q4 will be conducting, pulling the output to GND (LO). The NOR gate operation should be such that the output is HI when both inputs are LO and a LO output for all other inputs. This behaviour is summarized in the table in Figure 5.5(b).

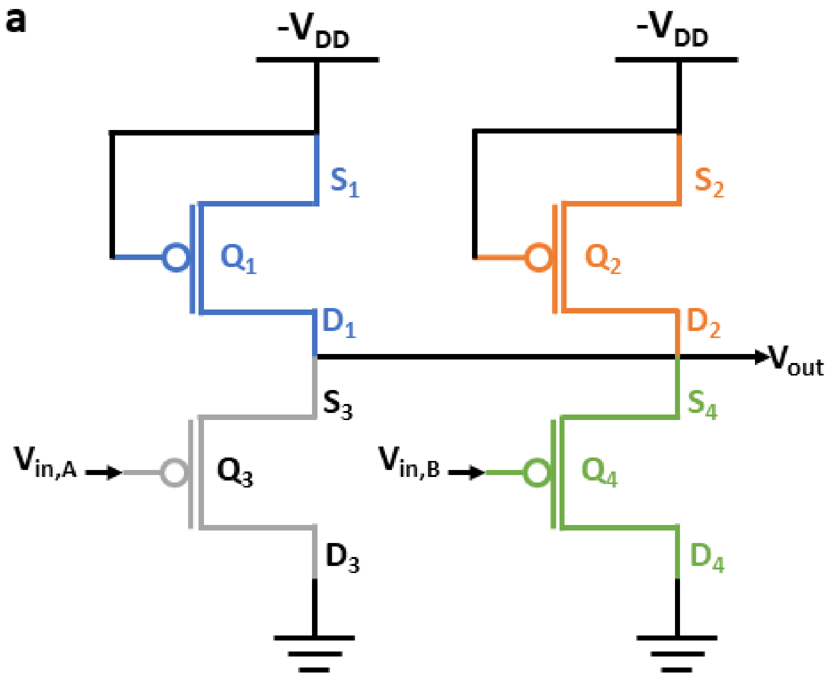

b

$V_{in,A}$	$V_{in,B}$	V_{out}
LO	LO	HI
LO	HI	LO
HI	LO	LO
HI	HI	LO

Figure 5.5 (a) NOR gate schematic. Q1 and Q2 in blue and orange respectively are always ON and conduct -V_{DD} to V_{out}. Both Q3 and Q4 in grey and green respectively, have to both my OFF for V_{out} to be -VDD which is logic HI. Otherwise, V_{out} will be shorted to ground, making the output LO. IN other words, $V_{in,\ A}$ and $V_{in,\ B}$ both need to be LO for V_{out} to be HI, otherwise, V_{out} is LO. (b) NOR Logic Table

5.4.4.2. NOR Gate Results and Discussions

To properly test the NOR gate, the first input must be held HI while the second input is swept from HI to LO. The first input is then held LO and the second input is swept from HI to LO, the output is measured during both of these measurements are then compiled to show the overall response of the gate. The theoretical response of a NOR gate is shown in Figure 5.6(b). When both inputs ($V_{in, A}$ and $V_{in, B}$) are set to LO (1 V), the output (V_{out}) should be HI. All other combinations of $V_{in, A}$ and $V_{in, B}$ should give a LO output. The actual results are shown in Figure 5.6.

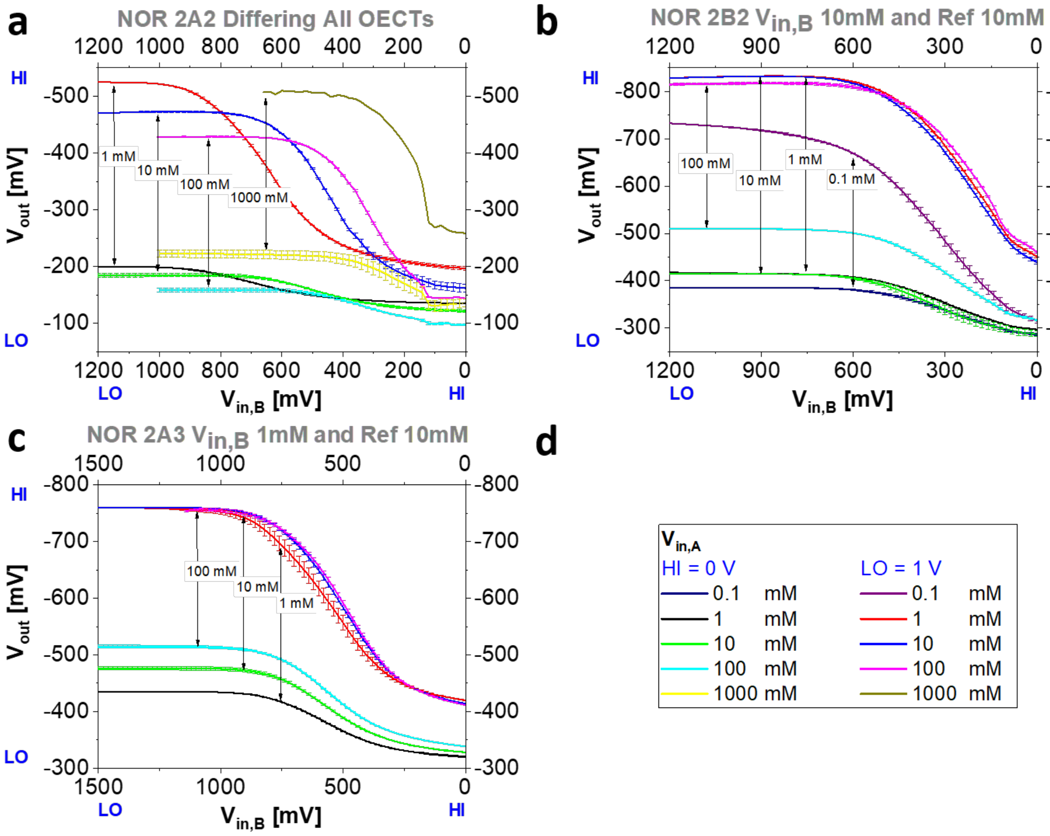

Figure 5.6 Response of a NOR gate showing testing with different electrolyte concentrations. (a) The results 1, 10, 100 and 1000 mM when all OECT electrolyte concentrations match. (b) The results for 0.1, 1, 10, and 100 mM on the $V_{in, A}$ OECT, while $V_{in, B}$ and the reference OECTs are held at 10mM. (c) The results for 1, 10 and 100 mM on the $V_{in, A}$ OECT, while $V_{in, B}$ is held at 1 mM and the references OECT is held at 10 mM. The error bars are calculated using the standard error method. (d) The legend for (a), (b) and (c).

From the measurements shown in Figure 5.6, the NOR gate response is clearly following the expected results shown in Figure 5.5(b) If we consider the purple, red, blue, magenta and brown lines, which is when $V_{in, A}$ is set to LO, and look on the X-axis when $V_{in, B}$ is also LO, we can see that V_{out} is HI. All other combinations of the inputs lead to a LO V_{out}. Therefore, the expected results for a NOR gate are achieved as shown in Figure 5.5(b).

In addition, there is a distinct difference in response when different concentrations of electrolytes are used on the channels. This result is consistent with the NOT gate results seen in the next chapter and the NAND gate results above. As the concentration increases, the required input voltage to switch the output decreases. Again, this is due to the increase in available cations to de-dope the PEDOT:PSS and turns off the channel, thereby requiring less gate voltage to be applied to turn off the OECT.

The results are shown in Figure 5.6 where three different conditions and indicate little change in the results. Figure 5.6 (a) is the result for when all of the OECT electrolytes are varied. Figure 5.6 (b) is the result when only one input is varied ($V_{in, A}$), while the other input ($V_{in, B}$) and the reference OECT are held at 10 mM NaCl. Figure 5.6 (c) is the result when only one input is varied ($V_{in, A}$), while the other input ($V_{in, B}$) is held at 1 mM and the reference OECT is held at 10 mM NaCl. The major difference between these scenarios is that the V_{out} = HI level is more unstable and shift when all of the OECT levels are changed instead of one input, as seen in Figure 5.6 (a). The V_{out} = HI level is more stable when one input and the reference are held at a set concentration as with Figure 5.6 (b) and (c).

5.4.5. MUX

5.4.5.1. MUX Materials and Methods

A MUX is a way to have multiple inputs and a single output, where an input can be selected with a select bit(s) and sent to the output. The number of select bits is N-1 where N is the number of inputs. The simplest mux has two inputs and a single output. The MUX gate was constructed after the testing of the different Logic gates. Its design is shown in Figure 5.7. It was constructed from three NAND gates and one NOT gate. The NOT gate simple supplies the select bit, S, and S'. The MUX is the simplest design with two inputs, and one select bit to show the working principle of the Organic MUX. In this case, the MUX is designed such that when S is set to LO, the V_{out} will mirror $V_{in, A}$ and when S is set to HI, V_{out} will mirror $V_{in, B}$. The MUX design can easily be scaled to add more inputs and select bits by following the same process.

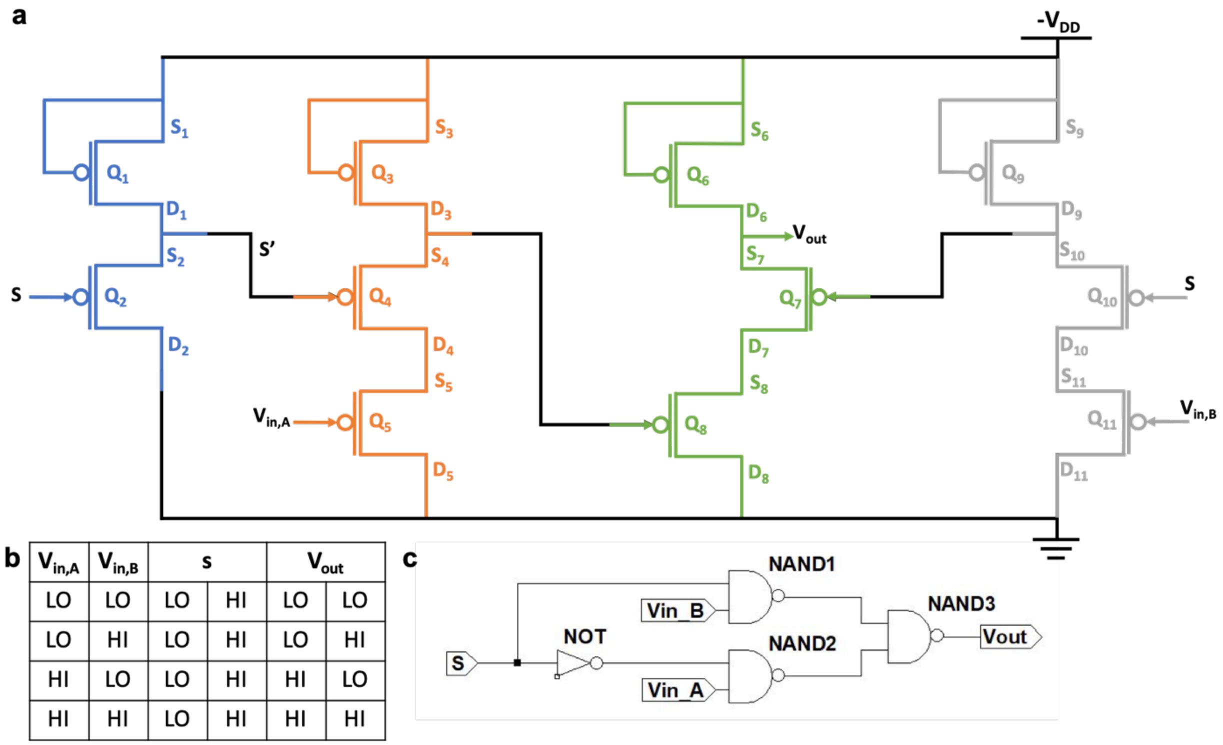

$V_{in,A}$	$V_{in,B}$	s		V_{out}	
LO	LO	LO	HI	LO	LO
LO	HI	LO	HI	LO	HI
HI	LO	LO	HI	HI	LO
HI	HI	LO	HI	HI	HI

Figure 5.7 (a) Simple MUX design using three NAND gates shown in orange, green and grey, and one NOT gate, shown in blue. The output is taken from the second NAND gate (green). Vin, B and the select bit (S) are put into the third NAND Gate (grey), while $V_{in,\ A}$ and the inverse of S (S') are inputs to the first NAND gate (orange). The NOT gate (blue) is used to invert S to S'. (b) Logic table for a two-input MUX. When S is LO, $V_{in,\ A}$ is sent to V_{out} when S is HI, $V_{in,\ B}$ is sent to V_{out}. (c) Schematic showing the constructions of a simple multiplexer with two inputs ($V_{in,\ A}$ and $V_{in,\ B}$) and a single select bit (s).

5.4.5.2. MUX Results and Discussion

The MUX was printed in the same manner as the other gates. However, they offered a significant design challenge as there are several gates. These were printed using a single conductive layer, however, in the future, to make more complex and compact designs, multiple conductive layers, with insulating layers in between could be printed.

The multiplexers were printed but were not functioning when they were tested. This is an area for future work as multiplexing can open many possibilities for multi-entity sensing. The fabricated multiplexer has two inputs and a single select bit. This means that when one input the select bit is HI, the output is set to the first input ($V_{in, A}$), and when the select bit is set to LO, the output is set to the second input ($V_{in, B}$). This behaviour is defined in Figure 5.7 (b).

5.5. Conclusion

Logic gates are an interesting way to use OECTs, allowing for novel applications. NOT gates can be used as threshold sensors and are further discussed in the following chapter. NAND, NOR and NOT gates were successfully fabricated and tested. These logic gates follow their expected operation as defined by their logic tables present in Figure 5.1 (b), Figure 5.3 (b) and Figure 5.5(b). Each of these logic gates has detectable changes in operation due to a shift in the electrolyte concentration. Overall, the required input to switch the output, shifts with the concentration. With an increase in concentration the required switching voltage decreases. With all of the logic gates, this is because as the concentration increases, the concentration of cations increases, meaning that there are more cations to de-dope the PEDOT:PSS, lower the conductivity and turning off the OECT. This translates into a lower input voltage being needed to turn off the OECT.

These basic logic gates, NAND, NOR and NOT, are the building blocks for all other logic circuits and can potentially be used in the building of multiplexers, de-multiplexers or flip-flops. In this chapter, a simple two-input multiplexer design was proposed. Though the MUX was designed and fabricated, no valid results were obtained. However, due to the complex nature of multiplexers, this is most likely due to the construction and design layout of the device instead of an issue with the working principle. This is because the building blocks of the multiplexer, in this case, NAND and NOT gates, are fully functioning separately. Therefore, MUX circuits are an area for future work, as well as using these logic gates to build other logic circuits such as de-multiplexers and flip-flops. The proposed design for the MUX only used a single conductive layer, which leads to a spread-out design adding to the resistance and loss in the circuit. In future work it may be beneficial to add conductive layers, separated by insulating masks to make the design more compact, thereby limiting the losses. Multiplexing has a great potential to be used in sensing as each input can potentially be adjusted by functionalizing the inputs such that each input can sense a different bio-entity specifically. This combines the sensor and takes care of some of the signal processing that is needed. This means that entire sensing circuits can be simply 3D printed, allowing for simple and effective sensing platforms along with the signal conditioning circuitry.

6. Fully 3D Printed OECT Based Logic Gate for Detection of Cation Type and Concentration

6.1. Preface

This chapter was published as “Fully 3D printed OECT based logic gate for detection of cation type and concentration” Majak, D., Fan, J., & Gupta, M. (2019). Sensors and Actuators B: Chemical, 286, 111–118. https://doi.org/10.1016/J.SNB.2019.01.120. It has been reprinted here with permission from Elsevier. The supplementary data that was published online has also been reprinted here as Appendix A. This chapter has been reformatted from its original published version. There is an additional Appendix B at the end of this chapter that is unpublished.

The work presented in this chapter further explores the abilities of OECT logic gates, which were presented in the previous chapter, to act as sensors. This chapter explores NOT gates as cation concentration sensors and demonstrates the ability to distinguish between cation type and concentration. The unpublished appendix presents preliminary data showing the detection of pH levels using these NOT gates.

6.2. Introduction

Flexible electronics have been emerging as a contender for standalone, portable, wearable sensors[127,128] for healthcare monitoring and this is a large industry that is growing, from USD 17.85

Billion in 2017 to USD 40.37 billion by 2023[2]. Flexible electronics are key to the wearables industry as they allow for the conformal application of electronics directly on the skin of the user. Flexible electronics have been made possible with organic semiconductors. The discovery of conductive, conjugated, organic polymers[100,129], allowed for the emergence of organic transistors. The advent of organic transistors has allowed research into non-traditional flexible electronics that mix both organic and inorganic materials. Recent studies have shown the use of organic flexible electronics for different applications. [127,128,164,165]. Organic electrochemical transistor (OECT) is a specific subset of organic transistor first demonstrated in 1984 [100], which is well suited for biological sensing due to its operating mechanism. OECTs behave similarly to the traditional transistors and have three contacts: source, drain, and the gate. How- ever, instead of doped silicon, the channel is made of an organic semiconductor like Poly(3,4-ethylenedioxythiophene)-poly(styrene sulfonate) (PEDOT:PSS) and the ions in an electrolyte are used as part of the gate contact. We have used PEDOT:PSS as the channel material of the OECT in our work. It is a p-type semiconductor whose conductivity can be electrochemically switched by a reversible reaction as shown in (Eq. 6.1).

$$PEDOT^{+}:PSS^{-} + M^{+} + e^{-} \leftrightarrows PEDOT^{\circ} + M^{+}:PSS^{-} \qquad 6.1$$

Where M^+ represents the metal cation and e^- is an electron. When cations, M^+, enter the PEDOT:PSS, they de-dope the PEDOT by interacting with the PSS. When the PEDOT is de-doped, the conductivity of the PEDOT is lowered. When PEDOT:PSS is the channel material for OECTs, the gate electrode pushes cations in the electrolyte into the channel to de-dope it and turn off the transistor. The working principle[105] of OECTs is illustrated in Figure 6.5. By using ions as charged carriers, OECTs have a high transconductance and therefore built-in amplification and high sensitivity; this means they can be driven at lower voltages and have lower power consumption. They are suitable for liquid medium operation due to their working principle. In earlier work, OECTs have been used for bio-sensing[116–118] as they can detect ions present in biological environments. OECTs have also been used to sense pH[75] lactate[126], ion concentration[74,119], hormone levels[122] glucose levels[120,121] and DNA[123–125]. OECTs are well suited to be made into flexible devices as they use organic semiconductors. Flexible devices allow for conformal adherence to different biological tissue topographies which leads to improved sensing of biometric data[127,128]. In this case, the use of PEDOT:PSS, PET, PDMS and flexible silver ink allows for flexible devices to be 3D printed. 3D printing significantly lowers the cost of fabrication as compared to traditional nanofabrication methods (photolithography, sputtering, etc.). Lower fabrication costs for these devices make them more affordable as disposable biosensors. In addition, 3D printing allows for fast fabrication and customizable designs for specific patients or applications. One specific biometric that needs to be measured with flexible sensors is ion concentration levels. Ions are essential for most of the important biological processes in humans and animals. An imbalance of the ion concentration can lead to irregular functioning of the human and animal body. Thus, ionic concentration can be used to predict simple things like hydration state and also complex functionalities like neuron firing and pH regulation[73,166–169]. However, for decades, the concentration of ions has been determined by ion-selective electrodes (ISE), also known as specific ion electrodes. These devices convert the concentration of a specific ion in-solution into an electrical potential. Ion-selective electrodes use ion-selective membranes made from either glass, crystalline/solid-state, polymer, gas sensing or enzyme membranes in conjunction with a reference electrode. These sensors are accurate but often large and expensive and require large sample sizes, which means they cannot be used effectively as sensors for in-situ sensing. In order to overcome this issue, as well as to address the need for better-suited sensors for bio-applications, several methods and applications have been demonstrated. Some methods include: in-vivo sodium concentration sensors[170], ion-selective nano-optodes incorporating quantum dots[171], and fluorescent nanoparticles[172]. Other concentration sensing methods that have been demonstrated earlier are for glucose sensors using CVD grown graphene-based FETs[173], and ammonia detectors using PEDOT:PSS[129]. However, there is still a need for reliable ionic concentration sensors that are wearable and that can be incorporated into larger circuitry for more robust, wearable, sensor devices. In order to make flexible ionic concentration sensors that can be incorporated into larger wearable devices, the first step is to expand on the basic building block of OECTs. In this case, the PEDOT:PSS based OECTs can be combined to create logic circuits which can be used to extend the sensing capabilities of the OECT[65]. Though accumulation mode (normally OFF) OECTs have been demonstrated[174], the natural state of a PEDOT:PSS based OECT is depletion mode (normally ON). By using logic gates for sensing, both data processing and sensing can be conducted with the same device. Specifically, a simple inverter design using two depletion-mode OECTs can be used to detect pH and ion concentration levels by operating one of the devices at the reference level. The devices demonstrated by us are 3D printed on flexible substrates, making them well suited for flexible wearable biomedical sensors. This fabrication method, as compared to nanofabrication, allows for an uncomplicated, economical, reproducible and commercializable method of production. We have demonstrated repeatable and reproducible performance of these logic gates.

6.3. Materials and Methods

6.3.1. Device Design and Operation

An inverter (NOT gate) was designed using the p-type depletion-mode OECTs, which use PEDOT:PSS as the channel material as shown in Figure 6.1(a) – (d). The device inverts a HI input signal to a LO output signal and vice versa. An inverter built with OECTs can be used as a sensor by simply shifting the LO and/or HI level from the reference HI and LO levels. Traditionally, complementary (both n- and p-type) accumulation mode transistors are used to make inverters. Only one type of transistor, p-type (depletion mode), device has been used to design the inverter which simplifies the fabrication. Using depletion-mode transistors means that the gate-source voltage has to be greater than zero ($V_{GS}>0$) for the channel to de-dope and lower its conductivity (turn OFF). We have assigned HI logic to $-V_{DD}$ and LO logic to 0 V. The logic gate operation is indicated by the states in the table inserted in Figure 6.1(f). For the inverter to perform as desired, transistor Q1 (Figure 6.1(e)), must have the gate and source shorted together; at this node, the device bias ($-V_{DD}$) was applied, which ensures that the gate-source voltage (V_{GS}) is always equal or less than zero ($V_{GS} \leq 0$). This ensures that the Q1 transistor is always ON and conducts the bias of $-V_{DD}$ to the output terminal. The input as a voltage sweep is applied to the gate of the transistor Q2 (Figure 6.1(e)) while the drain is grounded. This configuration means that Q1 will always be conducting, making the output HI ($-V_{DD}$). However, depending on the voltage applied to the gate of Q2, the channel will either turn ON, shorting the output to ground, or turn OFF, leaving the output HI ($-V_{DD}$). In other words, the input voltage of the device needs to be less negative than the biasing ($V_{GS} \leq -V_{DD}$) to turn OFF Q2, and it should be more negative than the biasing ($-V_{DD}$) to turn it ON.

6.3.2. Fabrication and Materials

The inverter devices were completely 3D printed using an nScrypt 3Dn-Tabletop 3D printing and micro-dispensing system. These sensors can be printed using only four layers: the substrate (printed or bought), silver electrodes (printed), PEDOT:PSS channel (printed) and a mask, PDMS in this case (printed). The devices were printed on polyethylene terephthalate (PET) substrate, specifically, MELINEX® ST506 provided by DuPont Teijin Films (125 μm) which come pretreated with an adhesion promoter. Next, DuPont CB028 silver conductive paste, 12.706 ± 1.384 μm thick, was used to print the electrodes which have a trace width of 300 μm with 600×1000 μm2 source and drain electrode pads for easier probe landing. After printing of the electrodes, the silver was cured on the printer bed at 130 °C for 60 min. Next, the PEDOT: PSS Orgacon™ EL-P-5015 channel was printed with the length, L=416.874 ± 7.642 μm, width, W=953.081 ± 14.058 μm and thickness, t=9.056 ± 0.559 μm and cured on the printer bed at 100 °C for 30 min. The film thickness was chosen due to the fabrication technique and for a film with an average thickness of 9.35 μm (n=2), the conductivity was measured to be 0.0139 S/cm. A polydimethylsiloxane (PDMS) solution was prepared using a 10:1 mixture with a crosslinker, specifically the SYLGARD® 184 silicone elastomer kit from Dow Corning. This PDMS solution was used to print a mask to prevent electrical short during measurements, which was then cured in a vacuum oven at 70 °C for 180 min. The gate and drain for Q1 are shorted together and therefore, the shorting connection must be covered so that it is not in contact with the electrolyte.

6.3.3. Materials and Characterization

All the electrical characterizations were conducted using a Keithley 4200- Semiconductor Characterization System (SCS Analyzer) with an electrolyte. Prior to testing the logic device, the individual OECTs were characterized to obtain their transconductance and ON/OFF ratios. The individual OECT characterization was conducted over a gate voltage of 0 to 1 V with 0.1 V step size. For each gate voltage step, the drain voltage is swept by −0.05 V steps from 0.2 V to −0.8 V to obtain the family of curves. The drain and gate current were measured with the source being grounded. From the family of curves, the transconductance (g_m) can be extracted as $\mathbf{g_m}=\Delta I_D/\Delta V_G$ at a specific drain voltage, V_D. Additionally, the transfer curve, which is the drain current (I_D) versus the gate voltage (V_G), can be plotted by extracting the values at a set drain voltage (V_D). From the transfer curve, the ON/OFF ratio can easily be extracted by taking the ratio of the maximum to minimum drain current. For these measurements, an external gate electrode of Ag/AgCl probe was used. The electrode was prepared by placing a pre-cleaned silver wire into a bleach solution to create an Ag/AgCl probe. This probe was placed in the electrolyte solution for the measurements. For future bio-wearable applications, this gate electrode will be printed to obtain planar devices.

Once the individual OECTs were characterized, all the inverter logic gates were tested. According to Figure 6.1(e), the source and gate of Q1 were biased to −300 mV, the gate of Q2 had a voltage sweep applied, the drain of Q2 was grounded and the output voltage was measured. The reference electrolyte was placed on Q1 and maintained for the entire measurement, whereas the pH or ion concentration of the solution on Q2 was changed. When the electrolyte was changed, the same procedure was followed for the different electrolyte concentration measurements. (1) Before the electrolyte concentration was changed, we waited five minutes after removing the bias to allow for the channel to re-dope, (2) the electrolyte was pipetted away, (3) the channel was rinsed 3–5 times with distilled water to remove any contamination, and (4) the electrolyte solution was then left on the channel for five minutes before voltage was applied and measurements were taken.

These wait times were maintained to ensure accurate readings from the lower concentrations, like 1 mM, and to maintain consistent procedures for all the measurements.

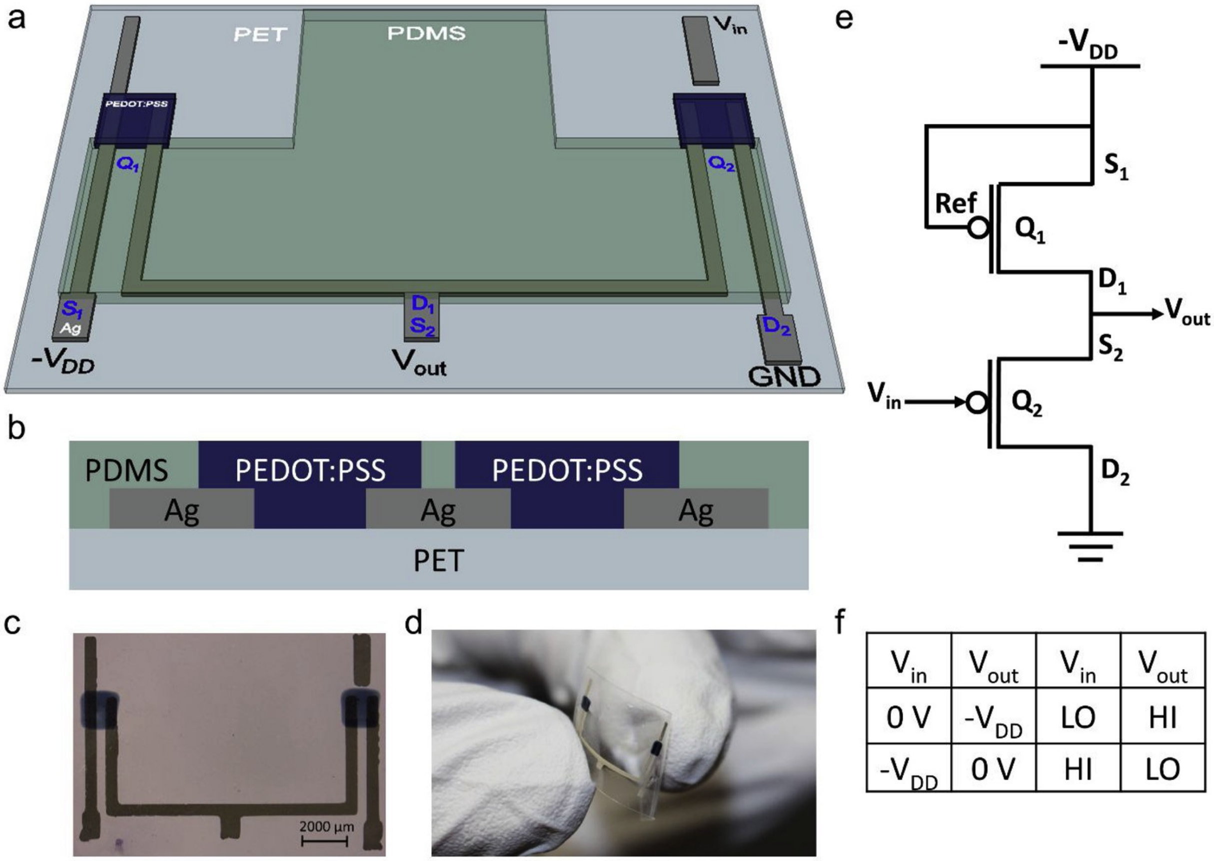

V_{in}	V_{out}	V_{in}	V_{out}
0 V	$-V_{DD}$	LO	HI
$-V_{DD}$	0 V	HI	LO

Figure 6.1(a) 3D rendering of the inverter design which shows the silver source (S1, S2) and drain (D1, D2) with the PEDOT:PSS channel for the transistors (Q1 and Q2)on a PET substrate and PDMS mask. (b) The cross-section of the inverter design. (c) Microscope image of the cross-section of a single 3D printed inverter design with silver contacts and PEDOT:PSS channel, note that the PET and PDMS are transparent and are not visible. The device terminals directly correspond to the terminals in part (a). The scale bar for the image is 2000 µm. (d) A single logic gate sensor being flexed. (e) Schematic of inverter design where Q1 and Q2 are the two transistors with the connections for all the terminals. V_{in} *and* V_{out} *are the input and output of the inverter. Here, Q1 is maintained at a reference concentration such that it is always ON as its drain D1 and gate are shorted and are connected to* $-V_{DD}$*. (f) Inverter logic gate functioning is shown in the Table for the input and output where logic HI is ideally* $-V_{DD}$ *and logic LO is 0 V.*

6.4. Results and Discussion

6.4.1. Individual OECT Characterization

The individual OECTs were tested at 100mM concentration, which

was used as the reference concentration for all the inverter tests. The tests were conducted using three different electrolytes (NaCl, CaCl2 and KCl) to test for ion and pH measurements. The devices were tested and characterized using the procedure described in the methods section. Figure 6.2(a) – (f) shows the transconductance and transfer curve (drain current versus gate voltage) plots for the OECTs (both Q1 and Q2) for 100mM of NaCl, CaCl2, KCl concentration. The curves are generated for a drain voltage of −300 mV as this was the voltage used to bias the device (V_{DD} = −300 mV, Figure 6.1(e)). The peak transconductance was extracted for Q1 and Q2 for NaCl, CaCl2 and KCl at 100mM concentration and is shown in Table 6.3. However, the transconductance of Q2 really indicates the sensitivity of the inverter device as Q1 is always ON and Q2 is actively sensing. All of the electrolytes have a peak in transconductance at a gate voltage of 0 V or 0.1 V. As the maximum transconductance voltage occurs within the voltage of 0–0.3 V, the power consumption of these devices is small, and this also makes them suitable for biosensing. The ON/OFF ratios of all the devices are also shown in Table 6.3and range from 598 to 2064, indicating good signal detection between ON and OFF states.

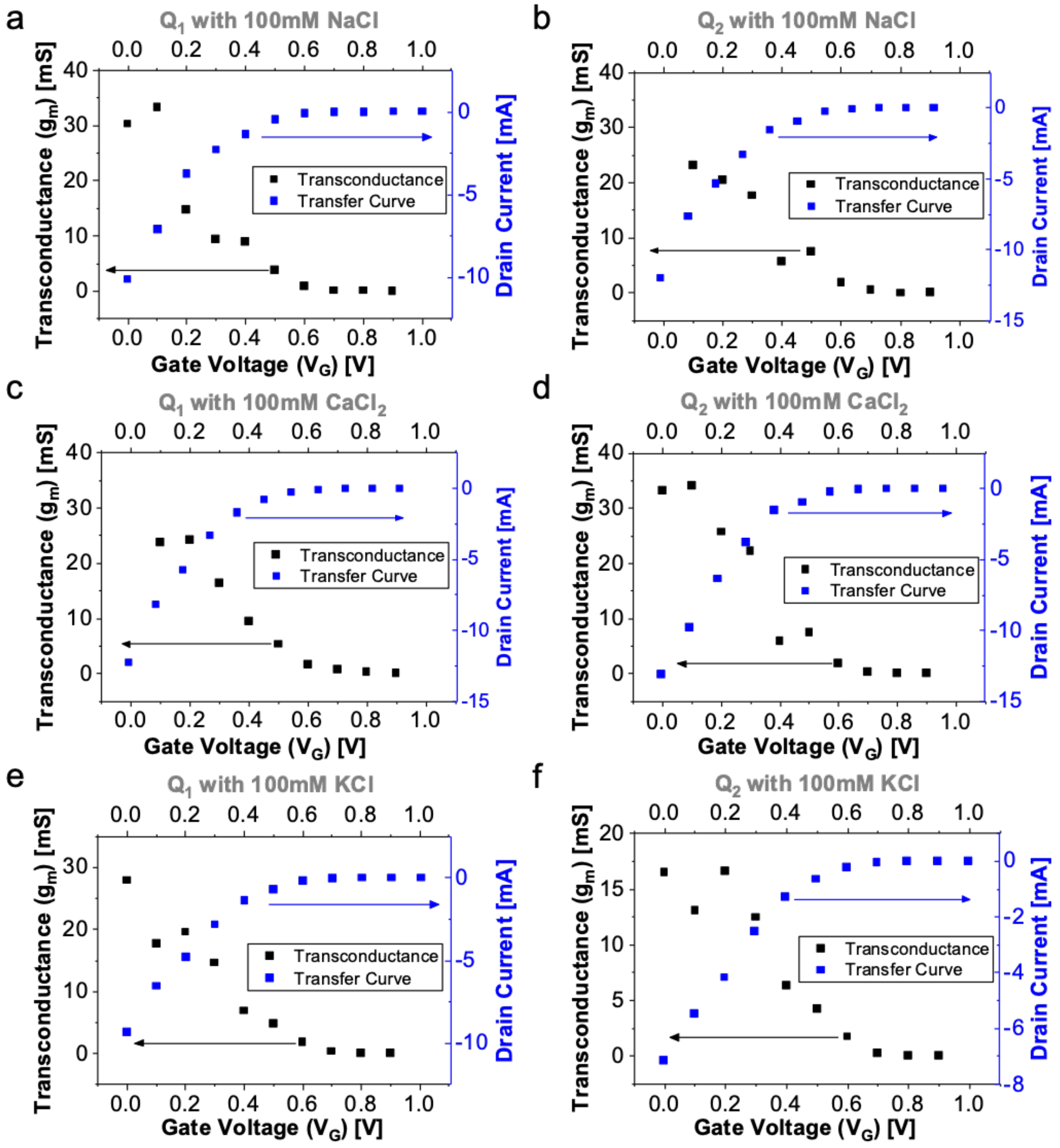

Figure 6.2 Transfer curve (right y-axis, blue color) and transconductance curve (left y-axis, black color) at 100mM electrolyte concentration for (a) NaCl Q1, (b) NaCl Q2, (c) CaCl2 Q1, (d) CaCl2 Q2, (e) KCl Q1 and (f) KCl Q2. These are extracted from the IV measurements shown in Figure 6.6. The curves are selected at a V_D of −0.3 V while V_G is stepped from 0 to 1 V in steps of 0.1 V. These curves show peak transconductance either at V_G of 0 or 0.1 V. Each electrolyte was tested on a different device to prevent cross-contamination. (For interpretation of the references to colour in this figure legend, the reader is referred to the web version of this article).

6.4.2. Inverter Device Operation

After the individual OECTs were characterized for their transconductance and ON/OFF ratio, the inverter tests were conducted. For these tests, Q1 was maintained at a reference level of 100mM for all the different electrolytes and the concentration of the electrolyte was sensed using Q2. When the output is LO, Q2 is ON, grounding the output. When Q2 turns OFF, the output switches to HI ($-V_{DD}$). When the sensed electrolyte concentration on Q2 changes, the input voltage required to switch the output from LO to HI, which will be denoted as $V_{in,\ switch}$, also shifts. Figure 6.3(a) – (c) shows the output-input voltage (V_{out} -V_{in}) curves for the inverter for the three different electrolytes (NaCl, $CaCl_2$, KCl) at four different concentrations (1 mM, 10 mM, 100mM and 1000 mM). From the plots, it can be seen that a shift in $V_{in,\ switch}$ is observed for each electrolyte concentration (NaCl, $CaCl_2$, KCl). This shift in $V_{in,\ switch}$ can be explained based on the electrolyte concentration. The lower the electrolyte concentration, the fewer the ions that are available to de-dope the channel and turn OFF Q2. For the sensed concentrations of 1mM and 10mM (both lower than the reference of 100 mM), we observe that the switching of the output from HI to Lo ($V_{in,\ switch}$) occurs at a higher voltage as compared to the 100mM (same as the reference) concentration. However, for concentrations higher than the reference concentration, such as 1000 mM, $V_{in,\ switch}$ is at a lower voltage. This is because one requires a higher voltage to drive in the fewer ions available in the electrolyte (1 mM and 10 mM) samples as compared to the larger concentration samples (100mM and 1000 mM). Also, it can be observed that the transconductance for Q2 increases from KCl (16.63 mS) to CaCl2 (34.17 mS) to NaCl 43.32 mS) (also shown in Table 6.3). Lower transconductance indicates lower sensitivity for KCl as compared to CaCl2 and NaCl. The measurements shown in Figure 6.3(a) – (c) are conducted on three different devices, one for each electrolyte, to avoid cross-contamination. To ascertain that the results are similar measurements were conducted on the same device using all the three electrolytes which are shown in Figure 6.3(d) – (g). The error of measurement in $V_{in,\ switch}$ was found to be within 1.3% and 10.3%. Based on the transconductance (sensitivity) as seen in Figure 6.2(a) – (f), we can directly correlate our measurements to predict the type of ion we are sensing. Thus, the sensing capabilities of the inverter can be extended to distinguish between different metal ions present in the electrolyte; in this case, Na^+, Ca^{2+}, and K^+. Figure 6.3(d) – (g) shows output-input voltage (V_{out} -V_{in}) comparison curves for the inverter for the three different electrolytes (NaCl, $CaCl_2$, KCl) at one concentration in each plot (1 mM, 10 mM, 100mM and 1000 mM), which were measured on the same device that was washed after a change in electrolyte or concentration. We clearly observe a shift in the input voltage required to change the output from HI to LO ($V_{in,\ switch}$) for the different electrolytes, as mentioned earlier. Thus, $V_{in,\ switch}$ is different for the three electrolytes for the same electrolyte concentration, with NaCl requiring the highest voltage and KCl requiring the least. These results show a definite shift in $V_{in,\ switch}$ depending on the concentration and the ion; in other words, the V_{in} necessary to turn OFF Q2, and switch the output to HI. These results can be explained by ionic radius and ionic charge, this is presented in Section 6.4.3.

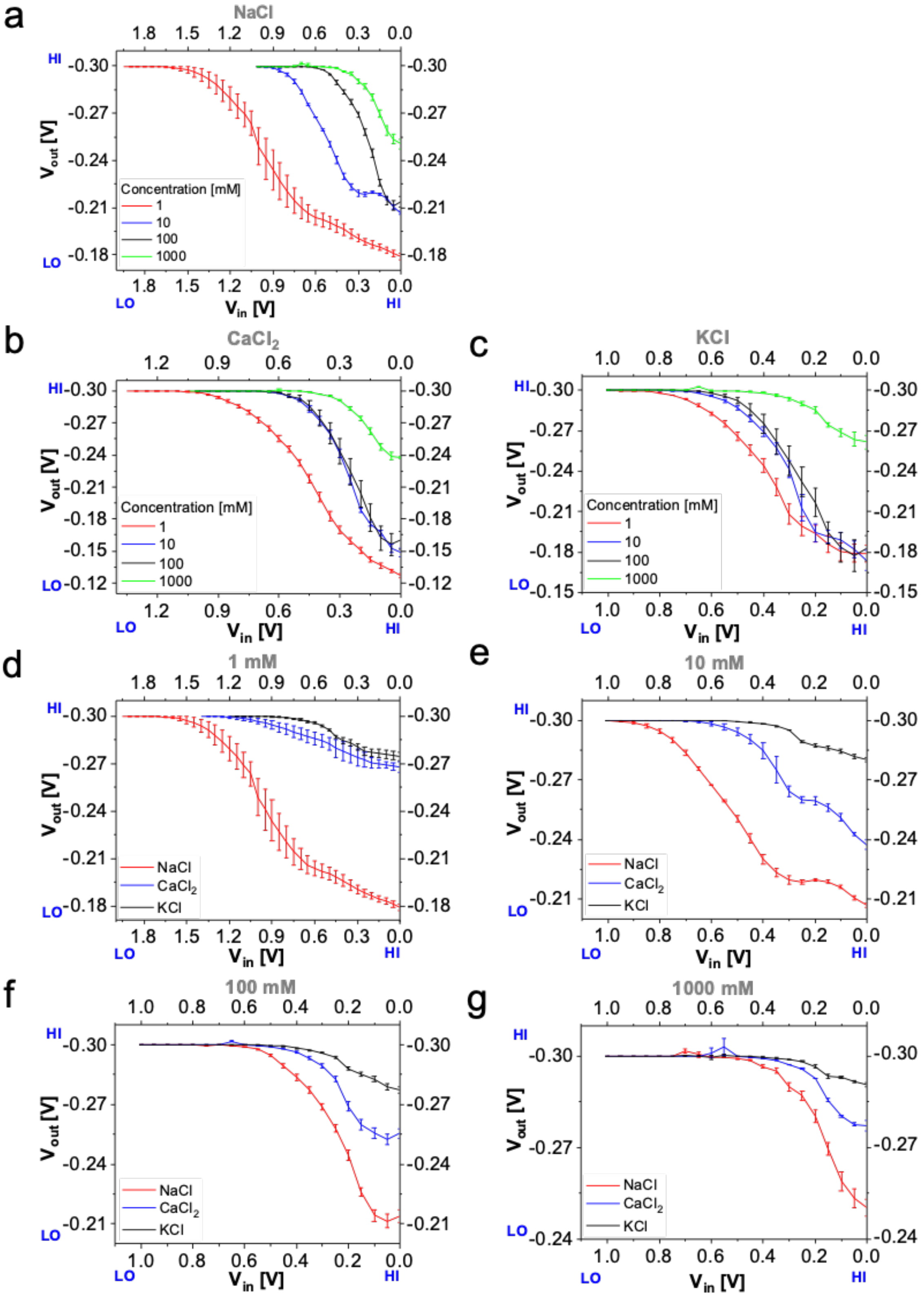
a
NaCl
1.8 1.5 1.2 0.9 0.6 0.3 0.0
HI -0.30
-0.27
-0.24
-0.21
LO -0.18
V_{out} [V]
Concentration [mM]
1
10
100
1000
V_{in} [V]
LO
HI
b
$CaCl_2$
1.2 0.9 0.6 0.3 0.0
HI -0.30
-0.27
-0.24
-0.21
-0.18
-0.15
LO -0.12
V_{out} [V]
Concentration [mM]
1
10
100
1000
V_{in} [V]
LO
HI
c
KCl
1.0 0.8 0.6 0.4 0.2 0.0
HI -0.30
-0.27
-0.24
-0.21
-0.18
LO -0.15
V_{out} [V]
Concentration [mM]
1
10
100
1000
V_{in} [V]
LO
HI
d
1 mM
1.8 1.5 1.2 0.9 0.6 0.3 0.0
HI -0.30
-0.27
-0.24
-0.21
LO -0.18
V_{out} [V]
NaCl
$CaCl_2$
KCl
V_{in} [V]
LO
HI
e
10 mM
1.0 0.8 0.6 0.4 0.2 0.0
HI -0.30
-0.27
-0.24
LO -0.21
V_{out} [V]
NaCl
$CaCl_2$
KCl
V_{in} [V]
LO
HI
f
100 mM
1.0 0.8 0.6 0.4 0.2 0.0
HI -0.30
-0.27
-0.24
LO -0.21
V_{out} [V]
NaCl
$CaCl_2$
KCl
V_{in} [V]
LO
HI
g
1000 mM
1.0 0.8 0.6 0.4 0.2 0.0
HI -0.30
-0.27
LO -0.24
V_{out} [V]
NaCl
$CaCl_2$
KCl
V_{in} [V]
LO
HI

Figure 6.3 Output voltage versus input voltage response for separate electrolytes along with standard error bars. Each concentration was tested multiple times and the results were averaged. (a) NaCl, (b) CaCl2 and (c) KCl at concentrations of 1 mM, 10 mM, 100mM and 1000mM with a reference of 100 mM. The plots shown in (a) – (c) were measured on different devices to eliminate cross-contamination. The HI output occurs when Q2 turns OFF, and the output is $-V_{DD}$*. The LO output occurs when Q2 turns ON, and the output is pulled to ground. The sensed electrolyte on Q2 was the same as the reference electrolyte but at varying concentrations. Comparison of input versus output voltage for NaCl, CaCl2 and KCl with a reference concentration at 100mM and a sensed concentration at (d) 1 mM, (e) 10 mM, (f) 100mM and (g) 1000 mM. All reference concentrations were set to 100mM on Q1 and a -0.3 V bias. The HI (*$-V_{DD}$*) output occurs when Q2 turns OFF and the LO (ground) output occurs when Q2 turns ON. The sensed electrolyte matched the reference electrolyte. Each concentration was tested multiple times and the results were averaged. Error bars were added based on standard error. Plots (d) – (g) show tests that were done on the same device which was washed after each concentration and electrolyte change. (For interpretation of the references to colour in this figure legend, the reader is referred to the web version of this article)*

6.4.3. Shift in Response Due to Cation Type

The OECT can also be used to identify the different cations, which is exhibited through the shift in V_{in} required to shift the output from LO to HI ($V_{in,\ switch}$). Figure 6.4 shows V_{in}, switch versus the concentration plotted for the different electrolytes (NaCl, $CaCl_2$, KCl) and concentrations (1 mM, 10 mM, 100 mM and 1000 mM). It can be observed that $V_{in,\ switch}$ is different for the three electrolytes at the same concentration. The observed $V_{in,\ switch}$ for the different ions can be directly correlated to the cation mobility, as shown in Table 6.1 ($\mu_{Na+} < \mu_{Ca2+} < \mu_{K+}$ at 298 K)[175]. The inverse ratio of the input $V_{in,\ switch}$ with respect to KCl matches very closely with the ionic mobility ratio with respect to KCl, as shown in Table 6.1 which summarizes all the switching voltage and the ratios. The values shown in the Table 6.1 were extracted from measurements done on the same device that was washed after each electrolyte and concentration change. Compared with measurements done on separate devices, the error in $V_{in, switch}$ is between 1.3% and 10.3%. Thus, the switching voltage, $V_{in, switch}$, is seen to be directly related to the ionic mobility and is larger for small ionic mobility and vice versa. This can also be observed directly from Figure 6.4, which can be used to predict the cation type based on the input voltage shift. Hence, we observe the highest change in voltage for Na^+ as compared to Ca^{2+} and K^+ (which is inverse of their mobilities). From Figure 6.4, we observe two different linear regimes of sensitivity, one from 1 to 100mM and the other from 100 to 1000mM range, for all the three different ions. Another important feature to observe is that the lower concentration region (1–100 mM) demonstrates a much higher sensitivity as compared to the higher concentration region (100–1000 mM). We have extracted the voltage sensitivity of our devices using the slopes of the two linear regimes as $\Delta V_{in, switch}/\Delta c$ (mV/ dec). Table 6.2 shows the comparison of our sensitivity for the different ions and ranges along with the channel thickness reported in other work. It should be noted that our results well surpass the theoretical Nernst limit of 59.2 mV/dec (for a charge of +1 at 300 K). The only exception is observed for K^+ in the concentration range of 10mM–1000 mM. The devices from our work demonstrate nearly a five-fold higher sensitivity for the Na^+ ions as compared to the other studies. For lower electrolyte concentration we observe higher sensitivity as compared to the higher electrolyte concentrations which have been also observed in other studies[73].

Table 6.2 also shows the limit of detection (LOD) for the different sensors. Even though the LOD of our sensors is 1mM for all the different electrolytes, we can improve it by optimizing the device operation parameters. Also, because we have used thicker channel devices, our devices demonstrate much larger transconductance, which means higher sensitivity. Although the thicker channel provides us with larger sensitivity, it also makes the response time of our devices slower due to larger capacitance. To improve our devices further, channel thickness optimization is required to obtain a good balance between the sensitivity and response time. Additionally, adjusting the W/L ratio (which was 2.292 ± 0.052), can directly increase the sensitivity and current levels of the device. One of the biggest advantages of this sensor is the simplicity of its design and ease of fabrication, which can be customized based on the application. These advantages make it an ideal candidate for wearable, flexible, sensors. In this work, we have not conducted any tests of the flexibility of the sensors which will be part of the future work. In addition, by making the sensors as a logic gate, the sensing and the data processing can be performed in the same circuit with a single active component, thereby reducing the power consumption and the noise in the system. Another important functionality, which is required in a multi-channel sensor, is the multiplexing circuitry, which is normally performed separately from the sensing. Utilizing the logic gates, multiplexing capability can be included on the sensor circuit, which reduces the extent of external electronics required and also reduces the noise.

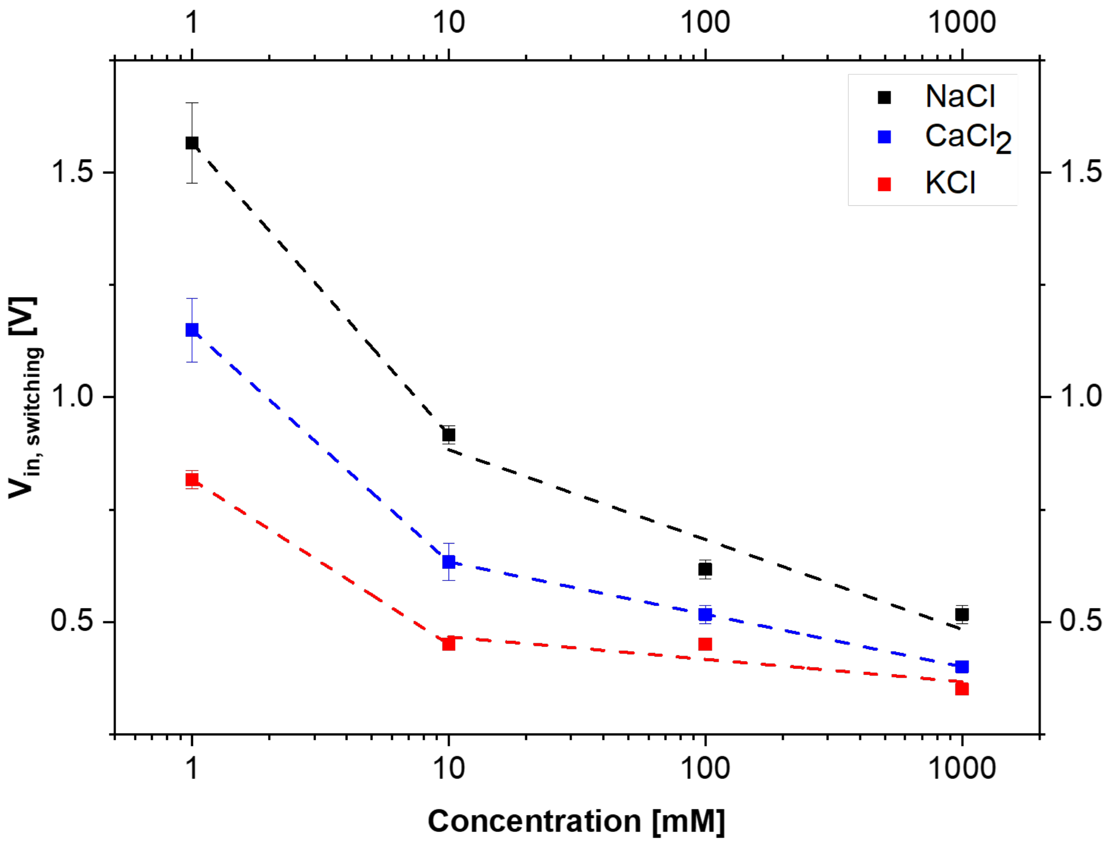

Figure 6.4 The electrolyte concentration vs the switching input voltage. The switching input voltage is taken as the first point that the output voltage reaches −0.299 V. The reference was set at 100mM for NaCl, CaCl2 and KCl and sensed at concentrations of 1 mM, 10 mM, 100mM and 1000 mM. The sensed electrolyte matched the reference electrolyte. The plot shows the data for an average of three measurements with the standard error used for the error bars. This data is extracted from measurements done on the same device that was washed after each electrolyte and concentration change shown in Figure 6.3(d) – (g). (For interpretation of the references to colour in this figure legend, the reader is referred to the web version of this article)

6.5. Conclusion

Inverters based on p-type depletion-mode OECTs have been designed and implemented using 3D printing. These OECTs exhibit transconductance as high as 43 mS which indicates very high sensitivity. These sensors demonstrate sensitivities as high as 650 mV/dec for Na^+ which is five-fold higher than the other reported work. Also, these devices demonstrate a switching voltage which can be directly correlated to the ionic mobility and hence can be used to directly distinguish between different cations. As the sensor is based on a logic gate it can directly be integrated and used for sensing as well as multiplexing using a single active component.

Table 6.1 Switching voltages for different electrolytes NaCl, CaCl2 and KCl for different concentrations of 1 mM, 100 mM, 1000 mM. The switching voltage, $V_{in, switch}$, for the different ions can be directly correlated to the cation mobility ($\mu_{Na+} < \mu_{Ca2+} < \mu^{K+}$ at 298 K) This data is extracted from measurements done on the same device that Na^+ Ca^{2+} K^+ was washed after each electrolyte and concentration change shown in Figure 6.3(d) – (g). Electrolyte

Electrolyte	**NaCl**	**$CaCl_2$**	**KCl**
Ionic mobility (x 10^{-8} m^2/V.s)	5.19	6.17	7.62
Ratio of mobility with respect to KCl	0.681	0.810	1.000
Concentration [mM]	**Switching Vin [V]**		
1	1.567 ± 0.089	1.150 ± 0.071	0.817 ± 0.020
Inverse ratio of switching voltage with respect to KCl	0.522	0.712	1.000
10	0.917 ± 0.020	0.633 ± 0.041	0.450 ± 0.000
Inverse ratio of switching voltage with respect to KCl	0.49	0.681	1.000
100	0.617 ± 0.020	0.517 ± 0.020	0.450 ± 0.000
Inverse ratio of switching voltage with respect to KCl	0.73	0.872	1.000
1000	0.517 ± 0.020	0.400 ± 0.000	0.350 ± 0.000
Inverse ratio of switching voltage with respect to KCl	0.678	0.875	1.000

Table 6.2 Sensitivity, change in voltage per concentration (mV/dec), and limit of detection (LOD) (mM) comparison of our sensors with other reported ion sensors. It can be observed that our sensitivity for Na+ is five-fold greater than the other reported values. Also, our LOD is comparable to most of the other reported sensors.

Technology	**Ion**	**ΔV/ΔC [mV/dec]**	**LOD [mM]**	**Reference**
OECT	Na^+	135	10	[73]
OECT	Na^+	98	0.1	[73]
OECT	K^+ (with Pt gate)	79.6	1	[74]
OECT	K^+ (with Au gate)	135	1	[74]
OECT	K^+ (with Ag/AgCl gate)	59.4	0.001	[74]
OECT	Na^+ (with Ag/AgCl gate)	57.7	1	[74]
OECT	Ca^{2+} (with Ag/AgCl gate)	29.7	1	[74]
ISE	Na^+	64.2	1	[62]
CNT ISE	Na^+	58	.00316	[72]
OECT Inverter	Na^+ (10 mM-1000 mM)	200	1	This Work
OECT Inverter	Na^+ (1 mM-10 mM)	650	1	This Work
OECT Inverter	Ca^{2+} (10 mM-1000 mM)	116.67	1	This Work
OECT Inverter	Ca^{2+} (1 mM-10 mM)	516.67	1	This Work
OECT Inverter	K^+ (10 mM-1000 mM)	50	1	This Work
OECT Inverter	K^+ (1 mM-10 mM)	366.67	1	This Work

6.6. Acknowledgements

The authors would like to acknowledge Alberta Innovates and NSERC grant number 06096 for providing for this work.

6.7. Appendix A Supplementary Data

Supplementary material related to this article can be found, in the online version, at doi:https://doi.org/10.1016/j.snb.2019.01.120.

Figure 6.5 shows the working principle of OECTs. In this case, the channel material is made from PEDOT:PSS, which is de-doped by cations, this lowers the conductivity of the channel which turns off the transistor.

Figure 6.6 (a) - (f)) shows I_D-V_D curves for different V_G can be used to extract the transconductance and ON/OFF ratios for the OECT for different electrolytes NaCl, $CaCl_2$ and KCl. Also, the IV family of curves indicates that all the OECTs turn OFF between 500 to 700 mV as seen from the curves. It is observed that the drain current decreases with subsequent voltage sweeps, which is due to the thick (9.055 ± 0.559 μm) PEDOT:PSS channel. The ON current for the device lowers with subsequent IV measurements as there is no driving force for cations to be removed from the channel and the channel remains partially de-doped. This leads to a permanent decrease in the ON current level. This lowering in ON current is more significant after the first few IV measurements but begins to settle afterwards. This result is observed repeatedly through multiple trials and with all the different electrolytes.

The transconductance and ON/OFF ratios were extracted from the IV curves at a drain voltage of -300 mV by the method described in the main text. The peak transconductance and the gate voltage at which it occurs, as well as the ON/OFF ratio, is presented in Table 6.3.

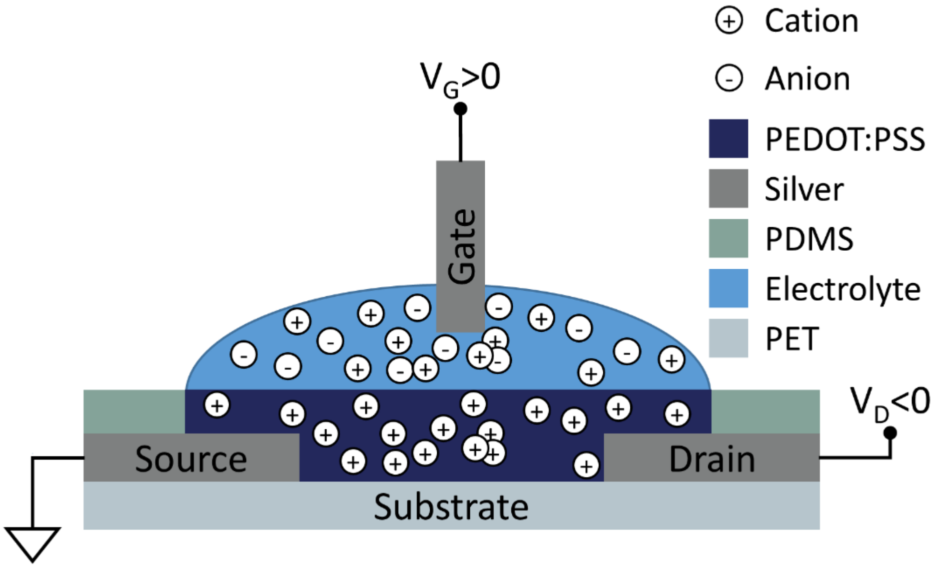

Figure 6.5 Working principle of OECTs, showing the cations in the channel and biasing of the device.

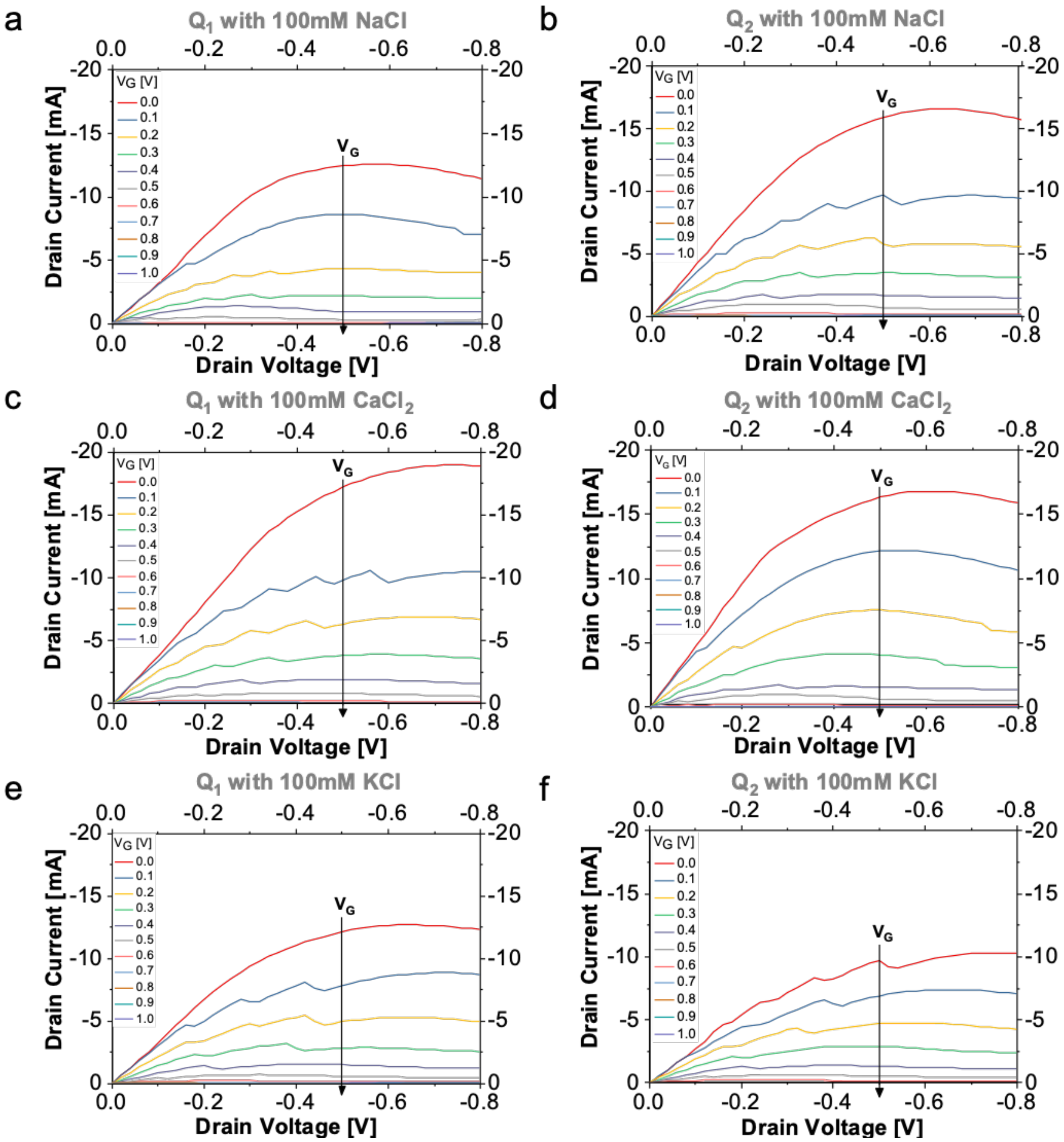

Figure 6.6 IV curves of Q1 and Q2 OECTs of the inverter at 100 mM concentration of NaCl, KCl and CaCl2 electrolytes. (a) and (b) show the characteristics of Q1 and Q2 for NaCl. (c) and (d) show the characteristics of Q1 and Q2 for CaCl2 Q2. (e) and (f) show the characteristics of Q1 and Q2 for KCl. For the measurements, VD is swept from 0.2 V to -0.8 with steps of -0.02 V while VG is varied in the range of 0 - 1 V with 0.1 V step. These curves indicate that both Q1 and Q2 turn OFF and are performing as desired, therefore they will function in a larger inverter configuration. Each electrolyte was tested on separate devices to prevent cross-contamination.

Table 6.3 The peak transconductance values and the ON/OFF ratios for 100 mM concentration of NaCl, CaCl2 and KCl for Q1 and Q2, taken at VD = -0.3 V

		Q_1			Q_2		
		g_m [mS]	V_G [V]	I_{ON}/I_{OFF}	g_m [mS]	V_G [V]	I_{ON}/I_{OFF}
Electrolyte	NaCl	33.29	0.10	1899.73	43.32	0.00	774.80
	$CaCl_2$	41.07	0.00	2064.86	34.17	0.10	1688.58
	KCl	27.86	0.00	1064.30	16.63	0.20	598.28

6.8. Appendix B pH Sensing with NOT Gates

Preliminary work with pH sensing was done, proving that the same shift in the required input voltage to reach a HI output level of -299mV. The trend follows the ion concentration sensing as pH sensing is simply H+ concentration, as pH decreases, H+ concentration increases. In this test, devices were tested with a 3D printed PDMS substrate, instead of a PET substrate. The device had slightly different dimensions (W/L=2.275±0.152) than the PET devices (W/L=2.292±0.052). All other materials were the same, silver electrodes (z=15.737±0.887 µm), a PEDOT:PSS channel (z=10.929±0.496 µm) and a PDMS mask. The reference Q1 was set at a pH of 7.03 while the sensed concentration changed to 7.03, 4.00 and 2.10, which correspond to 9.33X10-5mM, 0.10mM and 7.94mM respectively. This shows that the limit of detection is lower than that tested with the different electrolytes NaCl, $CaCl_2$, and KCl of 1mM. The same trend was observed with the pH sensing as the ion sensing.

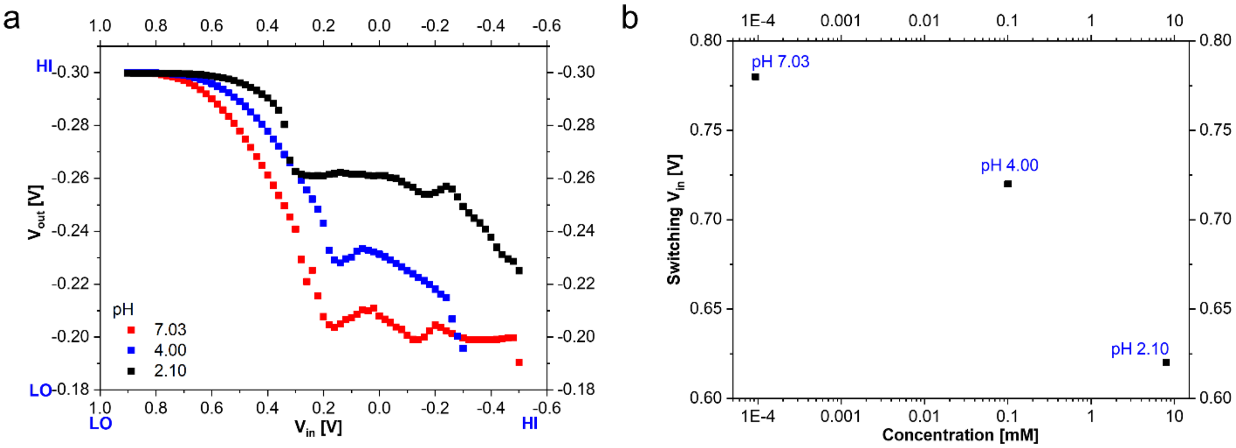

Figure 6.7 Output voltage versus input voltage response for (a) PBS reference at 7.03 and sensed PBS at different pH of 7.03, 4.00 and 2.10. (b) The concentration vs the switching input voltage. The switching input voltage is taken as the first point that the output voltage reaches -0.299 V. At PBS reference at 7.03 and sensed PBS at different pH of 7.03, 4.00 and 2.10.

7. Conclusion and Summary

7.1. Summary

The work presented in this thesis is fully 3D printed biosensors based on OECTs that use PEDOT:PSS as the active semiconductor component. These devices are fabricated in two different ways, gas injection 3D printing, using an nScrypt 3Dn-Tabletop 3D Printing and Micro-Dispensing System, and aerosol jet 3D printing, using an Optomec Aerosol Jet® 5x System. The different fabrication methods lead to different device performance due to the different device dimensions, PEDOT:PSS ink conductivity and gate materials. The nScrypt printed OECTs used in this thesis have a peak transconductance of ~2.54 mS. The Optomec printed OECTs used in this thesis have a peak transconductance of ~43.32 mS. These results are outlined in Chapter 3.

Chapter 4 describes two novel sensors using aerosol jet 3D printed OECTs, using a platinum gate. These OECTs were used to sense Δ9-tetrahydrocannabinol (THC), which is the psychoactive component in cannabis. These sensors can detect concentrations of THC, diluted in DI water, down to 0.05 nM. These sensors have a small error of less than 1.41%. The sensitivity has two different regions of -0.04188 /dec from 0.1 to 500 nM and -0.1730 /dec for 500 to 5000 nM. These same OECTs are also used as single-use sensors to detect melatonin concentrations as low as 10 nM and as high as 1 μM. The melatonin sensing results are preliminary but indicate that OECTs can, in fact, be used as melatonin concentration sensors.

In Chapter 5, aerosol jet 3D printed OECTs are arranged into logic gates. This chapter presents NOT, NOR and NAND logic gates. These logic gates are made exclusively using p-type depletion-mode OECTs. These logic gates successfully reproduce their respective logic tables. NOT, NAND and NOR gates are the building blocks for other, more complex logic circuits including multiplexers, de-multiplexers and flip-flops. A simple two-input, single-output multiplexer design was also presented, however, a better printing design needs to be implemented for a working multiplexer.

In addition, each of these logic gates was tested with different concentrations of electrolytes. Ultimately, the required input voltage decreases as the cation concentration increases. The cation concentration detection abilities of these logic gates are explored in-depth, using a NOT gate in Chapter 6.

A gas injection printed NOT gate was used to study the change in the electrical response due to a change in the electrolyte concentration in Chapter 6. This work was previously published in Elsevier's Sensors and Actuators B: Chemical as "Fully 3D printed OECT based logic gate for detection of cation type and concentration"[1] The sensors can distinguish between different concentrations of electrolyte, with a limit of detection of 1 nM. The NOT gates can also distinguish between Na^+, Ca^{2+}, and K^+ as the switching voltages can be directly correlated with the ionic mobility of the respective cations. These NOT gates illustrate sensitivities up to 650 mV/dec for Na^+, which is beyond the Nernst limit and five times more than other reported work. This chapter also includes an appendix with previously unpublished work that shows these NOT gates being used as pH sensors. This is preliminary work that shows acidic pH detection down to a pH of 2.10.

The work presented in this thesis explores the many ways in which OECTs can be used as novel sensors for THC and melatonin sensors. These same OECTs can also be used to build logic gates, which can also be used to detect cation types and cation concentrations as well as pH levels. All of these devices are fully 3D printed which allows for fast prototyping, customization and commercialization. Also, by 3D printing, the fabrication cost can be greatly reduced compared to traditional microfabrication techniques.

7.2. Future Work

7.2.1. THC Sensors

The THC sensors presented in Chapter 4 show a good response for THC diluted in DI water. This is an ideal case, meaning that there are no other entities present to interfere with the test results. However, because PEDOT:PSS is electrochemically active, these sensors would respond to other bio-entities such as cations, which would skew the results. These sensors should ideally be used to sense THC concentrations in saliva, where there are a number of other entities, including various cations. Therefore, the next step in developing these sensors is to add specificity by functionalizing them to exclusively sense THC. This could potentially be done by attaching THC antibodies to either the channel or the gate. This will allow for exclusive and specific sensing of THC as the antibody acts like a lock and key system.

7.2.2. Melatonin Sensors

The melatonin sensors illustrated in Chapter 4 show a response to various concentrations of melatonin. However, these results are preliminary and indicate that these OECTs can detect concentrations of melatonin down to 10 nM. This detection, however, is under ideal conditions as the melatonin is diluted in DI water, meaning that there are no other entities present in the samples as would be the case in bio-fluids. For these sensors to be used for wearable sensing applications to detect melatonin in sweat or saliva, these sensors will have to be functionalized to add specificity and exclusivity.

7.2.3. Logic Gates

The logic gates presented in Chapter 5 have a lot of potential for future work. These logic gates could be miniaturized and arranged into more complex logic circuits such as multiplexers, demultiplexers and flip-flops. These logic circuits can allow for signal processing and sensing in the same platform that is easily 3D printed. In addition, the inputs of these logic circuits, especially multiplexers, can each be functionalized to target a specific bio-entity. This allows for larger biosensing platforms that are capable of sensing multiple bio-entities simultaneously. In addition, these biosensing platforms can be coupled with external components to build more robust biosensing platforms. Components like microcontrollers (MCUs), voltage regulators, communication modules (Wi-Fi and Bluetooth) and batteries. This will mean a device that is completely wearable that can transmit the measured data from a person's body to a phone or computer. This sort of application can be used to expand telehealth solutions and allow doctors and patients to track their health more accurately and acutely.

References

1. Majak, D., Fan, J. & Gupta, M. Fully 3D printed OECT based logic gate for detection of cation type and concentration. *Sensors Actuators B Chem.* **286**, 111–118 (2019).
2. Markets and Markets. Flexible Electronics & Circuit Market by OLED & LCD Display, Printed Sensor - 2023 | MarketsandMarkets. *Marketsandmarkets.Com* https://www.marketsandmarkets.com/Market-Reports/flexible-electronics-market-50634885.html (2018).
3. Turner, A. Biosensors: Then and now. *Trends in Biotechnology* vol. 31 119–120 (2013).
4. Kim, J., Campbell, A. S., de Ávila, B. E. F. & Wang, J. Wearable biosensors for healthcare monitoring. *Nature Biotechnology* vol. 37 389–406 (2019).
5. Darsanaki, R. K., Azizzadeh, A., Nourbakhsh, M., Raeisi, G. & Aliabadi, M. A. Biosensors: Functions and Applications. *J. Biol. today's world* **2**, 53–61 (2013).
6. Patel, S., Nanda, R., Sahoo, S. & Mohapatra, E. Biosensors in health care: The milestones achieved in their development towards lab-on-chip-analysis. *Biochemistry Research International* vol. 2016 (2016).
7. Hasan, A. *et al.* Recent advances in application of biosensors in tissue engineering. *Biomed Res. Int.* **2014**, 307519 (2014).
8. Sabr, A. kh. Biosensors. *Glob. J. Res. Eng.* **16**, (2016).
9. Jain, Y. *et al.* Biosensors, types and applications. *BEATS 2010 Proc. 2010 Int. Conf. Biomed. Eng. Assist. Technol. Jalandhar, India* 1–6 (2010).
10. Gouvea, C. Biosensors for health applications. in *Biosensors for Health, Environment and Biosecurity* (InTech, 2011). doi:10.5772/16983.
11. Watts, H. J., Lowe, C. R. & Pollard-Knight, D. V. Optical Biosensor for Monitoring Microbial Cells. *Anal. Chem.* **66**, 2465–2470 (1994).
12. Syam, R., Justin Davis, K., Pratheesh, M. D., Anoopraj, R. & Surej Joseph, B. Biosensors: A Novel Approach for Pathogen Detection. *VetScan* **1**, 14–18 (2012).
13. Clark, L. C. & Lyons, C. Electrode systems for continuous monitoring cardiovascular surgery. *Ann. N. Y. Acad. Sci.* **102**, 29–45 (1962).
14. Ronkainen, N. J., Halsall, H. B. & Heineman, W. R. Electrochemical biosensors. *Chemical Society Reviews* vol. 39 1747–1763 (2010).
15. Bandodkar, A. J. & Wang, J. Non-invasive wearable electrochemical sensors: A review. *Trends in Biotechnology* vol. 32 363–371 (2014).
16. Mitsubayashi, K., Suzuki, M., Tamiya, E. & Karube, I. Analysis of metabolites in sweat as a measure of physical condition. *Anal. Chim. Acta* **289**, 27–34 (1994).
17. Wang, J. Carbon-Nanotube Based Electrochemical Biosensors: A Review. *Electroanalysis* **17**, 7–14 (2005).
18. Shao, Y. *et al.* Graphene Based Electrochemical Sensors and Biosensors: A Review. *Electroanalysis* **22**, 1027–1036 (2010).
19. Hansen, J. A. *et al.* Quantum-Dot/Aptamer-Based Ultrasensitive Multi-Analyte Electrochemical Biosensor. *J. Am. Chem. Soc.* **128**, 2228–2229 (2006).

20. Huang, J., Liu, Y. & You, T. Carbon nanofiber based electrochemical biosensors: A review. *Anal. Methods* **2**, 202–211 (2010).
21. Yogeswaran, U. & Chen, S.-M. A Review on the Electrochemical Sensors and Biosensors Composed of Nanowires as Sensing Material. *Sensors* **8**, 290–313 (2008).
22. Kergoat, L., Piro, B., Berggren, M., Horowitz, G. & Pham, M. C. Advances in organic transistor-based biosensors: From organic electrochemical transistors to electrolyte-gated organic field-effect transistors. *Analytical and Bioanalytical Chemistry* vol. 402 1813–1826 (2012).
23. Wang, Q. *et al.* Low-voltage, High-performance Organic Field-Effect Transistors Based on 2D Crystalline Molecular Semiconductors. *Sci. Rep.* **7**, 1–8 (2017).
24. Kumar, S. & Dhar, A. Low Operating Voltage N-channel Organic Field Effect Transistors using Photoresist/LiF Bilayer Gate Dielectric. in *Procedia Engineering* vol. 141 78–82 (Elsevier Ltd, 2016).
25. Xu, W. & Rhee, S. W. Low-operating voltage organic field-effect transistors with high-k cross-linked cyanoethylated pullulan polymer gate dielectrics. *J. Mater. Chem.* **19**, 5250–5257 (2009).
26. Padma, N., Sen, S., Sawant, S. N. & Tokas, R. A study on threshold voltage stability of low operating voltage organic thin-film transistors. *J. Phys. D. Appl. Phys.* **46**, 325104 (2013).
27. Casans, S., Muñoz, D. R., Navarro, A. E. & Salazar, A. ISFET drawbacks minimization using a novel electronic compensation. *Sensors Actuators, B Chem.* **99**, 42–49 (2004).
28. Wang, D., Noël, V. & Piro, B. Electrolytic Gated Organic Field-Effect Transistors for Application in Biosensors—A Review. *Electronics* **5**, 9 (2016).
29. Macchia, E. *et al.* About the amplification factors in organic bioelectronic sensors. *Mater. Horizons* (2020) doi:10.1039/C9MH01544B.
30. Tadayon, F. & Sepehri, Z. A new electrochemical sensor based on a nitrogen-doped graphene/CuCo2O4 nanocomposite for simultaneous determination of dopamine, melatonin and tryptophan. *RSC Adv.* **5**, 65560–65568 (2015).
31. Apetrei, I. M. & Apetrei, C. Voltammetric determination of melatonin using a graphene-based sensor in pharmaceutical products. *Int. J. Nanomedicine* **11**, 1859–1866 (2016).
32. Molaakbari, E., Mostafavi, A. & Beitollahi, H. Simultaneous electrochemical determination of dopamine, melatonin, methionine and caffeine. *Sensors Actuators, B Chem.* **208**, 195–203 (2015).
33. Gupta, P. & Goyal, R. N. Graphene and Co-polymer composite based molecularly imprinted sensor for ultratrace determination of melatonin in human biological fluids. *RSC Adv.* **5**, 40444–40454 (2015).
34. Lee, M.-H. *et al.* Molecularly imprinted electrochemical sensing of urinary melatonin in a microfluidic system. *Biomicrofluidics* **8**, 054115 (2014).
35. WEI, S.-L., PAN, W.-J., WANG, H.-W. & YAN, Z.-J. Study of Melatonin Sensor Based on Molecular Imprinting Technique and Electropolymerization Membrane. *CHINESE J. Anal. Chem. (CHINESE VERSION)* **40**, 1219–1224 (2013).
36. Kumar, N., Rosy & Goyal, R. N. Nanopalladium grained polymer nanocomposite based sensor for the sensitive determination of Melatonin. *Electrochim. Acta* **211**, 18–26 (2016).
37. Kumar, N., Rosy, B. S. P. & Goyal, R. Electrochemical Behavior of Melatonin and its Sensing in Pharmaceutical Formulations and in Human Urine. *Curr. Pharm. Anal.* **13**, 85–90 (2016).
38. Hensley, A. L., Colley, A. R. & Ross, A. E. Real-Time Detection of Melatonin Using Fast-

Scan Cyclic Voltammetry. *Anal. Chem.* **90**, 8642–8650 (2018).

39. Bartlett, C.-A. A. *et al.* Disposable screen printed sensor for the electrochemical detection of methamphetamine in undiluted saliva. *Chem. Cent. J.* **10**, 1–11 (2016).
40. Stevenson, H. *et al.* A Rapid Response Electrochemical Biosensor for Detecting Thc In Saliva. *Sci. Rep.* **9**, 12701 (2019).
41. Drummer, O. H. Drug testing in oral fluid. *Clin. Biochem. Rev.* **27**, 147–59 (2006).
42. Niedbala, R. S. *et al.* Detection of Marijuana Use by Oral Fluid and Urine Analysis Following Single-Dose Administration of Smoked and Oral Marijuana. *J. Anal. Toxicol.* **25**, 289–303 (2001).
43. Thompson, L. K. & Cone, E. J. Determination of Δ9-tetrahydrocannabinol in human blood and saliva by high-performance liquid chromatography with amperometric detection. *J. Chromatogr. B Biomed. Sci. Appl.* **421**, 91–97 (1987).
44. Teixeira, H., Proença, P., Corte-Real, F. & Vieira, D. N. Analysis of Δ9-tetrahydrocannabinol in oral fluid samples using solid-phase extraction and high-performance liquid chromatography–electrospray ionization mass spectrometry. *Forensic Sci. Int.* **150**, 205–211 (2005).
45. Quintela, O., Andrenyak, D. M., Hoggan, A. M. & Crouch, D. J. A Validated Method for the Detection of Δ9-Tetrahydrocannabinol and 11-nor-9-Carboxy- Δ9-Tetrahydrocannabinol in Oral Fluid Samples by Liquid Chromatography Coupled with Quadrupole-Time-of-Flight Mass Spectrometry. *J. Anal. Toxicol.* **31**, 157–164 (2007).
46. Kircher, V. & Parlar, H. Determination of Δ9-tetrahydrocannabinol from human saliva by tandem immunoaffinity chromatography-high-performance liquid chromatography. *J. Chromatogr. B Biomed. Sci. Appl.* **677**, 245–255 (1996).
47. Teixeira, H. *et al.* Cannabis and driving: the use of LC–MS to detect Δ9-tetrahydrocannabinol (Δ9-THC) in oral fluid samples. *Forensic Sci. Int.* **146**, S61–S63 (2004).
48. Gross, S. J. *et al.* Detection of Recent Cannabis Use by Saliva Δ9-THC Radioimmunoassay. *J. Anal. Toxicol.* **9**, 1–5 (1985).
49. Luo, D., Chen, F., Xiao, K. & Feng, Y.-Q. Rapid determination of Δ9-Tetrahydrocannabinol in saliva by polymer monolith microextraction combined with gas chromatography–mass spectrometry. *Talanta* **77**, 1701–1706 (2009).
50. Moore, C. *et al.* Detection of Conjugated 11-nor- Δ9-Tetrahydrocannabinol-9-carboxylic Acid in Oral Fluid. *J. Anal. Toxicol.* **31**, 187–194 (2007).
51. Rohrich, J., Zorntlein, S., Becker, J. & Urban, R. Detection of Δ9-Tetrahydrocannabinol and Amphetamine-Type Stimulants in Oral Fluid Using the Rapid Stat Point-of-Collection Drug-Testing Device. *J. Anal. Toxicol.* **34**, 155–161 (2010).
52. Kauert, G. F., Ramaekers, J. G., Schneider, E., Moeller, M. R. & Toennes, S. W. Pharmacokinetic Properties of Δ9-Tetrahydrocannabinol in Serum and Oral Fluid. *J. Anal. Toxicol.* **31**, 288–293 (2007).
53. Huestis, M. A. & Cone, E. J. Relationship of Δ9-Tetrahydrocannabinol Concentrations in Oral Fluid and Plasma after Controlled Administration of Smoked Cannabis. *J. Anal. Toxicol.* **28**, 394–399 (2004).
54. Moore, C. *et al.* Detection of the Marijuana Metabolite 11-Nor- Δ9-Tetrahydrocannabinol-9-Carboxylic Acid in Oral Fluid Specimens and Its Contribution to Positive Results in Screening Assays. *J. Anal. Toxicol.* **30**, 413–418 (2006).
55. Cirimele, V., Villain, M., Mura, P., Bernard, M. & Kintz, P. Oral fluid testing for cannabis:

On-site OraLine® IV s.a.t. device versus GC/MS. *Forensic Sci. Int.* **161**, 180–184 (2006).

56. Kintz, P., Cirimele, V. & Ludes, B. Detection of Cannabis in Oral Fluid (Saliva) and Forehead Wipes (Sweat) from Impaired Drivers. *J. Anal. Toxicol.* **24**, 557–561 (2000).
57. Maseda, C. *et al.* Detection of Δ9-THC in saliva by capillary GCECD after marihuana smoking. *Forensic Sci. Int.* **32**, 259–266 (1986).
58. Tan, C., Gajovic-Eichelmann, N., Stöcklein, W. F. M., Polzius, R. & Bier, F. F. Direct detection of Δ9-tetrahydrocannabinol in saliva using a novel homogeneous competitive immunoassay with fluorescence quenching. *Anal. Chim. Acta* **658**, 187–192 (2010).
59. Tan, C., Gajovic-Eichelmann, N., Polzius, R., Hildebrandt, N. & Bier, F. F. Direct detection of Δ9-tetrahydrocannabinol in aqueous samples using a homogeneous increasing fluorescence immunoassay (HiFi). *Anal. Bioanal. Chem.* **398**, 2133–2140 (2010).
60. Just, W. W., Filipovic, N. & Werner, G. Detection of Δ9-tetrahydrocannabinol in saliva of men by means of thin-layer chromatography and mass spectrometry. *J. Chromatogr. A* **96**, 189–194 (1974).
61. Zhang, M. *et al.* A low power sensor signal processing circuit for implantable biosensor applications. *Smart Mater. Struct.* **16**, 525–530 (2007).
62. Gao, W. *et al.* Fully integrated wearable sensor arrays for multiplexed in situ perspiration analysis. *Nature* **529**, 509–514 (2016).
63. Lee, B. Y. *et al.* Biosensor system-on-a-chip including CMOS-based signal processing circuits and 64 carbon nanotube-based sensors for the detection of a neurotransmitter. *Lab Chip* **10**, 894–898 (2010).
64. Sun, H. *et al.* Complementary Logic Circuits Based on High-Performance n-Type Organic Electrochemical Transistors. *Adv. Mater.* **30**, 1704916 1–7 (2018).
65. Nilsson, D., Robinson, N., Berggren, M. & Forchheimer, R. Electrochemical Logic Circuits. *Adv. Mater.* **17**, 353–358 (2005).
66. Hutter, P. C., Rothlander, T., Scheipl, G. & Stadlober, B. All Screen-Printed Logic Gates Based on Organic Electrochemical Transistors. *IEEE Trans. Electron Devices* **62**, 4231–4236 (2015).
67. Klauk, H., Zschieschang, U., Pflaum, J. & Halik, M. Ultralow-power organic complementary circuits. *Nature* **445**, 745–748 (2007).
68. Ribierre, J. C., Watanabe, S., Matsumoto, M., Muto, T. & Aoyama, T. Majority carrier type conversion in solution-processed organic transistors and flexible complementary logic circuits. *Appl. Phys. Lett.* **96**, 083303 (2010).
69. Hambsch, M., Reuter, K., Kempa, H. & Hübler, A. C. Comparison of fully printed unipolar and complementary organic logic gates. *Org. Electron.* **13**, 1989–1995 (2012).
70. Ribierre, J. C. *et al.* Direct Laser Writing of Complementary Logic Gates and Lateral p-n Diodes in a Solution-Processible Monolithic Organic Semiconductor. *Adv. Mater.* **22**, 1722–1726 (2010).
71. Shiwaku, R. *et al.* A printed organic amplification system for wearable potentiometric electrochemical sensors. *Sci. Rep.* **8**, 3922 (2018).
72. Roy, S., David-Pur, M. & Hanein, Y. Carbon Nanotube-Based Ion Selective Sensors for Wearable Applications. *ACS Appl. Mater. Interfaces* **9**, 35169–35177 (2017).
73. Ghittorelli, M. *et al.* High-sensitivity ion detection at low voltages with current-driven organic electrochemical transistors. *Nat. Commun.* **9**, 1441 (2018).
74. Lin, P., Yan, F. & Chan, H. L. W. W. Ion-sensitive properties of organic electrochemical transistors. *ACS Appl. Mater. Interfaces* **2**, 1637–1641 (2010).

75. Scheiblin, G., Coppard, R., Owens, R. M., Mailley, P. & Malliaras, G. G. Referenceless pH Sensor using Organic Electrochemical Transistors. *Adv. Mater. Technol.* **2**, 1600141 1–5 (2017).
76. Mariani, F., Gualandi, I., Tessarolo, M., Fraboni, B. & Scavetta, E. PEDOT: Dye-Based, Flexible Organic Electrochemical Transistor for Highly Sensitive pH Monitoring. *ACS Appl. Mater. Interfaces* **10**, 22474–22484 (2018).
77. Lakard, B. *et al.* Miniaturized pH biosensors based on electrochemically modified electrodes with biocompatible polymers. *Biosens. Bioelectron.* **19**, 595–606 (2004).
78. ELEY, D. D. & Eley, D. D. (Chemistry Department, B. U. Phthalocyanines as Semiconductors. *Nature* **162**, 819 (1948).
79. Shirakawa, H., Louis, E. J., MacDiarmid, A. G., Chiang, C. K. & Heeger, A. J. Synthesis of electrically conducting organic polymers: halogen derivatives of polyacetylene, (CH) x. *J. Chem. Soc. Chem. Commun.* 558–578 (1977) doi:10.1039/C39770000578.
80. Thiele, J. Zur Kenntniss der ungesättigten Verbindungen. Theorie der ungesättigten und aromatischen Verbindungen. *Justus Liebig's Ann. der Chemie* **306**, 87–142 (1899).
81. Milián-Medina, B. & Gierschner, J. π-Conjugation. *Wiley Interdiscip. Rev. Comput. Mol. Sci.* **2**, 513–524 (2012).
82. Son, S. Y. *et al.* Exploiting π–π Stacking for Stretchable Semiconducting Polymers. *Macromolecules* **51**, 2572–2579 (2018).
83. Holgate, S. A. *Understanding Solid State Physics*. *Understanding Solid State Physics* (Taylor & Francis, 2010).
84. Jakubiak, R., Collison, C. J., Wan, W. C., Rothberg, L. J. & Hsieh, B. R. Aggregation Quenching of Luminescence in Electroluminescent Conjugated Polymers. *J. Phys. Chem. A* **103**, 2394–2398 (1999).
85. Hadziioannou, G. ; M. G. G. *Semiconducting polymers: chemistry, physics and engineering*. (Wiley, 2007).
86. Zan, H. *Polymer Electronics* . (CRC Press, 1960).
87. So, F. *Organic Electronics: Materials, Processing, Devices and Applications*. vol. 8 (CRC Press, 2010).
88. Borges-González, J., Kousseff, Christina J. ; Nielsen, C. B., Kousseff, C. J. & Nielsen, C. B. Organic semiconductors for biological sensing. *J. Mater. Chem. C* **7**, 1111–1130 (2019).
89. Yan, H. *et al.* A high-mobility electron-transporting polymer for printed transistors. *Nature* **457**, 679–686 (2009).
90. Pappa, A. M. *et al.* Direct metabolite detection with an n-type accumulation mode organic electrochemical transistor. *Sci. Adv.* **4**, (2018).
91. Babel, A. & Jenekhe, S. A. High Electron Mobility in Ladder Polymer Field-Effect Transistors. *J. Am. Chem. Soc.* **125**, 13656–13657 (2003).
92. Horowitz, G., Fichou, D., Peng, X. & Garnier, F. Thin-film transistors based on alpha-conjugated oligomers. *Synth. Met.* **41**, 1127–1130 (1991).
93. Tiwari, S. *et al.* Poly-3-hexylthiophene based organic field-effect transistor: Detection of low concentration of ammonia. *Sensors Actuators, B Chem.* **171–172**, 962–968 (2012).
94. Dumitru, L. M., Manoli, K., Magliulo, M., Palazzo, G. & Torsi, L. Low-voltage solid electrolyte-gated OFETs for gas sensing applications. *Microelectronics J.* **45**, 1679–1683 (2014).
95. Inal, S., Malliaras, G. G. & Rivnay, J. Benchmarking organic mixed conductors for transistors. *Nat. Commun.* **8**, (2017).

96. Roberts, M. E. *et al.* Water-stable organic transistors and their application in chemical and biological sensors. *Proc. Natl. Acad. Sci. U. S. A.* **105**, 12134–12139 (2008).
97. Torsi, L. *et al.* A sensitivity-enhanced field-effect chiral sensor. *Nat. Mater.* **7**, 412–417 (2008).
98. Khim, D. *et al.* Precisely Controlled Ultrathin Conjugated Polymer Films for Large Area Transparent Transistors and Highly Sensitive Chemical Sensors. *Adv. Mater.* **28**, 2752–2759 (2016).
99. Pfattner, R. *et al.* On the Working Mechanisms of Solid-State Double-Layer-Dielectric-Based Organic Field-Effect Transistors and Their Implication for Sensors. *Adv. Electron. Mater.* **4**, 1700326 (2018).
100. White, H. S., Kittlesen, G. P. & Wrighton, M. S. Chemical Derivatization of an Array of Three Gold Microelectrodes with Polypyrrole: Fabrication of a Molecule-Based Transistor. *J. Am. Chem. Soc.* **106**, 5375–5377 (1984).
101. Mostafalu, P. *et al.* Smart Bandage for Monitoring and Treatment of Chronic Wounds. *Small* **14**, 1703509 (2018).
102. Kaempgen, M. & Roth, S. Transparent and flexible carbon nanotube/polyaniline pH sensors. *J. Electroanal. Chem.* **586**, 72–76 (2006).
103. Paul, E. W., Ricco, A. J. & Wrighton, M. S. Resistance of polyaniline films as a function of electrochemical potential and the fabrication of polyaniline-based microelectronic devices. *J. Phys. Chem.* **89**, 1441–1447 (1985).
104. Rahimi, R. *et al.* A low-cost flexible pH sensor array for wound assessment. *Sensors Actuators, B Chem.* **229**, 609–617 (2016).
105. Bernards, D. A., Malliaras, G. G., N, D. A. & Malliaras, G. G. Steady-state and transient behavior of organic electrochemical transistors. *Adv. Funct. Mater.* **17**, 3538–3544 (2007).
106. Friedlein, J. T., McLeod, R. R. & Rivnay, J. Device physics of organic electrochemical transistors. *Organic Electronics* vol. 63 398–414 (2018).
107. Timpanaro, S., Kemerink, M., Touwslager, F. J., De Kok, M. M. & Schrader, S. Morphology and conductivity of PEDOT/PSS films studied by scanning–tunneling microscopy. *Chem. Phys. Lett.* **394**, 339–343 (2004).
108. Nardes, A. M. *et al.* Conductivity, work function, and environmental stability of PEDOT:PSS thin films treated with sorbitol. *Org. Electron.* **9**, 727–734 (2008).
109. Gangopadhyay, R., Das, B. & Molla, M. R. How does PEDOT combine with PSS? Insights from structural studies. *RSC Adv.* **4**, 43912–43920 (2014).
110. Brédas, J. L., Wudl, F. & Heeger, A. J. Polarons and bipolarons in doped polythiophene: A theoretical investigation. *Solid State Commun.* **63**, 577–580 (1987).
111. Rumbau, V. *et al.* First Enzymatic Synthesis of Water-Soluble Conducting Poly(3,4-ethylenedioxythiophene). *Biomacromolecules* **8**, 315–317 (2007).
112. Yamashita, M., Sasaki, T., Okuzaki, H. & Otani, C. PH dependence of carrier transport in PEDOT:PSS films investigated by THz and IR-UV spectroscopy. in *International Conference on Infrared, Millimeter, and Terahertz Waves, IRMMW-THz* (2012). doi:10.1109/IRMMW-THz.2012.6380295.
113. Ouyang, J. Solution-Processed PEDOT:PSS Films with Conductivities as Indium Tin Oxide through a Treatment with Mild and Weak Organic Acids. *ACS Appl. Mater. Interfaces* **5**, 13082–13088 (2013).
114. Rivnay, J. *et al.* Structural control of mixed ionic and electronic transport in conducting polymers. *Nat. Commun.* **7**, 1–9 (2016).

115. Rivnay, J., Owens, R. M. & Malliaras, G. G. The Rise of Organic Bioelectronics. *Chem. Mater.* **26**, 679–685 (2014).
116. Lin, P. & Yan, F. Organic thin-film transistors for chemical and biological sensing. *Adv. Mater.* **24**, 34–51 (2012).
117. Mabeck, J. T. & Malliaras, G. G. Chemical and biological sensors based on organic thin-film transistors. *Anal. Bioanal. Chem.* **384**, 343–353 (2006).
118. Zhang, M., Lin, P., Yang, M. & Yan, F. Fabrication of organic electrochemical transistor arrays for biosensing. *Biochim. Biophys. Acta - Gen. Subj.* **1830**, 4402–4406 (2013).
119. Sessolo, M., Rivnay, J., Bandiello, E., Malliaras, G. G. & Bolink, H. J. Ion-selective organic electrochemical transistors. *Adv. Mater.* **26**, 4803–4807 (2014).
120. Tang, H., Yan, F., Lin, P., Xu, J. & Chan, H. L. W. Highly sensitive glucose biosensors based on organic electrochemical transistors using platinum gate electrodes modified with enzyme and nanomaterials. *Adv. Funct. Mater.* **21**, 2264–2272 (2011).
121. Zhu, Z. T. *et al.* A simple poly(3,4-ethylene dioxythiophene)/poly(styrene sulfonic acid) transistor for glucose sensing at neutral pH. *Chem. Commun.* **0**, 1556–1557 (2004).
122. Tang, H., Lin, P., Chan, H. L. W. & Yan, F. Highly sensitive dopamine biosensors based on organic electrochemical transistors. *Biosens. Bioelectron.* **26**, 4559–4563 (2011).
123. Lin, P., Luo, X., Hsing, I. M. & Yan, F. Organic electrochemical transistors integrated in flexible microfluidic systems and used for label-free DNA sensing. *Adv. Mater.* **23**, 4035–4040 (2011).
124. Yan, F. & Tang, H. Editorial: Application of thin-film transistors in label-free DNA biosensors. *Expert Rev. Mol. Diagn.* **10**, 547–549 (2010).
125. Yan, F., Mok, S. M., Yu, J., Chan, H. L. W. & Yang, M. Label-free DNA sensor based on organic thin film transistors. *Biosens. Bioelectron.* **24**, 1241–1245 (2009).
126. Khodagholy, D. *et al.* Organic electrochemical transistor incorporating an ionogel as a solid state electrolyte for lactate sensing. *J. Mater. Chem.* **22**, 4440–4443 (2012).
127. Kenry, Yeo, J. C. & Lim, C. T. Emerging flexible and wearable physical sensing platforms for healthcare and biomedical applications. *Microsystems Nanoeng.* **2**, 16043 (2016).
128. Wang, X., Liu, Z. & Zhang, T. Flexible Sensing Electronics for Wearable/Attachable Health Monitoring. *Small* **13**, 1602790 (2017).
129. Seekaew, Y. *et al.* Low-cost and flexible printed graphene-PEDOT:PSS gas sensor for ammonia detection. *Org. Electron. physics, Mater. Appl.* **15**, 2971–2981 (2014).
130. Morin, P.-O., Bura, T. & Leclerc, M. Realizing the full potential of conjugatedpolymers: innovation in polymer synthesis. *Mater. Horizons* **3**, 11–20 (2016).
131. Rivnay, J. *et al.* High-performance transistors for bioelectronics through tuning of channel thickness. *Sci. Adv.* **1**, 1–5 (2015).
132. Sessolo, M. *et al.* Easy-to-fabricate conducting polymer microelectrode arrays. *Adv. Mater.* **25**, 2135–2139 (2013).
133. Liao, C. & CAIZHI MPhil, L. High performance biological sensors based on organic electrochemical transistors (OECTs). *MPhil Thesis* (2014).
134. Khodagholy, D. *et al.* High transconductance organic electrochemical transistors. *Nat. Commun.* **4**, 1–6 (2013).
135. Rivnay, J. *et al.* Organic electrochemical transistors. *Nat. Rev. Mater.* **3**, 17086 (2018).
136. Andersson, P. *et al.* Fast-switching all-printed organic electrochemical transistors. *Org. Electron.* **5**, 1276–1280 (2013).
137. Hütter, P. C., Fian, A., Gatterer, K. & Stadlober, B. Efficiency of the Switching Process in

Organic Electrochemical Transistors. *ACS Appl. Mater. Interfaces* **8**, 14071–14076 (2016).

138. Nilsson, D. *An Organic Electrochemical Transistor for Printed Sensors and Logic*. *Science And Technology* (2005).
139. Mannerbro, R., Ranlöf, M., Robinson, N. & Forchheimer, R. Inkjet printed electrochemical organic electronics. *Synth. Met.* **158**, 556–560 (2008).
140. Basiricò, L., Cosseddu, P., Fraboni, B. & Bonfiglio, A. Inkjet printing of transparent, flexible, organic transistors. in *Thin Solid Films* vol. 520 1291–1294 (2011).
141. Valdes, L. B. Resistivity Measurements on Germanium for Transistors. *Proc. IRE* **42**, 420–427 (1954).
142. Smits, F. M. Measurement of Sheet Resistivities with the Four-Point Probe. *Bell Syst. Tech. J.* **37**, 711–718 (1958).
143. Bard, A. J. & Faulkner, L. R. *Electrochemical methods : fundamentals and applications*. (Wiley, 2001).
144. Afonso, M., Morgado, J. & Alcácer, L. Inkjet printed organic electrochemical transistors with highly conducting polymer electrolytes. *J. Appl. Phys.* **120**, (2016).
145. Ginsburg, B. C. Strengths and limitations of two cannabis-impaired driving detection methods: a review of the literature. *Am. J. Drug Alcohol Abuse* 1–13 (2019) doi:10.1080/00952990.2019.1655568.
146. Grotenhermen, F. Pharmacokinetics and Pharmacodynamics of Cannabinoids. *Clin. Pharmacokinet.* **42**, 327–360 (2003).
147. Armentano, P. Should per se limits be imposed for cannabis? Equating cannabinoid blood concentrations with actual driver impairment: Practical limitations and concerns. *Humboldt J. Soc. Relat.* **35**, 41–51 (2013).
148. Sharma, P., Murthy, P. & Bharath, M. M. S. Chemistry, Metabolism, and Toxicology of Cannabis: Clinical Implications. *Iran. J. Psychiatry* **7**, 149 (2012).
149. Anizan, S. *et al.* Oral fluid cannabinoid concentrations following controlled smoked cannabis in chronic frequent and occasional smokers. *Anal. Bioanal. Chem.* **405**, 8451–8461 (2013).
150. McMullan, C. J., Schernhammer, E. S., Rimm, E. B., Hu, F. B. & Forman, J. P. Melatonin secretion and the incidence of type 2 diabetes. *JAMA - J. Am. Med. Assoc.* **309**, 1388–1396 (2013).
151. Siu, S. W. F., Lau, K. W., Tam, P. C. & Shiu, S. Y. W. Melatonin and prostate cancer cell proliferation: Interplay with castration, epidermal growth factor, and androgen sensitivity. *Prostate* **52**, 106–122 (2002).
152. Sánchez-Barceló, E. J. *et al.* Melatonin-estrogen interactions in breast cancer. *J. Pineal Res.* **38**, 217–222 (2005).
153. Jönsson, S. K. . *et al.* The effects of solvents on the morphology and sheet resistance in poly(3,4-ethylenedioxythiophene)–polystyrenesulfonic acid (PEDOT–PSS) films. *Synth. Met.* **139**, 1–10 (2003).
154. Ouyang, J. *et al.* On the mechanism of conductivity enhancement in poly(3,4-ethylenedioxythiophene):poly(styrene sulfonate) film through solvent treatment. *Polymer (Guildf).* **45**, 8443–8450 (2004).
155. Mukherjee, A. K., Thakur, A. K., Takashima, W. & Kaneto, K. Minimization of contact resistance between metal and polymer by surface doping. *J. Phys. D. Appl. Phys.* **40**, 1789–1793 (2007).
156. Balbino, M. A. *et al.* A Comparative Study Between Two Different Conventional Working

Electrodes for Detection of Δ ^{9} -Tetrahydrocannabinol Using Square-Wave Voltammetry: a New Sensitive Method for Forensic Analysis. *J. Braz. Chem. Soc.* **25**, 589–596 (2014).

157. Balbino, M. A. *et al.* The Application of Voltammetric Analysis of Δ9-THC for the Reduction of False Positive Results in the Analysis of Suspected Marijuana Plant Matter. *J. Forensic Sci.* **61**, 1067–1073 (2016).
158. Bernards, D. A. *et al.* Enzymatic sensing with organic electrochemical transistors. *J. Mater. Chem.* **18**, 116–120 (2008).
159. Xiao-Ping, W. *et al. Study on the Electrochemical Behavior of Melatonin with an Activated Electrode*. https://onlinelibrary.wiley.com/doi/pdf/10.1002/elan.200290007 (2001).
160. Haynes, W. M. *CRC Handbook of Chemistry and Physics, 93rd Edition*. (Taylor & Francis, 2012).
161. Bard, A. J., Parsons, R., Jordan, J. & International Union of Pure and Applied Chemistry. *Standard potentials in aqueous solution*. (M. Dekker, 1985).
162. Tan, D. *et al.* Chemical and Physical Properties and Potential Mechanisms: Melatonin as a Broad Spectrum Antioxidant and Free Radical Scavenger. *Curr. Top. Med. Chem.* **2**, 181–197 (2005).
163. Odell, M. S., Frei, M. Y., Gerostamoulos, D., Chu, M. & Lubman, D. I. Residual cannabis levels in blood, urine and oral fluid following heavy cannabis use. *Forensic Sci. Int.* **249**, 173–180 (2015).
164. Zhang, S. *et al.* Patterning of Stretchable Organic Electrochemical Transistors. *Chem. Mater.* **29**, 3126–3132 (2017).
165. Zhang, S. *et al.* Water stability and orthogonal patterning of flexible micro-electrochemical transistors on plastic. *J. Mater. Chem. C* **4**, 1382–1385 (2016).
166. Marzouk, S. A. M., Buck, R. P., Dunlap, L. A., Johnson, T. A. & Cascio, W. E. Measurement of extracellular pH, K+, and lactate in ischemic heart. *Anal. Biochem.* **308**, 52–60 (2002).
167. Naumova, E. A. *et al.* Dynamic changes in saliva after acute mental stress. *Sci. Rep.* **4**, 4884 (2014).
168. Sulzer, N. U., Schwellnus, M. P. & Noakes, T. D. Serum electrolytes in ironman triathletes with exercise-associated muscle cramping. *Med. Sci. Sports Exerc.* **37**, 1081–1085 (2005).
169. Tayo, B. O. *et al.* Patterns of sodium and potassium excretion and blood pressure in the African Diaspora. *J. Hum. Hypertens.* **26**, 315–324 (2012).
170. Dubach, J. M., Lim, E., Zhang, N., Francis, K. P. & Clark, H. In vivo sodium concentration continuously monitored with fluorescent sensors. *Integr. Biol.* **3**, 142–148 (2011).
171. Dubach, J. M., Harjes, D. I. & Clark, H. A. Ion-selective nano-optodes incorporating quantum dots. *J. Am. Chem. Soc.* **129**, 8418–8419 (2007).
172. Dubach, J. M., Balaconis, M. K. & Clark, H. A. Fluorescent Nanoparticles for the Measurement of Ion Concentration in Biological Systems. *J. Vis. Exp.* (2011) doi:10.3791/2896.
173. Kwak, Y. H. *et al.* Flexible glucose sensor using CVD-grown graphene-based field effect transistor. *Biosens. Bioelectron.* **37**, 82–87 (2012).
174. Knoll, M. & Thämer, M. An enhancement-mode electrochemical organic field-effect transistor. *Electrochem. commun.* **13**, 597–599 (2011).
175. Atkins, P. W. (Peter W., De Paula, J. & Atkins, P. W. (Peter W. *Atkins' Physical chemistry.* (W. H. Freeman and Company New York, 2002).

Appendix 1: PEDOT:PSS Film Characterization

PEDOT:PSS ink was prepared and printed using the Optomec aerosol jet printer. The parameters were adjusted to achieve different thicknesses. The thickness was then measured using profilometry and then the sheet resistivity was measured using a four-point probe. The results are displayed in Figure 0.1.

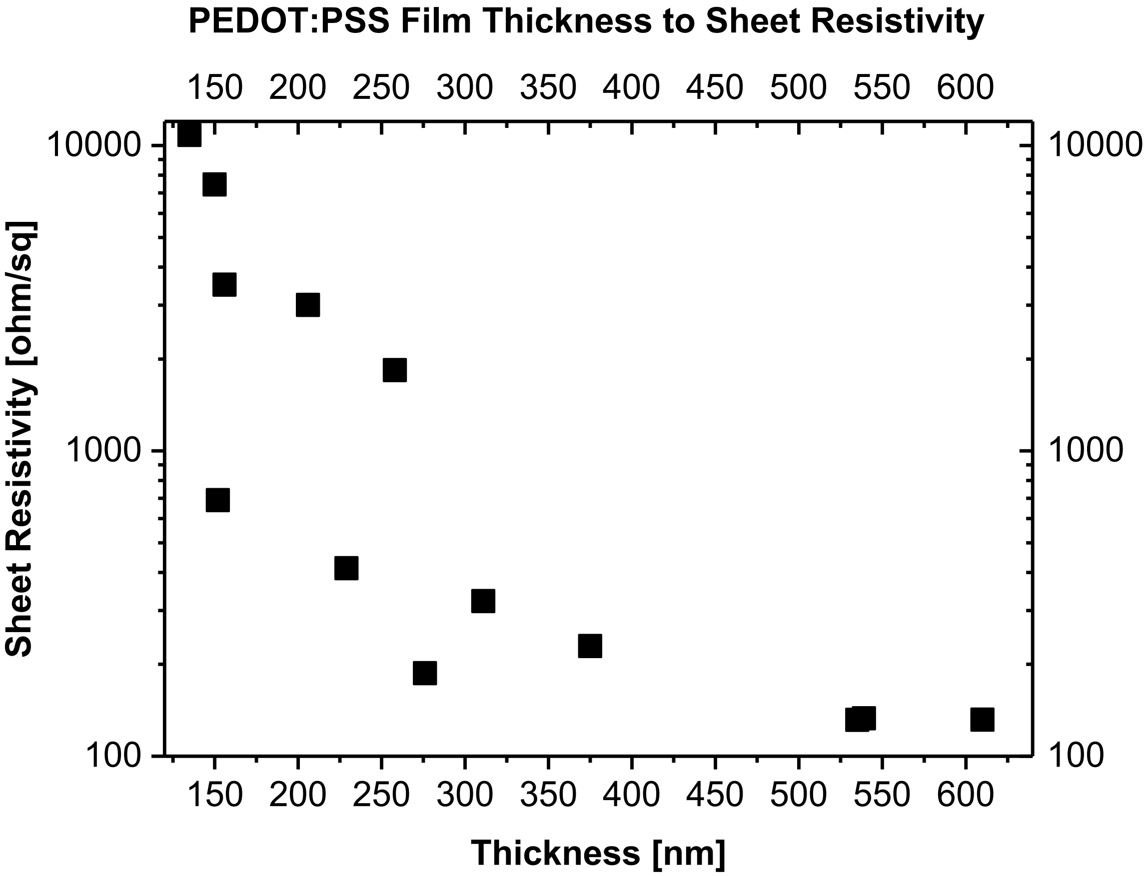

Figure 0.1 Graph showing the sheet resistivity as a function of film thickness.